ROYAUME DU MAROC
Université Mohammed V - RABAT -
جامعة محمد الخامس – الرباط –
Faculté des sciences
كلية العلوم
CENTRE D'ETUDES DOCTORALES - SCIENCES ET TECHNOLOGIES

N° d'ordre 3640

THESE.

En vue de l'obtention du : ***DOCTORAT***

Structure de Recherche *: Équipe de Sciences de la Matière et du Rayonnements*
Discipline : *Physique*
Spécialité : *Physique des Hautes Énergies*

Présentée et soutenue le 25/06/2022 par :

Jihad BOUMAAZA

Search for magnetic monopoles with ANTARES and construction of the KM3NeT telescope.

JURY

Antoine KOUCHNER	*PES, Université Paris cité, Paris, France*	*Président*
Yassine HASSOUNI	*PES, Université Mohammed V, Faculté des sciences - Rabat.*	*Rapporteur/ Examinateur*
Adil BELHAJ	*PH, Université Mohammed V Faculté des sciences - Rabat.*	*Rapporteur/ Examinateur*
Mohammed GOUIGHRI	*PH, Université Ibn Tofail, Faculté des sciences - Kénitra.*	*Rapporteur/ Examinateur*
Nour Eddine FETTOUHI	*PES, Université Mohammed V, Faculté des sciences - Rabat.*	*Examinateur*
Abdelilah MOUSSA	*PH, Université Mohammed Premier, Faculté des sciences - Oujda.*	*Examinateur*
Yahya TAYALATI	*PES, Université Mohammed V, Faculté des sciences - Rabat.*	*Directeur de Thèse*

Année Universitaire : 2021/2022

MOHAMMED V UNIVERSITY in RABAT

Search for magnetic monopoles with ANTARES and construction of the KM3NeT telescope

by

Jihad BOUMAAZA

A thesis submitted in partial fulfillment for the
degree of Doctor of Philosophy

in the
Faculty of Sciences of Rabat
Department or Physics

July 2022

"Forget all the reasons it won't work and believe the one reason that it will."

Acknowledgements

This thesis was carried out within "Equipe de Sciences de Matière et Rayonnement (ESMaR)" at the Faculty of Sciences of the Mohammed V University in Rabat.

I would like to express my gratitude to my supervising professor, **Yahya TAYALATI**, PES at the Faculty of Sciences of University Mohammed V in Rabat, for granting me the opportunity to pursue this work, his trust in me and sharing his wisdom whenever is needed.

I would like to thank Professor **Antoine KOUCHNER**, PES at "le Laboratoire d'AstroParticule et Cosmologie (APC)" of "Université Paris cité, France" as well. Having the spokesperson of the ANTARES collaboration as the president of the jury in my thesis is a great honor.

I thank Professor **Yassine HASSOUNI**, PES at the Faculty of Sciences of University Mohammed V in Rabat, for agreeing to report and examine so closely the content of my doctoral thesis.

I thank as well, Professor **Adil BELHAJ**, PH at the Faculty of Sciences of University Mohammed V in Rabat, for kindly reporting and reviewing my Ph.D.

I also thank Professor **Mohammed GOUIGHRI** PH at the Faculty of Sciences of University Ibn Tofail, Kénitra, for accepting to report and evaluate my thesis, and his insightful comments to improve its quality.

I express my appreciation to Professor **Nour Eddine FETTOUHI**, PES at the Faculty of Sciences of University Mohammed V in Rabat, for accepting to take part in the examining committee, I also thank him for his pertinent discussions and ideas.

I am also grateful to Professor **Abdelilah MOUSSA**, PH at the Faculty of Sciences of University Mohammed I in Oujda, for his thorough examination of my doctoral thesis.

I present my sincere gratitude to all the members of the collaborations ANTARES and KM3NeT, for sharing their knowledge, and never withholding information to help other collaborators progress with their tasks.

I finally take this opportunity to thank all my colleagues and friends of ESMaR, being a part of this group made the hardest of tasks enjoyable.

Abstract

Magnetic monopoles are hypothetical particles that can be detected by their direct Cherenkov emission or that of relativistic secondaries in transparent media. Large scale neutrino observatories designed to detect Cherenkov emission of secondaries produced in high-energy neutrino collisions provide sensitive probes of a cosmic flux of monopoles. This particular signal has been studied by various neutrino observatories like IceCube, ANTARES, Baikal and AMANDA in the past. This work shows a new analysis with ANTARES data collected over ten years (January 2008 to December 2017) that improves previous limits of the collaboration. Compared to previous ANTARES searches, this analysis uses a run-by-run simulation strategy, with a larger exposure as well as a new simulation of magnetic monopoles taking into account the Kasama, Yang and Goldhaber model for their interaction cross-section with matter. No signal compatible with the passage of relativistic magnetic monopoles is observed, and upper limits on the flux of magnetic monopoles with $\beta = \mathrm{v}\ /\mathrm{c} \geq 0.55$, are presented. For ultra relativistic magnetic monopoles the flux limit is $\sim 7 \times 10^{-18}\ cm^{-2}s^{-1}sr^{-1}$. This thesis focuses also on the project of the integration of digital optical modules, a task carried out in the faculty of Sciences in Rabat, and being a major step in the construction of the KM3NeT telescope.

Key Words: Magnetic monopoles, ANTARES, Cherenkov, Neutrino telescope, KM3NeT, Digital Optical Module.

Résumé

Les monopôles magnétiques sont des particules hypothétiques qui peuvent être détectées par leur émission directe Cherenkov ou celle des secondaires relativistes dans les milieux transparents. Les télescopes à neutrinos à grande échelle conçus pour détecter l'émission Cherenkov de secondes produites dans les collisions de neutrinos à haute énergie fournissent des sondes sensibles d'un flux cosmique de monopôles. Ce signal particulier a été étudié par divers télescopes à neutrinos comme IceCube, ANTARES, Baikal et AMANDA dans le passé. Ce travail montre une nouvelle analyse avec des données ANTARES collectées sur dix ans (janvier 2008 à décembre 2017) qui améliore les limites précédentes de la collaboration. Par rapport aux précédentes recherches ANTARES, cette analyse utilise une stratégie de simulation run-by-run, avec une plus grande exposition ainsi qu'une nouvelle simulation des monopôles magnétiques prenant en compte le modèle de Kasama, Yang et Goldhaber pour leur interaction de section avec la matière. Aucun signal compatible avec le passage des monopôles magnétiques relativistes n'est observé, et des limites supérieures sur le flux des monopôles magnétiques avec $\beta = \mathrm{v}/\mathrm{c} \geq 0.55$, sont présentées. Pour les monopôles magnétiques ultra-relativistes, la limite de flux est $\sim 7 \times 10^{-18}\ cm^{-2}s^{-1}sr^{-1}$. Cette thèse porte également sur le projet d'intégration de modules optiques digitaux, tâche réalisée à la faculté des sciences de Rabat, et constituant une étape majeure dans la construction du télescope KM3NeT.

Mots-clefs: Monopoles magnétique, ANTARES, Cherenkov, telescope à neutrino, KM3NeT, Module Optique Digital.

Résumé détaillé

Les monopôles magnétiques font l'objet de recherches considérables parmi toutes les observations cosmologiques actuellement menées. Ces défauts topologiques sont nécessairement produits lors des transitions de phase dans l'Univers primordial, selon de nombreuses théories de la physique des particules. De plus, les défauts topologiques auraient joué un rôle clé dans les situations de l'Univers primitif et auraient pu contribuer à la création d'énormes structures. Les monopôles magnétiques sont des particules hypothétiques avec une charge magnétique qui, contrairement aux aimants ordinaires avec deux pôles magnétiques opposés, peuvent provoquer une gamme d'événements physiques inattendus. Le champ électrique dans l'électromagnétisme de Maxwell est généré par les charges habituelles, lui conférant une divergence non nulle, cependant le champ magnétique est toujours de divergence nulle du fait de l'indisponibilité des charges ponctuelles correspondantes, la seule source du champ magnétique est le courant électrique, qui est un mouvement de charges électriques. Les monopôles magnétiques indiqueraient ainsi la présence de courants magnétiques, qui fourniraient également une source au champ électrique d'un type différent des sources typiques.

Les monopôles magnétiques ont les attributs les plus simples de tous les défauts topologiques, et malgré le fait qu'ils peuvent fournir un signal distinctif dans un détecteur de particules, aucune expérience ne les a jamais trouvés. Seules des limites à leur flux ont été déterminées pour diverses expériences.

Le télescope à neutrinos ANTARES, objet de la première partie de cette thèse, permet la recherche de monopôles magnétiques. À moins qu'un signal significatif audessus de l'espérance de fond atmosphérique ne soit observé, le but de cette enquête est d'utiliser une compilation de dix années de données ANTARES acquises entre 2008 et 2017 pour fixer une meilleure limite supérieure sur le flux de monopôle magnétique. La deuxième partie de cette thèse s'articulera autour de la construction du nouveau télescope KM3NeT, considéré comme la nouvelle génération améliorée de télescopes à neutrinos, et une discussion sur la contribution des instituts marocains dans cette tâche, en particulier l'intégration des modules d'optique numérique réalisée à la faculté. des sciences à Rabat.

Au chapitre 1 de ce rapport, une description de la géométrie et de la composition du télescope ANTARES, ainsi que ses performances, acquisition de données et détection de bruit.

Le chapitre 2 survole Le contexte théorique des monopôles magnétiques et leur impact, en particulier la symétrie des équations de Maxwell et la quantification de la charge électrique. Les limites théoriques et expérimentales de leur écoulement seront ensuite discutées, ainsi que les résultats de plusieurs études expérimentales. Ensuite, dans le chapitre 3, l'interaction des monopôles magnétiques dans la matière sera discutée, ainsi que leur perte d'énergie dans l'eau et leur signal dans un télescope à neutrinos.

Le chapitre 4 s'articule autour de la simulation effectuée, de la stratégie de reconstruction et du traitement des données, ainsi que de l'efficacité de déclenchement du détecteur. Suivi du chapitre 5 où les résultats de cette analyse sont explorés, et de nouvelles limites sur le flux des monopôles magnétiques sont fixées.

Enfin, le chapitre 6 se concentre sur la construction du télescope KM3NeT, en commençant par l'introduction de la collaboration KM3NeT, la description du détecteur et un aperçu détaillé des activités d'intégration DOM menées à Rabat.

Contents

List of Figures

List of Tables

Abbreviations

ANTARES **A**stronomy with a **N**eutrino **T**elescope and **A**byss environmental **RES**earch

KM3NeT **K**ilo**M**eter **3** (cubic) **N**eutrino **T**elescope

ARCA **A**stroparticle **R**esearch with **C**osmics in the **A**byss

ORCA **O**scillation **R**esearch with **C**osmics in the **A**byss

PMT **P**hoto**M**ulti**P**lier **T**ube

OM **O**ptical **M**odule

DOM **D**igital **O**ptical **M**odule

BM **B**ase **M**odule

DU **D**etection **U**nit

CU **C**alibration **U**nit

LCM **L**ocal **C**ontrol **M**odule

ARS **A**nalog **R**ing **S**ampler

QE **Q**uantum **E**fficiency

TVC **T**ime to **V**oltage **C**onverter

FPGA **F**ield **P**rogrammable **G**ate **A**rray

SFP **S**mall **F**orm-factor **P**luggable

CLB **C**entral **L**ogical **B**oard

HV **H**igh **V**oltage

pe **p**hoto**e**lectron

MM **M**agnetic **M**onopole

WIMP **W**eakly **I**nteracting **M**assive **P**article

KYG **K**asama, **Y**ang and **G**oldhaber

MSW **M**ikheyev–**S**mirnov–**W**olfenstein

WIMP **W**eakly **I**nteracting **M**assive **P**article

GUT **G**rand **U**nified **T**heory

HPSS **H**igh **P**erformance **S**torage **S**ystem

MC **M**onte**C**arlo

DAQ **D**ata **A**c**Q**uisition

QA/QC **Q**uality **A**ssurance / **Q**uality **C**ontrol

Dedicated to my parents to whom I give my infinite gratitude, for their unconditional support and encouragement throughout my path.

Introduction

The history of the Univers has been well described by astrophysics and particle physics. Researchers were able to decode the development of matter around us using the Big-Bang cosmological model on the one hand and the standard model of particle physics on the other. These models have had a lot of success with their forecasts, which have been tested. Nevertheless, researchers have never been able to precisely describe the very first moments of the Univers. Physicists are prompted to propose theories for what could have happened at the beginning of the Univers (inflation [1], CP violation [2], topological defects [3], etc.).

Understanding the processes involved in large cosmic accelerators in the context of high energy astrophysics needs more information than simply observing photons from the source, for which several techniques of creation are possible. In the contemporary environment of astroparticle physics, high-energy neutrino telescopes are favored devices. These telescopes can bring very interesting results on neutron oscillations and indirect detection of non-baryonic dark matter, in addition to having entry to the core of stellar objects, due to the weak interaction of neutrinos with matter, permitting the crossing of extremely dense regions without interacting. Beside detecting high-energy neutrinos, neutrino telescopes have a broad detection surface, which will open up new possibilities, particularly in the hunt for exotic particles, while imposing significant flux limits.

Magnetic monopoles are the focus of considerable research among all the cosmological observations now being conducted. These topological defects are necessarily produced during phase transition in the early Univers, according to numerous particle physics theories [4, 5]. Furthermore, topological flaws would have played a key part in the early Univers's situations and might have aided in the creation of huge structures. Magnetic monopoles are hypothetical particles with a magnetic charge that, unlike ordinary magnets with two opposed magnetic poles, can cause a range of unexpected physical events. The electric field in Maxwell's electromagnetism is generated by the usual charges, granting it a none null divergence, however the magnetic field is always of null divergence owing to the unavailability of the relating point charges; the magnetic field's

only source is the electric current, which is a movement of electric charges. Magnetic monopoles would thus indicate the presence of magnetic currents, which would likewise provide a source to the electric field of a different kind than the typical sources.

Magnetic monopoles have the simplest attributes of all topological defects, and despite the fact that they can provide a distinctive signal in a particle detector, no experiment has ever found them. Only limits on their flux have been determined for various experiments [6–9].

The ANTARES neutrino telescope, which is the subject of the first part of this thesis, permits the search for magnetic monopoles. Unless a significant signal above the atmospheric background expectancy is seen, the goal of this investigation is to use a compilation of ten years of ANTARES data acquired between 2008 and 2017 to set a better upper limit on the magnetic monopole flux. The second part of this thesis will revolve around the construction of the new KM3NeT telescope, considered the new upgraded generation of neutrino telescopes, and a discussion about the contribution of Moroccan institutes in this task, especially the Digital Optical modules integration carried out in the faculty of sciences in Rabat.

In Chapter 1 of this report, a description of the geometry and composition of the ANTARES telescope, as well as its performance, data acquisition and noise detection.

Chapter 2 hovers over The theoretical background of magnetic monopoles and their impact, particularly the symmetry of Maxwell equations and the quantization of electric charge. Theoretical and experimental limits on their flow will then be discussed, as well as the results of several experimental studies. After that, in Chapter 3, the interaction of magnetic monopoles in matter will be discussed, along with their energy loss in water, and their signal in a neutrino telescope.

Chapters 4 revolves around the performed simulation, the reconstruction strategy, and data processing, as well as the trigger efficiency of the detector. Followed by chapter 5 where the results of this analysis are explored, and new limits on the magnetic monopoles' flux are set.

Finally, chapter 6 is focused on the construction of the KM3NeT telescope, starting by introducing the KM3NeT collaboration, the description of the detector and a detailed look into the DOM integration activities carried out in Rabat.

Chapter 1

The ANTARES TELESCOPE

1.1 Introduction

ANTARES (for Astronomy with a Neutrino Telescope and Abyss Environmental Research) [10] is an underwater neutrino telescope which operated in the Mediterranean abyss during the period 2008-2022. The result of an international collaboration which brought together around 200 physicists, engineers, oceanologists and astronomers from 8 countries: Germany, Spain, France, Italy, the Netherlands, Morocco, Romania and Australia (see Fig.1.1).

FIGURE 1.1: The ANTARES collaboration cities and sites.

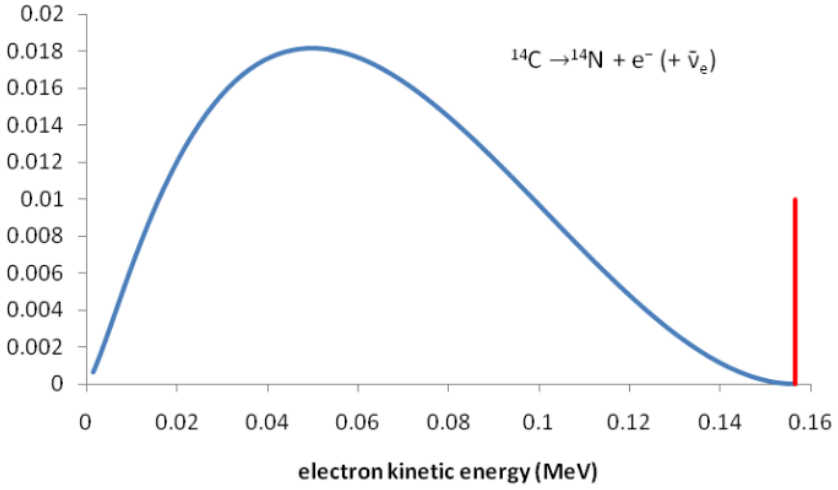

FIGURE 1.2: The electron energy spectrum for carbon-14 beta decay. If only one electron were released, the red line represents the estimated electron energy. The electron energies detected are shown in blue.

The construction of the detector was completed on May 30, 2008, after several construction phases, which will be detailed below with a full description of the telescope.

1.2 Scientific framework of ANTARES

The ANTARES experiment focuses on three topics: particle physics, which is now facing one of the most daunting difficulties that is neutrino oscillation, particle astrophysics, which is primarily attempting to unravel the enigma of dark matter, and astronomy.

1.2.1 Neutrino oscillation

For the first time in nuclear physics, neutrinos have been discovered, notably in beta decay, when a nucleus of atomic number Z converts into a nucleus of atomic number $Z + 1$ with the emission of an electron. The following process converts carbon 14 to nitrogen 14 as an example:

$$C_6^{14} \rightarrow N_7^{14} + e^- \tag{1.1}$$

The progeny nucleus has less mass than the parent nucleus in beta decay. The electron is intended to take out the difference in masses in the form of kinetic energy, according to Einstein's $E = mc^2$. Instead of all electrons having the same energy, as indicated in Fig.1.2, there distribution is continuous:

Wolfgang Pauli hypothesized the presence of a light neutral particle (neutrino) with spin 1/2 released with the electron in beta decay in a famous letter to a conference

in Tübingen. As a result, the available energy is shared between the electron and the undiscovered neutral particle, explaining the continuous spectrum as well as solving a few other technical non-conservation issues.

Fermi proposed the neutrino in his Beta decay hypothesis [11], demonstrating its validity in nuclear and particle physics. The problem with this particle was it could not be detected, causing physicists to be concerned about the new theory's failure. Fortunately, the experimental identification of these evasive particles was established with the progress of nuclear fission in the 1930s and 1940s. Nuclear fission provided a high quantity of neutrinos.

Neutrinos are totally massless according to the basic standard model, however with the development of the so-called Solar Neutrino Problem, scientists recognized that this assumption needed to be reconsidered. Neutrino astronomy experiments revealed that the Sun's flow of electron neutrinos was lower than predicted. Later, neutrino oscillations in vacuum or, more likely, within the Sun itself, aided by the high electron density in the solar core, were proposed as a solution to the problem (the MSW effect [12]).

The transformation of electron neutrinos into another flavour is one of the neutrino oscillation remedies to the solar neutrino conundrum. Recent Super-Kamiokande neutrino detector results [13] appear to support the occurrence of atmospheric muonic neutrino oscillations. The finding of an imbalance between upward and downward going muonic events led to this conclusion. Other studies [14, 15] agree with this conclusion.

The phenomenon of quantum oscillation occurs between particles whose mass eigenstates are different from the eigenstates of flavors. If the oscillations are confirmed, this inevitably implies that the neutrinos have a mass. In the simple case of a mixture of two flavors of ν_α and ν_β neutrinos, the eigenstates of flavors can be decomposed into a linear combination of the mass eigenstates ν_1 and ν_2 (of mass m_1 and m_2 respectively), via a unitary mixture matrix:

$$\begin{pmatrix} \nu_\alpha \\ v_\beta \end{pmatrix} = \begin{pmatrix} \cos\theta & \sin\theta \\ -\sin\theta & \cos\theta \end{pmatrix} \quad \begin{pmatrix} \nu_1 \\ v_2 \end{pmatrix} \tag{1.2}$$

θ being the angle of mixture, the transition amplitude from ν_α to ν_β may be calculated using the time evolution equation of mass states:

$$\langle v_\beta \mid v_\alpha \rangle = -\cos\theta \sin\theta \exp\left(\frac{-iE_1 t}{\bar{h}}\right) + \sin\theta \cos\theta \exp\left(\frac{-iE_2 t}{\bar{h}}\right) \tag{1.3}$$

and to determine the probability of the transition:

$$P\left(v_\alpha \to v_\beta\right) = \sin^2(2\theta)\sin^2\left[1.27\frac{\Delta m^2\left(eV^2\right)L(km)}{E_v(GeV)}\right] \tag{1.4}$$

Where $\Delta m^2 = \left|m_1^2 - m_2^2\right|$ is the difference between the squared masses

The distance L for neutrinos created in the atmosphere ranges from 15 km (downward vertical trajectory) to about 13000 km (upward vertical trajectory). The muon events show asymmetry in Super-Kamiokande data, but not in the associated electronic events. At a 90% confidence level, current results show the disappearance of muon neutrinos, most likely owing to oscillations $V_\mu \leftrightarrow V_\tau$, with $\sin^2 2\theta > 0.88$ and $1.6^{-3} < \Delta m^2 < 4 \times 10^{-3}\mathrm{eV}^2$ the most plausible parameters being a complete mixing $\left(\sin^2 2\theta = 1\right)$ and a squared mass difference $\Delta m^2 \approx 2.5 \times 10^{-3}\mathrm{eV}^2$ [13].

At low energy, the averaged impact of atmospheric neutrino oscillations is visible as a reduction in flux, as shown in Fig.1.3. High-energy neutrino telescopes sensitive to $x = E/\cos\theta > 20\mathrm{GeV}$ can capture both the maximum and minimum of this probability of survival.

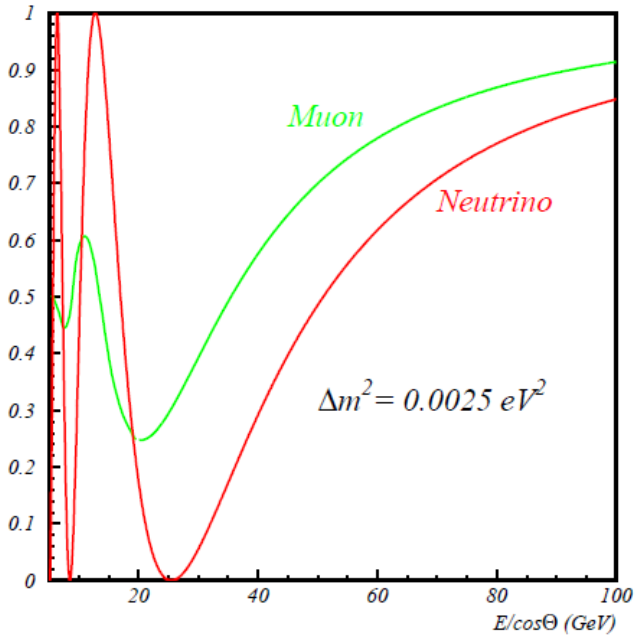

FIGURE 1.3: Ascending neutrino survival probability as a function of $x = E/\cos\theta$, where x represents the actual values of the neutrinos or the accompanying muons they generate.

1.2.2 Astronomy and Astrophysics

The interaction of protons propelled from astrophysical objects with matter or radiation produces high-energy neutrinos. These proton interactions create pions, which decay into neutrinos through leptonic decay modes. As a result, a number of astronomical neutrino sources are implicated.

Compact objects like neutron stars and black holes accrete mass from their normal partner stars, resulting in plasma waves in a strong magnetic field that stochastically accelerate protons to high energies. The accelerated particles' interactions with the accreting matter or the companion star would subsequently create a neutrino flux similar to that of high-energy particles with a spectral index near to 2.

Supernovae, or supermassive star bursts, cause high-energy particles to accelerate. In rare situations, supernovae may leave a neutron star that can be detected as a pulsar. Different mechanisms might be at work in supernovae shells to accelerate protons, which combine with the matter to produce charged and neutral pion decays, which produce neutrinos and photons, respectively. The detection of these neutrinos would reveal a clear indicator of proton acceleration, as well as the source's direction.

1.2.3 Cosmology and dark matter

Astrophysicists have recently come to the conclusion that the majority of the matter in the cosmos is non-luminous "dark matter." The observed flattening of disk galaxies' rotation curves, which suggest a dynamical mass substantially greater than that considered by the ingredient stars and gas, is the finest proof for this. The measured amounts of light objects suggest that a large portion of the dark matter in the Universe is non-baryonic. Although no existing particle has the requisite qualities, the stable neutral particle predicted by most variants of supersymmetry theory is a sound theoretical contender.

Through gravitational capture, supersymmetric WIMPs gather in the cores of the Sun and Earth, as well as in the galaxy's center. Because of the high space density, annihilation processes occur, resulting in high-energy neutrinos from the decays of the gauge bosons and heavy particles generated. The ANTARES telescope might detect these neutrinos throughout a relevant range of WIMP masses. Both cosmology and particle theory would benefit greatly from the discovery and identification of a remnant cosmic population of supersymmetric particles.

1.3 Neutrino detection principal in ANTARES

The principle of neutrino telescopes is to detect Cherenkov radiation from leptons, which are products of neutrino interactions by charged current, using a three-dimensional system of PMTs implemented within a large volume of a translucent medium, such as body of water or ice. The Earth serves as a destination for neutrinos as well as a barrier against all other particles (Fig.1.4)

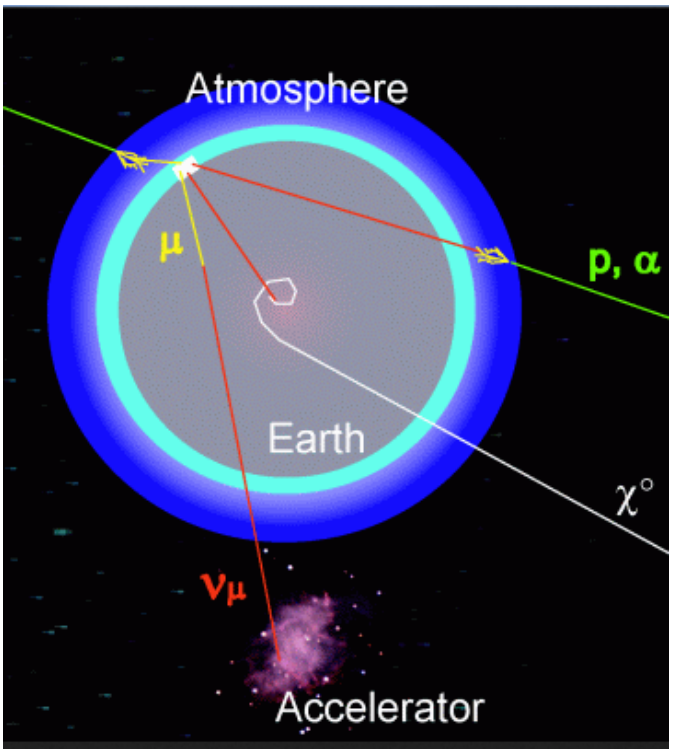

FIGURE 1.4: Detection of upward-going muons as a sign of muon neutrino interactions in the matter below the detector used by a neutrino telescope.

Because neutrinos have a very weak interaction with matter, a broader target compact volume is required. This method of detection necessitates distinguishing upward muons from the higher flux of downward atmospheric muons (see Fig.1.5).

It is required to understand the kinetics of neutrino interactions, the permeability of the Earth, muon energy loss, and detector resolution over a wide range of angles and energies in order to connect the recorded muon spectrum with the original neutrino spectrum.

1.3.1 Neutrino interactions in ANTARES

A neutrino with a mass of $10^{12}eV$ has a random orientation of around $3 \times 10^{11} g.cm^{-2}$, while the radius of the Earth is $2.5 \times 10^{9} g.cm^{-2}$. Supposing a neutrino or anti-neutrino

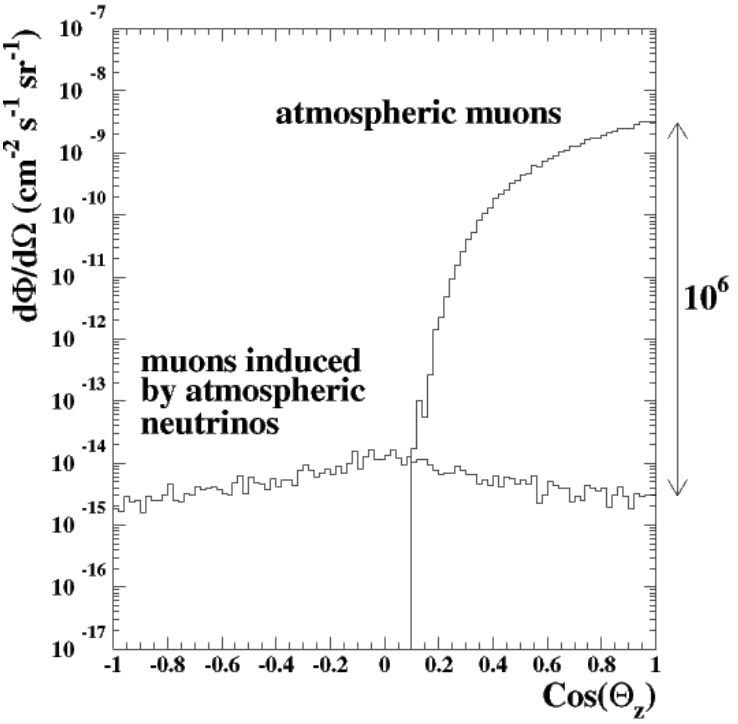

FIGURE 1.5: The flux of muons and neutrinos in the atmosphere as a function of their zenithal angle's cosinus.

released by an origin, it will spread to our Planet with minimal collisions, weakly interacting with it through charged current: $v_l\,(\bar{v}_l) + N \rightarrow l(\bar{l}) + X$, or neutral current: $v_l\,(\bar{v}_l) + N \rightarrow v_l\,(\bar{v}_l) + X$, l being a charged lepton, ν a neutrino, N a nucleon and X is a hadronic sheaf.

Since the radiation distance and nuclear interaction length of water are both less than 1 m, charged-current ν_e interactions produce electromagnetic and hadronic showers with horizontal distances of $\sim$ few meters, which are virtually point-like events on the ANTARES scale. Due to leaving all of their energy above 100 GeV inside the detector volume, the events energy resolution is projected to be greater than that of muon events. However, due to the point-like nature of the showers, the angular resolution is limited when compared to muon events. Neutral-current interactions of both ν_e and ν_μ(and ν_τ if present), would taint the charged-current ν_e interactions. The amount of neutral-current interactions is approximately Third that of charged-current interactions. In neutral-current interactions, the neutrino type is unknown, the energy resolution is limited given the absence of a final-state neutrino, and the angular resolution is low due to the point-like feature.

$\mu^{\pm}$ Leptons are generated by charged-current ν_μ interactions, the energy of which may be deduced using the obtained $\mu^{\pm}$ energy. The mean μ^- is half the energy of ν_μ in the interactions $\nu_\mu d \rightarrow \mu^- u$; while in $\bar{\nu}_\mu u \rightarrow \mu^+ d$ interactions, the mean μ^+ energy is three

quarters of the mean ν_μ energy. For the energy of $\mu^{\pm}$, it may be determined by using $E < 100GeV$ range, or dE/dx if $E > 1TeV$. The hadronic shower provides more details on the energy of ν_μ for interactions inside the volume of the telescope. The ANTARES detector was developed to capture the interactions of these charged current ν_μ.

$\mu^{\pm}$ Leptons having electronic, muonic, and hadronic decay processes are produced through charged-current ν_τ interaction. Charged-current or neutral-current interactions will characterize the electronic and hadronic modes. The muonic decays $\tau^- \rightarrow \mu^- \bar{\nu}_\mu \nu_\tau$, are detectable in ANTARES, but they are difficult to identify from ν_μ interactions.

Muon neutrino interactions are the most suitable to be detected by ANTARES among the other neutrino flavors. Due to the limited energy of electron and the brief lifespan of tau, the detection of their associated neutrinos in terms of efficiency and angular resolution is problematic. As a result, in what follows, only the muon path will be examined.

1.3.2 The Cherenkov effect and ANTARES

Mallet conducted the first observational investigation of this phenomena from 1926 to 1929. Cherenkov, on the other hand, exclusively researched this radiation between 1934 and 1944 [16]. He looked at the angular distribution, the radiation's influence on n and β, and demonstrated that the wave's amplitude is dependent on the distance traversed. The relationship he discovered is given as follows:

$$\cos\theta = \frac{1}{n \cdot \beta} \tag{1.5}$$

θ denoting the angle between the particle path and the produced light orientation.

Particles are mostly ultra-relativistic with $\beta \approx 1$ in the energy range of interest for ANTARES. For a wavelength of $450nm$, the index of refraction of sea water is $n = 1.35$, hence Cherenkov light is released under $42°$ for this wavelength. This simple geometrical arrangement of light emission enables for exact track reconstruction with only a few hits at distinct space positions.

In the case of a uniform medium with the index n, the particle's Cherenkov light release is proportional with regard to its propagation direction. As seen in Fig.1.6, a light cone, also known as a Cherenkov cone, is generated with an angle of θc constant with regard to the particle's propagation.

The neutrino detection with an underwater neutrino telescope is depicted in Fig.1.7.

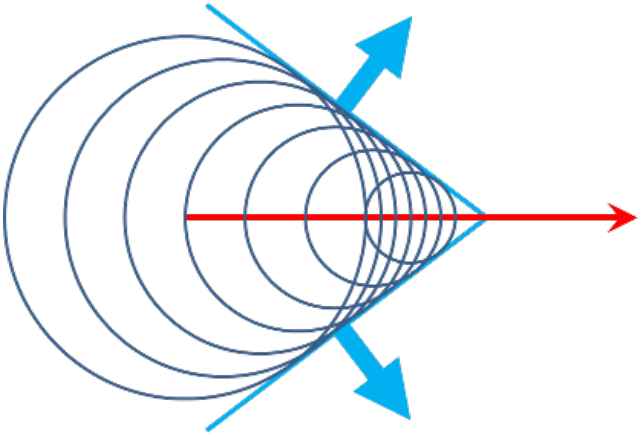

FIGURE 1.6: Illustration of the light emission through the Cherenkov effect, light is emitted in form of a cone.

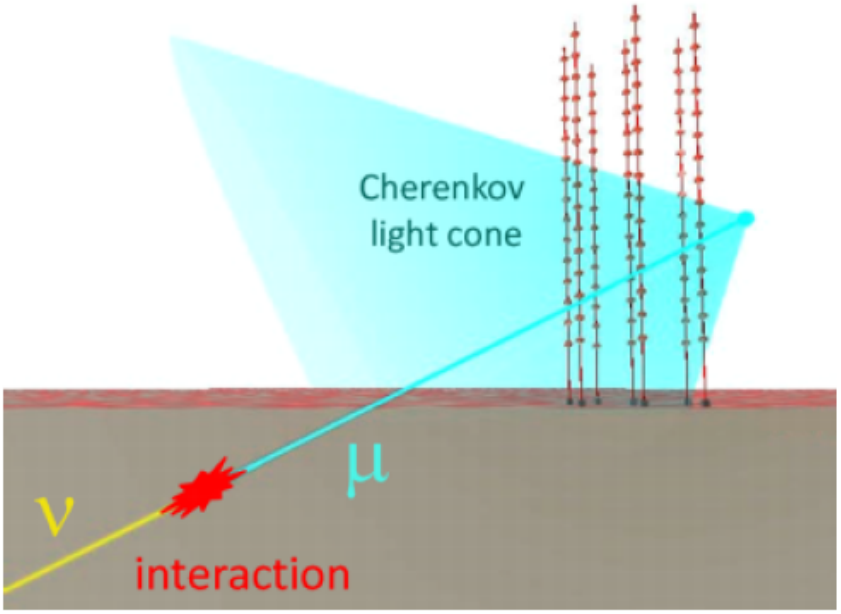

FIGURE 1.7: Depiction of a Cherenkov based neutrino telescope's principal of particle detection. The incoming particle interacts under the detector producing secondary particles that propagate in water while emitting a Cherenkov light cone.

For a particle bearing a unit charge, the number of photons generated across a path dx in a wave length interval $d\lambda$ is:

$$\frac{d^2N}{d\lambda dx} = 2\pi\alpha \sin^2\theta/\lambda^2. \tag{1.6}$$

Relying on the refractive qualities of the substance through which Cherenkov photons are released during a muon crossing, they will disperse differentially. Between 1997 and 2000, many measurement campaigns were conducted on the ANTARES site in order to describe the optical characteristics of the water, particularly the light attenuation length. The effective attenuation length L_{att} is the distance at which the light amplitude has been reduced by a factor of 1/e. It is determined by the absorption length L_{abs} and the scattering distance L_{scatt}, written as follows:

$$\frac{1}{L_{att}} = \frac{1}{L_{abs}} + \frac{1}{L_{scatt}}. \tag{1.7}$$

The attenuation distance is used in the formulation of the luminous intensity I function of distance R at the emission source, of intensity I_0, and is expressed for an isotropic source as follows:

$$I(R) \propto \frac{I_0}{R^2} \exp^{-\frac{R}{L_{att}}}. \tag{1.8}$$

The observations obtained on ANTARES indicate an attenuation distance of the order of 50 m for a wavelength of 473 nm, corresponding the blue color, by evaluating the number of photons as a function of distance to the source.

1.4 ANTARES detector

An artist's view of the ANTARES telescope is presented in figure 1.8. The ANTARES detector was deployed about 40 km off Toulon, France, in a militarized zone chosen for the quality of its relatively flat terrain and for its depth of about 2500 m, which made it possible to overcome both light from the sun as a large part of the atmospheric muons. In addition, its proximity to the coast facilitated deployment and maintenance operations.

1.4.1 Layout of ANTARES

ANTARES telescope is made up of an array of 885 photomultipliers distributed over 12 independent detection lines, spaced from each other by 60 or 75 m, in an area of about

FIGURE 1.8: Artist view of the ANTARES neutrino telescope.

0.1 km^2. These Hamamatsu (R7081-20) 10" photomultipliers (PM) are sensitive in the wavelength region of [300, 600] nm are surrounded by a glass sphere of 17" diameter,2 cm thick to which they are glued using a transparent gel, of which the refractive index of 1.404 is between that of the sphere of 1.47 and water of about 1.35, in order to reduce the reflection of light on its surface.

The PMs are also protected by a mu-metal grid to limit the effects of the earth's magnetic field, and are connected to the electronics necessary to supply them with the high voltage.

Each detection line has 25 floors and is kept vertical by an anchor at the bottom and a buoy at the top. The foot of the line is attached to the anchor by a remotely operated hook. It also supports line power and control module and is equipped with a transducer for acoustic positioning. This latter send signals to the five receivers distributed over the lines. The 12 lines are connected to a junction box, which is connected by a 42 km long electro-optical cable to the control room located in La Seyne sur Mer.

1.4.2 Optical module

The optical modules [17] are the eyes of the telescopes, they have been designed to withstand, like all the other telescope components, the difficult conditions of commissioning in the abyss (see Fig.1.9). Each optical module contains the necessary electronics for the high voltage power supply of the PM as well as a calibration system using an LED.

FIGURE 1.9: The optical module of the ANTARES neutrino telescope.

1.5 DATA acquisition system

The role of the data acquisition system is to transform the signals output from the PMs into data that will be used for reconstruction and physical analysis software. The signals from each optical module are read by two ARS (Analogue Ring Sampler) [18, 19], electronic cards which are used to digitize the arrival time and the charge of the pulse (hit). Hit arrival time is referenced from local control module (LCM). LCM cards are synchronized from the control station by a master clock (see Fig.1.10). the DAQ card of each LCM sends the data to the ground in the form of a list of consecutive hits (frame) with a duration of 104ms of data acquisition. A computer farm located at the ground station, combines the simultaneous packets from each PM into a time window of 104 ms. Thus, each of these packets can contain several muons events, the latter having a detector transit time of the order of 2 μs. However, no selection is made by the on-board acquisition system, and the data sent is mainly due to the surrounding background.

To save as much relevant data as possible from muon and reduce background noise as much as possible. The computer farm applies in real time various triggering systems, The algorithms look for hits related in time and position (coincidences), which will generally be the consequence of a muon passing through the detector, due to the properties of Cherenkov light emission, these do not apply to random background noises.

The events considered in this analysis must fulfill the conditions applied by the ANTARES "T3" triggers [20], which are based on local coincidences defined as the occurrence of

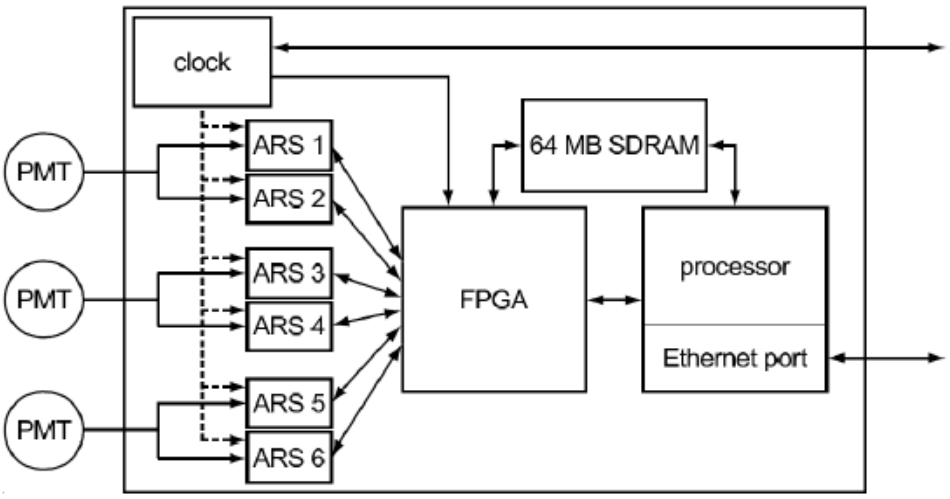

FIGURE 1.10: Schematic view of an LCM.

either two hits on two separate optical modules of a single storey within 20 ns, or one single hit of large amplitude (more than 3 photo-electrons). For this analysis a software trigger is defined as a combination of two local coincidences in adjacent or next to adjacent storeys within 100 ns or 200 ns, respectively.

1.5.1 Optical background noise

The optical background noise in the ANTARES site has been studied very intensively, first by dedicated studies during the R&D phase and then with data taken by the lines. It has two origins: The radioactive disintegration of potassium 40 contained in seawater salt and the bioluminescence.

indeed, seawater contains approximately 400 ppm of potassium, including the radioactive isotope K40 with a proportion of $\sim$ 0.0117%. This isotope decays mainly into Ca40 (89.3%, emitting an electron, whose maximum energy is 1.311 MeV, greater than the energy required to cross the Cherenkov threshold of 1.13 MeV for an electron [21–23].

$$^{40}_{19}K \rightarrow ^{39}_{20}Ca + e^{-} + \bar{\nu}_e \tag{1.9}$$

This background noise is continuous and identical on all optical modules. It has been estimated that it contributes 30 $\pm$ 7 kHz. to the baseline.

Bioluminescence due to bacteria, shrimp or even fish emitting light contributes parity to the baseline and is responsible for peaks. This contribution is very variable over a few hours of data collection. Studies have shown that the peak rate is correlated with sea currents and water temperature (Fig.1.11).

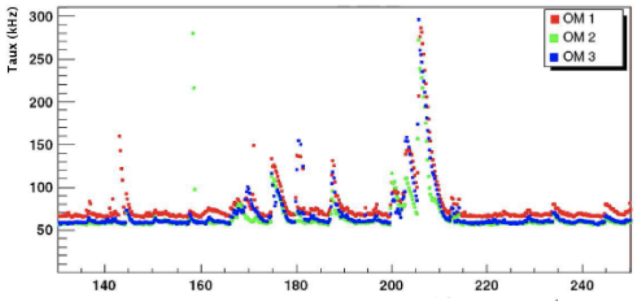

FIGURE 1.11: The count rate of 3 optical modules corresponding to the same floor over a period of a hundred seconds.

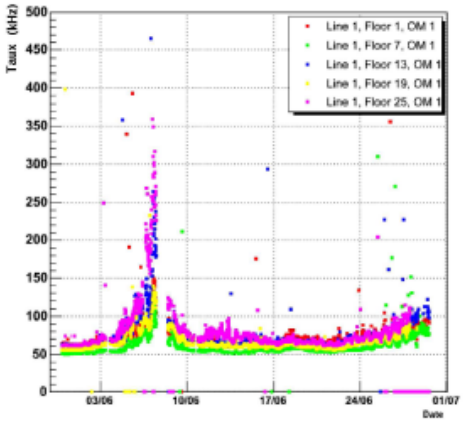

FIGURE 1.12: The count rate corresponding to 5 optical modules of the first line placed on 5 floors for a period of around a month.

1.5.2 Atmospheric background noise

The optical background from the K40 decay, and from bioluminescent organisms dominate the digitized signals from optical modules, For each optical module, a continuous background rate of about 60 kHz is recorded and only 10 Hz of this comes from atmospheric muons.

These muons are produced in the interaction of cosmic rays (mostly very high energy protons) with Earth's upper atmosphere. These protons interact with nuclei in the atmosphere and create secondary particles giving rise to what are called atmospheric shower (Fig.1.12). Many particles produced by the primary rays are not stable enough to reach the ground and decay into other more stable particles, such as muons. Others interact very strongly with atmospheric gas and still produce less energetic showers. At ground level cosmic rays are mainly made up of photons, electrons and positrons, and muons.

Muons are produced from the decay of pions in the cosmic showers :

$$\pi^- \rightarrow \mu^- + \bar{\nu}_\mu \quad et \quad \pi^+ \rightarrow \mu^+ + \nu_\mu \tag{1.10}$$

muons decay by weak interaction into electron or positron with their neutrinos:

$$\mu^- \rightarrow e^- + \bar{\nu}_e + \nu_\mu \quad et \quad \mu^+ \rightarrow e^+ + \nu_e + \bar{\nu}_\mu \tag{1.11}$$

Muons are the only particles produced in the atmosphere, with neutrinos, to be able to reach the ANTARES detector, and emit a characteristic signal. Their flux decrease exponentially with the depth of water crossed, as a consequence of significant energy losses due to e^+e^- pairs productions, Bremsstrahlung and photo-nuclear interactions (figure 3.2). Atmospheric neutrinos resulting from the interaction of cosmic rays with the atmosphere are is also a background that need to be suppressed when searching for magnetic monopoles. We distinguish between:

1- The conventional atmospheric neutrinos, resulting from the decay of kaons and pions, which dominate up to $10^5 - 10^6$ GeV. and 2- The prompt atmospheric neutrinos, produced by the decay of heavier mesons typically containing a charm quark. Their production is strongly suppressed, but they are expected to exhibit a harder energy spectrum. Hence, they could dominate the atmospheric neutrino flux at energies above $\sim$ 100 TeV.

1.6 Conclusion

Undersea neutrino telescopes are viable and controllable from onshore infrastructure, as proved by ANTARES. A neutrino telescope might detect the passage of currently undiscovered particles, such as magnetic monopoles, by being sensitive to any particle releasing light in its path.

The following chapters will cover the prediction of such particles in physics as well as their theoretical basis.

Chapter 2

Magnetic Monopole phenomenology

2.1 Introduction

Physicists have been on the hunt for a particular particle more than any other, this elusive particle is the magnetic monopole. Although it is known by its more popular term "electric charge", the notion of an electric monopole is well-known in physics since it occurs in the form of particles with positive or negative charges, such as electrons and protons. Through the interplay of electric fields, which are defined as going from positive to negative, opposite electric charges attract and similar charges repel. Magnetism appears to be similar to electricity in that it has a magnetic field that runs from north to south. When looking for the magnetic equivalent of the electron, being the magnetic monopole (MM), this comparison falls apart, furthermore, no experimental evidence of MMs has ever been established. MMs are so expected to exist from a theoretical standpoint, discovering one will be a huge step forward in high-energy physics. They get their qualities from physics principles at very high energies, which are considerably beyond the capabilities of any particle accelerator experiment. MMs are completely stable, they do not decay into other particles, and they interact quite strongly with the electromagnetic field, allowing for the possibility to investigate their existence experimentally.

2.2 Classical electrodynamics and magnetic monopoles

Both electric and magnetic fields, **E** and **B** are considered fundamental in classical electrodynamics. Two charges are able to interact since one responds to the field formed

by the other and vice versa. Finding the electric and magnetic fields for given sources and boundary conditions may be simplified to all electromagnetic issues. Even more fundamentally, a set of Maxwell equations may be used to deduce all electromagnetic phenomena. For a vacuum without sources, the following Maxwell equations have an intriguing symmetry:

$$\nabla \cdot \mathbf{E} = 0, \tag{2.1}$$

$$\nabla \cdot \mathbf{B} = 0, \tag{2.2}$$

$$\nabla \times \mathbf{E} + \frac{1}{c}\frac{\partial \mathbf{B}}{\partial t} = 0, \tag{2.3}$$

$$\nabla \times \mathbf{B} - \frac{1}{c}\frac{\partial \mathbf{E}}{\partial t} = 0, \tag{2.4}$$

The equations above show an interchangeability between $\mathbf{E}$ a $\mathbf{B}$, more specifically, they are invariant under:

$$\mathbf{E} \to \mathbf{B} \quad \text{and} \quad \mathbf{B} \to -\mathbf{E} \tag{2.5}$$

However, the aforementioned symmetry appears to be compromised empirically, as no magnetic charges have yet been detected. Assuming there is an electric charge density ρ_e and an electric current J_e but no magnetic counterparts to understand the statement. As a result, the Maxwell equations are written as:

$$\nabla \cdot \mathbf{E} = 4\pi\rho_e, \tag{2.6}$$

$$\nabla \cdot \mathbf{B} = 0, \tag{2.7}$$

$$\nabla \times \mathbf{E} + \frac{1}{c}\frac{\partial \mathbf{B}}{\partial t} = 0, \tag{2.8}$$

$$\nabla \times \mathbf{B} - \frac{1}{c}\frac{\partial \mathbf{E}}{\partial t} = \frac{4\pi}{c}J_e. \tag{2.9}$$

Under the duality transformation, the equations are no more symmetric. The second term of the equations 2.7 and 2.8 appears to be missing something. To understand what they are lacking, we must first define $\nabla \cdot \mathbf{B}$, also known as the divergence of $\mathbf{B}$. Let V be a volume contained in space by a surface S. The integral $\nabla \cdot \mathbf{B}$ over the volume V results in 4π times the total amount of magnetic charge g contained in the volume V. Likewise, $\nabla \cdot \mathbf{B}$ provides 4π times the magnetic charge density at x when evaluated at x. As a result, Equation 2.7 states that no magnetic charge exists at any point in space. Moving charges are roughly similar to currents in terms of magnitude.

However, because the preceding Maxwell equations assume no magnetic charge, there is no magnetic current J_m on the second term of Equation 2.8. As a result, the dualism is no more due to the lack of magnetic charge. In other words, the symmetry is broken when there is no magnetic charge. This begs the issue of why nature is so asymmetrical. There is no reason why magnetic charges couldn't exist in classical electrodynamics, and if they did, the duality symmetry would be preserved. To put it another way, classical electrodynamics is completely consistent with the concept of MMs, and it's odd that MMs don't appear to exist, because their presence would make the theory more symmetric [24].

2.3 Dirac's Magnetic Monopole

In 1931, Paul Dirac originally proposed the notion of a particle with a magnetic charge (the magnetic monopole) [25] in order to justify the quantization of the elementary electric charge, e. When electric charges are measured, they are always integer multiples of the electron charge. This quantization of electric charge is a mysterious natural phenomenon that has no explanation. If we suppose that a particle with a single magnetic pole exists and that it may interact with charged particles, Dirac demonstrated that the principles of quantum mechanics demand that electrical charges should be quantized.

Assume the magnetic field generated by a magnetic monopole with charge g, which is analogous to the Coulomb electric field generated by an electric charge:

$$\vec{B} = \frac{g\vec{r}}{r^3}, \tag{2.10}$$

The classical equations of motion are fulfilled by a particle with an electric charge e interacting with a MM:

$$m\ddot{\vec{r}} = \overrightarrow{e\dot{r}} \wedge \vec{B}. \tag{2.11}$$

This equation defines a classical dynamic that is well understood. However, we must incorporate the potential vector $\vec{A}$, such as $\vec{B} = \vec{\nabla} \wedge \vec{A}$, to define the quantum mechanics of a charged particle while it interacts with a magnetic monopole. The action S_{int} is introduced to describe the interaction component of a charged particle with an extrinsic electromagnetic field

$$S_{int} = \frac{e}{\hbar c}\int_1^2 dt \frac{d\vec{r}}{dt} \cdot \vec{A} = \frac{e}{\hbar c}\int_1^2 d\vec{r} \cdot \vec{A}, \tag{2.12}$$

This is solely determined by the particle's trajectory. The particle's wave function may then be represented as:

$$\psi(\vec{r}) = \psi_0(\vec{r}) e^{i\frac{e}{\hbar c}\int_0^{\vec{r}} d\overrightarrow{r'}\cdot\vec{A}}, \tag{2.13}$$

where $\psi_0(\vec{r})$ is a wave function that complies with the Schrödinger equation. On a sphere around a MM, the potential vector $\vec{A}$ cannot be specified continuously. This definition, however, is irrelevant; only the relative phase among two different trajectories will be of interest.

Assume Γ and Γ' two trajectories having the same starting and ending points:

$$(S_{int})_\Gamma - (S_{int})_{\Gamma'} = \frac{e}{\hbar c}\oint_{\Gamma-\Gamma'} d\vec{r}\cdot\vec{A} = \frac{e}{\hbar c}\int_{S_{\Gamma-\Gamma'}} d^2\vec{S}\cdot\vec{B} = \frac{e}{\hbar c}\Phi_{\Gamma-\Gamma'}. \tag{2.14}$$

The relative phase $\Phi_{\Gamma-\Gamma'}$ has been represented as the magnetic flow across a surface confined by the closed path $\Gamma - \Gamma'$ using the Stokes theorem. As a result, the relative phase is a function of the magnetic field, which is more precisely defined. However, because the phase is multivalued, there is always a challenge. If the path Γ' can scan once the closed surface surrounding the MM and return to its initial position, the action becomes:

$$\Delta S_{int} = \frac{e}{\hbar c}\Phi_{\text{sphere}} = \frac{e}{\hbar c}\frac{g}{r^2}\sin\theta d\theta\int_0^{2\pi} d\phi = \frac{4\pi eg}{\hbar c}, \tag{2.15}$$

θ and ϕ being respectively the zenithal and azimuthal angles in spherical coordinates. At the end, if $\exp(i\Delta S_{int}) = 1$, the relative phase between two paths is clearly established:

$$\frac{eg}{c} = \frac{n\hbar}{2} \quad \longrightarrow \quad g = k\cdot g_D = k\cdot\frac{e}{2\alpha}. \tag{2.16}$$

n being an integer, Dirac's quantization condition is this relationship. If there is a single MM somewhere in the Universe, it would justify why electrical charges are quantized.

2.4 Grand Unification Theories and magnetic monopoles

Unlike Dirac's argument of MM consistency with quantum mechanics, G. 't Hooft [4] and A. M. Polyakov [5] individually proved the requirement of magnetic monopoles in unified gauge theories in 1974. MMs must exist in any unified gauge theory in which the group $U(1)$ defining electromagnetism is embedded in a spontaneously broken semisimple gauge group, and electric charge is therefore automatically quantized. In electromagnetism [26], MMs occur during the phase transition corresponding to the spontaneous breakdown of the unified group into subgroups, one of which is $U(1)$.

Grand unified theories (GUTs) are founded on the notion that at sufficiently high energies, strong, weak, and electromagnetic interactions all arise from the same gauge group, which was divided into $SU(3) \times SU(2) \times SU(1)$. This group reflects the standard model of particle physics: the strong interaction is described by the group $SU(3)$, while the electroweak interaction is described by the group $SU(2) \times SU(1)$. As a result, MMs are a general prediction of grand unification.

2.5 Early Universe and magnetic monopoles

Gauge symmetries were united at the formation of the Universe, when the temperature was extremely high. These gauge symmetries have been spontaneously broken in the context of the phase transitions of the cosmos as the universe expands and its temperature decreases, and at a particular temperature of order Λ. Topological defects, such as MMs, have been produced at this point using the Kibble mechanism [27].

At this stage, one magnetic monopole is formed per causal domain, with a mass of 10^{17} GeV on average. There is an inconsistency with the MM relic known as the "magnetic monopole problem". Their mass density is several orders of magnitude more than the mass density of the visible Universe [28], implying that the density of MMs should be larger than measured. This difficulty may be overcome by supposing that the early universe went through an inflation phase, which attenuates the magnetic monopole density to a minute number [1], (see Fig.2.1).

Inflation models can result in the elimination of this problem, however they drastically decrease the number of MMs in the observable Univers [29].

An alternative option is to use great unification models, in which MMs occur at temperatures lower than 10^11 GeV, much below the original high unification scale [30]. In comparison to cosmology, this results in intermediate MM masses and a more realistic density. MM' mass and charge are greatly reliant on the scale of unification of the gauge theories that predict them.

$$M \geq \frac{\Lambda}{\alpha_G}, \tag{2.17}$$

α_G being the gauge coupling constant unified. The calculation of the low-energy coupling constants predicts that Λ and α_G are on the order of 10^{15} GeV and 10^{-2} GeV, respectively [31].

The MMs created in a minimum SU(5) unification model have a mass of $\sim 10^{17}$ GeV and carry a single Dirac charge [32, 33]. However, a phenomenologically intriguing extension of the SU(5) model predicts a magnetic monopole mass of $\sim 10^{11}$ GeV [34], while

the phenomenologically interesting model SU(15) predicts comparatively light particles of $\sim 10^8$ GeV [35, 36]. Magnetic monopole masses as low as $\sim 10^7$ GeV can exist in some supersymmetric models [37, 38]. Kaluza-Klein models [39, 40] may also be recognized, which lower the mass of vast unification if the extra-dimensions are not excessively compactive. With the addition of two millimeter-sized additional dimensions, the unification scale rises to the order of ~ 100 TeV, indicating a mass of $\sim 10^4$ TeV for MMs. MMs with masses ranging from $\sim 10^4$ GeV to $\sim 10^{20}$ GeV and various charges have a variety of theoretical possibilities. If the production of MMs is not followed by a period of inflation, the Kibble mechanism predicts a significant flux of MMs on Earth.

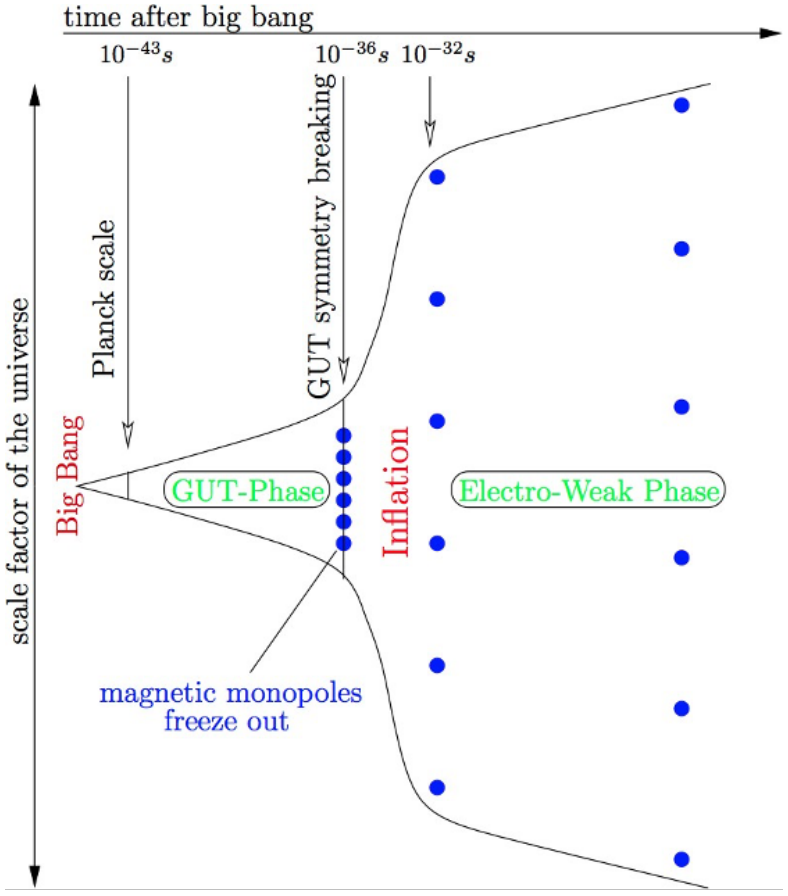

FIGURE 2.1: Depiction of the early Universe's time progression. If monopoles are formed before the symmetry is broken, inflation dilutes their density. Taken from [41]

2.6 Cosmic acceleration of magnetic monopoles

The convenience with which kinetic energy is conveyed to MMs by cosmic magnetic fields is a wide motivator for the search for MMs in high-energy cosmic rays. The MM's kinetic energy T is increased by a magnetic field B interacting along a length l:

$$T = gBl \tag{2.18}$$

It is feasible to compute the energy gB that a MM of minimum charge would acquire over various locations of magnetic fields in the Universe using a fine structure constant of 1/137. This energy may be calculated using the features listed in the table 2.1 (derived from [42]), as well as other expected characteristics of cosmic magnetic fields that MMs can traverse.

Cosmic environment	B(μG)	L(pc)	T(GeV)
Milky Way	3	300	6×10^{10}
Galaxy clusters	2 - 30	10^2 - 10^6	10^{10} - 10^{15}
Extragalactic sheets	0.1 - 1	10^6 - 3×10^7	10^{12} - 10^{15}
AGN jets	10^2	10^2 - 10^4	10^{11} - 10^{13}
Radio galaxy lobes	10 - 10^2	10^5	10^{13} - 10^{14}

TABLE 2.1: The magnetic field intensity B and coherence length L of various cosmic magnetic fields taken from [29, 43, 44]. The last column shows the usual kinetic energy T of a magnetic monopole traversing such a field.

The dominating spectrum of the medium that MMs may transverse is predicted to be the extra-galactic medium. After passing through a coherent extragalactic magnetic field area, a minimum energy gain of 1.7×10^{13} GeV is predicted for a minimum MM charge and $\alpha \sim 1/137$, based on the values in the table 2.1. As a result, $M \leq 1.5 \times 10^{13}$ GeV is required for a magnetic charge to attain a speed of $\beta \geq 0.5$ and hence generate a sufficiently distinctive signal in water. Nevertheless, this computation only considers the passage of a MM through a single coherent field region. According to the publication [42], the number of crossed fields is on the order of $n \approx H_0^{-1}/50Mpc \approx 100$, resulting in a higher order of magnitude acquired energy and hence a limit mass for relativistic MMs on the scale of $M \leq 10^{14}$ GeV.

The existence of detectable galactic magnetic fields can potentially offer an upper limit on the MMs flux, according to Parker [45]. MMs traveling across space will be propelled by the magnetic field, gaining kinetic energy at the expense of the magnetic field. The pace at which the magnetic field energy is drained must be limited in comparison to the time scale of its regeneration in order for the magnetic field to endure. The Parker bound corresponds to the equation below with feasible selections for the astrophysical parameters [46].

$$\Phi_M \lesssim \begin{cases} 10^{-15} & \left[\text{ cm}^{-2}\text{ s}^{-1}\text{sr}^{-1}\right], \quad M \lesssim 10^{17}\text{GeV/c}^2 \\ 10^{-15}\left(\frac{11^{17}\text{GeV}}{M}\right) & \left[\text{cm}^{-2}\text{ s}^{-1}\text{sr}^{-1}\right], \quad M \gtrsim 10^{17}\text{GeV/c}^2 \end{cases} \tag{2.19}$$

The figure 2.2 depicts the Parker bound as well. The restriction is less strict for greater MM masses and velocities.

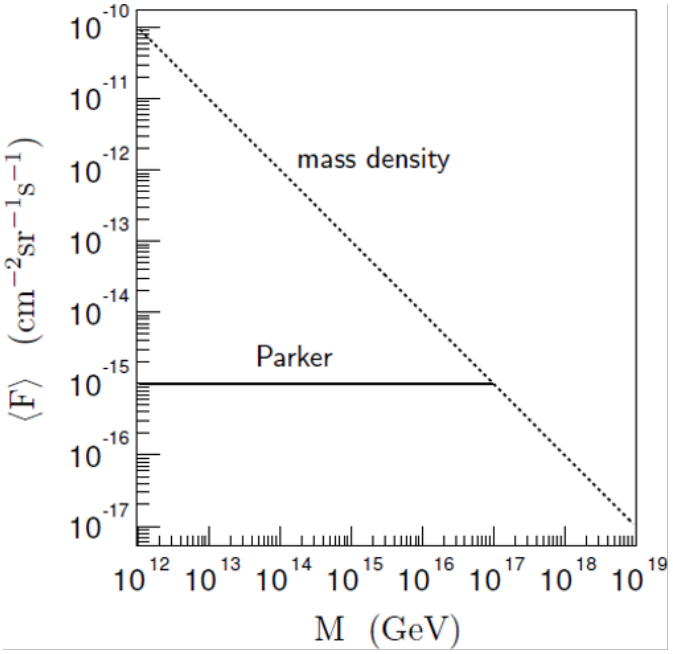

FIGURE 2.2: The upper limits on the flux for a standard magnetic monopole as a function of a typical mass and velocity of $10^{-3}c$. The limits are based on the Universe's mass density (dashed line) and the galactic magnetic field's survival (i.e. the Parker bound, solid line).

2.7 Experimental results

The predicted interactions of MMs as they travel through matter affect search approaches. This would result in a variety of unusual signatures. [47] has a detailed discussion of the methodology used to find these particles, as well as a comprehensive summary of the results in [46].

Since the theoretical prediction of cosmic monopoles' existence, a variety of methods have been used to search for them. The MACRO experiment used various types of excitation and ionization detectors (liquid scintillators, streamer chambers, and nuclear track-etch material) to search for MMs in a large velocity range, $\beta \geq 4 \times 10^{-5}$, with a detection area of several hundred meters squared [48], and obtained the most extended limit on the MM flux, carrying a Dirac charge, according to their velocity. Other experiments results on the MM upper limit on the flux are discussed in chapter 5, and depicted in Fig.5.8 which contains the newest results of the ANTARES telescope as well.

2.8 Conclusion

Magnetic monopoles have yet to be discovered, despite much investigation, and are not included in the standard model theory. Several grand unification theories, on the

other hand, predict the presence of monopoles, or at least the probability of their existence at high energies. Their discovery would have significant implications since it would complete the theory of electromagnetism by making Maxwell's equations perfectly symmetrical under the electrical-magnetic duality, and it would also provide a natural explanation for the quantization of the electric charge.

Chapter 3

Detection of Magnetic Monopoles with ANTARES

3.1 Introduction

A MM with Dirac charge would interact like a heavy ion $Z_e = 68.5e$ at high velocities (assuming a fine structure constant of 1/137). When crossing the medium, significant electromagnetic energy losses are predicted due to the comparatively high charge. The MM generates an electric field vertical to its propagation direction, which interacts with the particles of the medium traveled throughout its passage. As a result of this electric field, the surrounding atoms are ionized and excited. ANTARES is most sensitive to particles moving upward, as a result, it's required to estimate how much energy a MM deposits after traversing the Earth in order to determine if they may be detected as up-going events.

3.2 Magnetic monopole interaction and energy loss

Some processes through which a MM deposits energy (ionization and atomic excitation) in the surrounding medium will be explored in the following sections.

3.2.1 Energy loss due to collision

Based on the Mott cross sections of Bauer and Cole [49, 50], S. P. Ahlen [51] has developed for MMs another version of the Bethe-Bloch formula, describing the energy

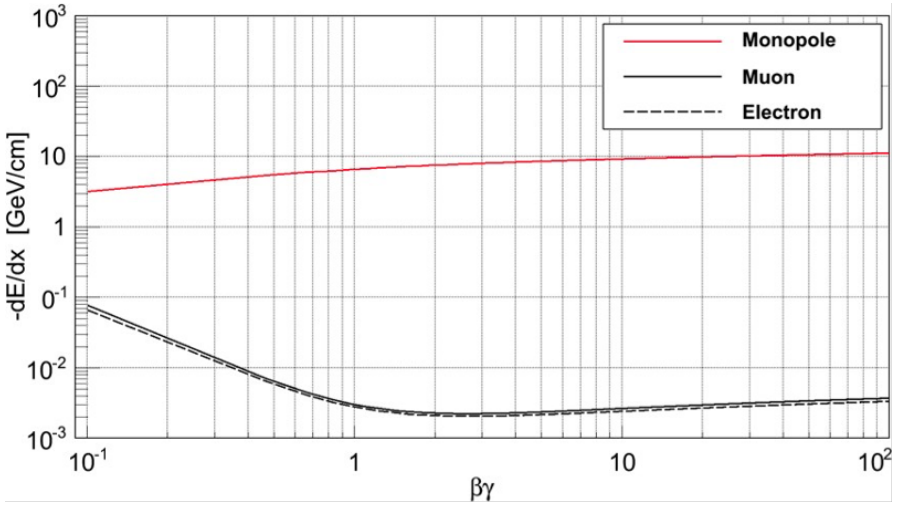

FIGURE 3.1: The mean energy loss rate due to collision per unit path length for MMs with minimum charge (red line). The energy losses for muons and electrons are also displayed (in black). MMs lack the typical rise in energy loss toward lower velocities seen in electric particles [56].

loss in the passing of a heavy electric charge via ionization and excitation in a non-conductive medium. Then later on, he determined the energy loss described in [52] after the publishing of the updated KYG cross section [53]:

$$\frac{dE}{dx} = \frac{4\pi N_e g^2 e^2}{m_e c^2}\left[\ln\left(\frac{2m_e c^2\beta^2\gamma^2}{I}\right) - \frac{1}{2} + \frac{k}{2} - \frac{\delta}{2} - B_m\right]. \tag{3.1}$$

where N_e is the electron density, m_e is the electron mass, g is the MM's charge, I is the mean ionization potential, δ is the density effect correction [54], k is the QED cross-section correction [53], and B_m is the Bloch correction [55]. The formula illustrated in Fig.3.1 is valid in the velocity range of $\beta \leq 0.1$ and $\gamma \geq 100$. The energy loss of MMs increases with velocity, while the energy loss of leptons decreases until $\beta\gamma \sim 3.5$, then increases again. A MM with a magnetic charge g and a velocity βc loses around $(g\beta/Z_e)^2$ times more ionization energy than a particle with electric charge Z_e with the same velocity.

3.2.2 Energy loss due to radiative processes

Radiative processes must be considered at velocities $\gamma > 10^3$ ($\beta \sim 0.999$). Pair creation, Bremsstrahlung, and photo-nuclear interactions are the three processes taken into account for this kind of energy loss. Fig.3.2, borrowed from [42], depicts the electromagnetic energy loss by a MM of mass $M \sim 10^5 GeV$ in air. Collisions cause the majority of the losses until $\gamma \sim 10^4$. Electromagnetic energy losses are driven by pair formation e^+e^- for $10^4 < \gamma < 10^6$ and photonuclear interactions for $\gamma > 10^6$ at higher velocities.

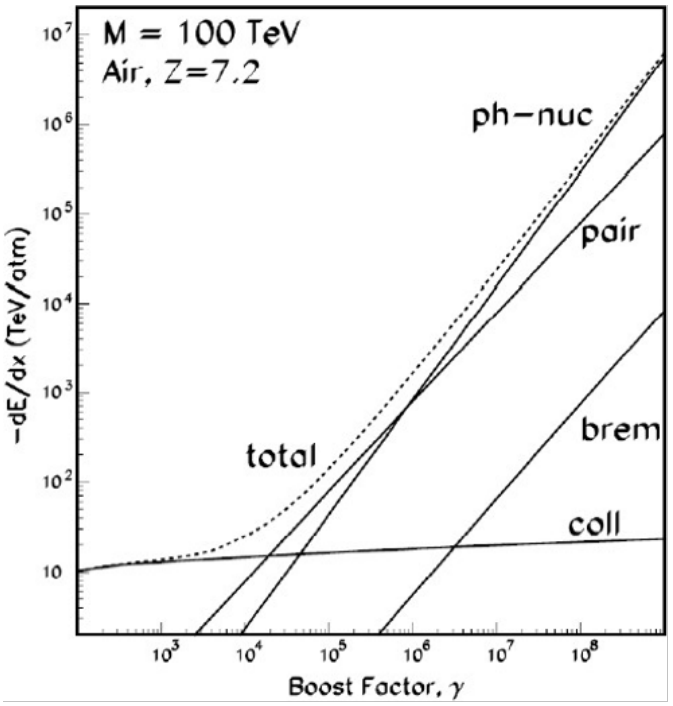

FIGURE 3.2: Electromagnetic energy loss by collision, Bremsstrahlung, pair production, and by photonuclear interactions in air for a monopole of mass $M = 100TeV$, as a function of the boost factor γ.

The energy loss of muons caused by pair production [57, 58] is adapted for MMs in [42], and photonuclear interactions are modeled by the exchange of a virtual photon between the MM and the nucleus, such as the energy losses of leptons produced by these interactions [59]. The contribution of energy losses from MM through Bremsstrahlung radiation, that becomes marginal for massive particles being inversely proportional to their mass [42], is shown in Fig.3.2 while energy losses from collisions, pair production, and photonuclear interactions are mostly independent of the MM mass.

Additionally, using the simplified density profile described by Derkaoui et al. [60], the stopping-power of a MM traversing the Earth may be determined as described in Fig.3.3. Eq.3.1 is used to generate the solid lines of areas A and B. Part C is the outcome of numerical computations found in [60]. The dashed lines reveal that the formulae have been extrapolated past their valid area ($\beta < 10^{-5}$ and $\beta \sim 8 \cdot 10^{-4}$) or that two valid regions have been united with a polynomial to ensure the functions and derivatives continuity ($0.01 < \beta < 0.1$). Despite the energy loss in their passage, MMs with $M \gtrsim 10^{10}$ GeV/c^2 would remain relativistic and observable as up-going events (see, for example, Fig.3 of [47]). Given appropriate astrophysical assumptions, MMs with a mass of $M \lesssim 10^{14}$ GeV/c^2 can be observed in neutrino telescopes as an up-going event with a speed surpassing the Cherenkov threshold.

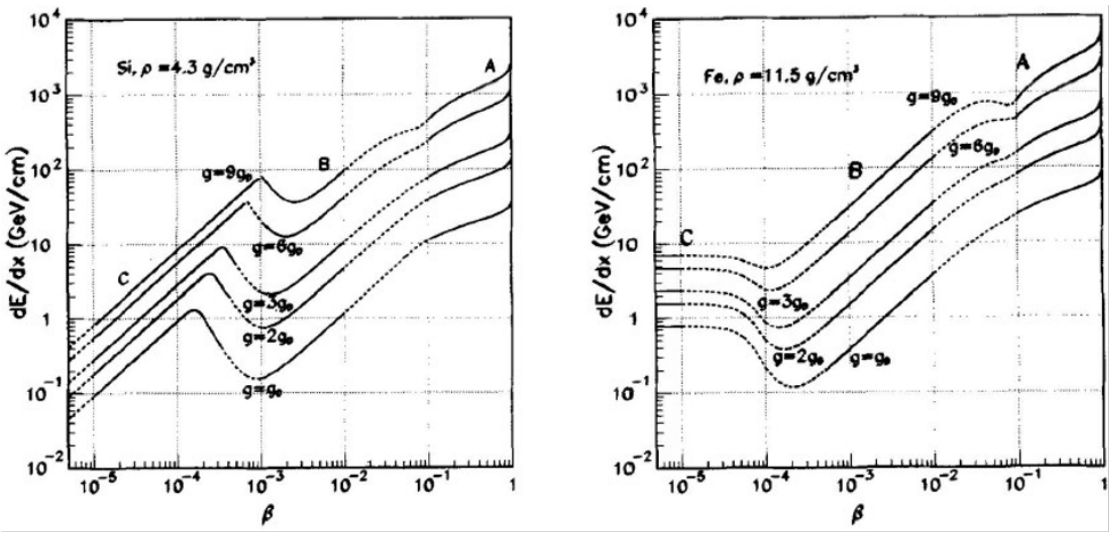

FIGURE 3.3: Ionization energy loss of a monopole in the Earth's mantle (left) and core (right), retrieved from [60].

3.2.3 Callan-Rubakov's Mechanism

Some GUT models predict that MMs would catalyze nuclear decay [61–64]. This necessitates a low MM velocity of roughly $\beta \leq 10^{-3}$. The cross section of catalysis is composed of the following:

$$\sigma_{cat} = \frac{\sigma_0}{\beta}, \tag{3.2}$$

where σ_0 corresponds to the value of strong interaction cross sections ($\sim 10^{-28} cm^2$). During a catalysis, the released energy is divided among several proton decay products, each of which emits Cherenkov radiation. The Cherenkov photon rate may exceed that of the background if the rate of nuclear decay is relatively high along the MM pathway. The aim of this thesis will cover the search for MMs through the direct and indirect Cherenkov emission.

3.3 Signature of magnetic monopole in water

A sufficiently intense MM (with a high mass and a significant Lorentz factor) may traverse the Earth and reach the detector with a considerable upward speed, despite notable energy losses along the passage. The velocity of MMs is the determining factor in the detection technique. Given the tremendous energy that MMs may obtain through acceleration in a cosmological magnetic field and the projected masses based on various models, it appears that a comparatively light MM ($M \leq 10^{12} GeV$) can easily approach relativistic velocities.

3.3.1 Direct Cherenkov emission ($\beta > 0.74$)

Tompkins [65] demonstrated that the Cherenkov emission does not occur for magnetic charges with a velocity of $\beta < 1/n$, where n is the refractive index of the medium. For the case where $\beta > 1/n$, the number of photons emitted per unit of length and wavelength is represented as:

$$\frac{d^2 n_\gamma}{d\lambda dx} = \frac{2\pi\alpha}{\lambda^2}\left(\frac{ng}{e}\right)^2\left(1 - \frac{1}{n^2\beta^2}\right), \tag{3.3}$$

where n_γ denotes the number of photons emitted and λ denotes their wavelength, the other terms are described in the previous chapter. The Cherenkov radiation released by a MM is a factor $(ng/Z_e)^2$ more important than that emitted by an electrically charged particle for a given velocity. A MM's Cherenkov radiation is polarized differently than that of an electric charge, in addition to having a different intensity. With a refractive index of $n \approx 1.35$ for seawater and a fine structure constant of $\alpha \approx 1/137$, a Dirac charge MM $g = g_D$ should release around 8550 times more Cherenkov photons than an electric charge moving at the same speed.

3.3.2 Indirect Cherenkov emission: δ-rays ($\beta \geq 0.52$)

A MM will ionize the surrounding environment as it crosses matter. This ionization will generate δ-electrons (or δ-rays), that have the potential to create Cherenkov radiation provided their kinetic energy is sufficiently high. The $Z \to g\beta/e$ substitution [66] can be used to approximate the electromagnetic interactions of a MM in matter to those generated by an electric charge. Therefore, given the distribution of δ-rays produced by an electric charge, the distribution of δ-rays produced by a MM may be derived [67]. Fig.3.4 depicts the contributions of all processes to the light yield. The differential cross-section of Kasama, Yang, and Goldhaber (KYG) [53] or the more conservative, in terms of photon yield, mott cross section [51] are used to characterize the generation of δ-electrons.

In comparison to the direct and indirect Cherenkov light displayed in Fig.3.4, contributions from water radio-luminescence, pair generation, Bremsstrahlung, and photo-nuclear processes generated by relativistic MMs are minimal and thus are not taken into consideration in this analysis.

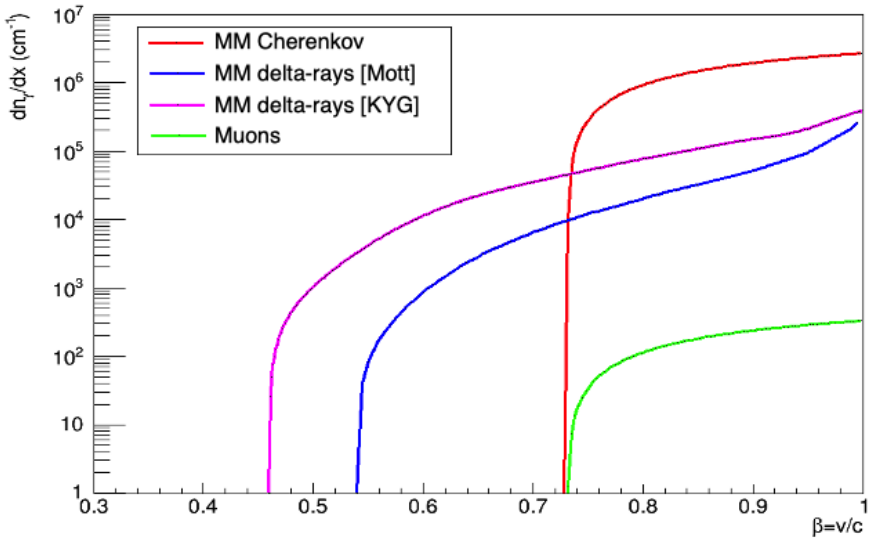

FIGURE 3.4: Number of Cherenkov photons emitted per cm in the sea water from a magnetic monopole (red line), and from δ–rays produced along its path according to the Mott model [51] (blue line), and to the KYG model [53] (magenta line) as a function of the velocity of the monopole. The direct Cherenkov emission from a single muon is also shown as a comparison reference (green line) [68].

δ-ray generation

The distribution of δ-rays generated by a MM per unit of length dx and energy dT_e is determined in [69]:

$$\frac{d^2N_e}{dT_e dx} = \frac{2\pi N g^2 e^2}{m_e c^2} \frac{F\left(T_e\right)}{T_e^2}, \tag{3.4}$$

where T_e is the electrons' kinetic energy In order to produce Cherenkov light in a medium with an index of 1.35, an electron needs at least a $T_0 = 0.25\ MeV$ energy. Eq.3.4 may be utilized to calculate the number of δ-electrons generating Cherenkov radiation since $I = 74\ eV$ for water [70]. The spin of the MM affects the factor $F(T_e)$, nevertheless the generation of δ–ray is independent of its spin as long as T_e is minimal relative to the MM's kinetic energy and mass, and $F(T_e)$ is represented as [69]:

$$F\left(T_e\right) = \left(1 - \beta^2 \frac{T_e}{T_m}\right) \tag{3.5}$$

T_m is the traditional upper limit on the amount of energy that may be supplied to an atomic electron in one collision with a MM. The maximum energy transfer may be approximated by the equation below since the MM's mass is expected to be significantly larger than that of the electron.

$$T_m = 2m_e c^2 \beta^2 \gamma^2, \tag{3.6}$$

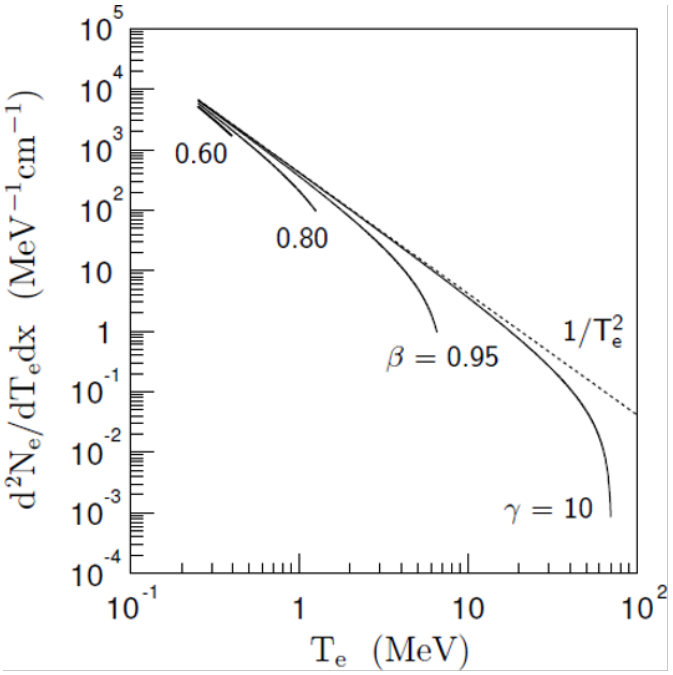

FIGURE 3.5: The distribution of δ-rays with kinetic energy greater than 0.25 MeV generated by a MM with a single Dirac charge g_D, travelling through water, for MM velocities corresponding to $\beta = 0.60, 0.80, 0.95$, and $\gamma = 10$. A spectrum proportional to $1/{T_e}^2$ is represented by the dashed line.

Conversely, while colliding with a MM, the maximum energy that may be transferred to an electron is stated as:

$$T_{\max} \approx 0.69 \cdot T_m, \tag{3.7}$$

The factor 0.69 accounts for the hit parameter's correction [51]. As a result, T_{max} is used instead of T_m in Eq.3.5. After then, the distribution of δ–rays generated by a MM shifts to:

$$\frac{d^2N_e}{dT_e dx} = \frac{2\pi N g^2 e^2}{m_e c^2}\left(\frac{1}{T_e^2} - \frac{\beta^2}{T_e T_{\max}}\right), \tag{3.8}$$

The distribution of δ-rays generated by a MM with charge g_D in water having a kinetic energy of at least T_0 is illustrated in Fig.3.5 for various MM velocities. Fig.3.6 depicts the number of δ-electrons created per centimeter as a function of MM's velocity, with a kinetic energy larger than $T_0 = 0.25\ MeV$. Both are deduced by integrating Eq.3.8 Between T_0 and T_{max}.

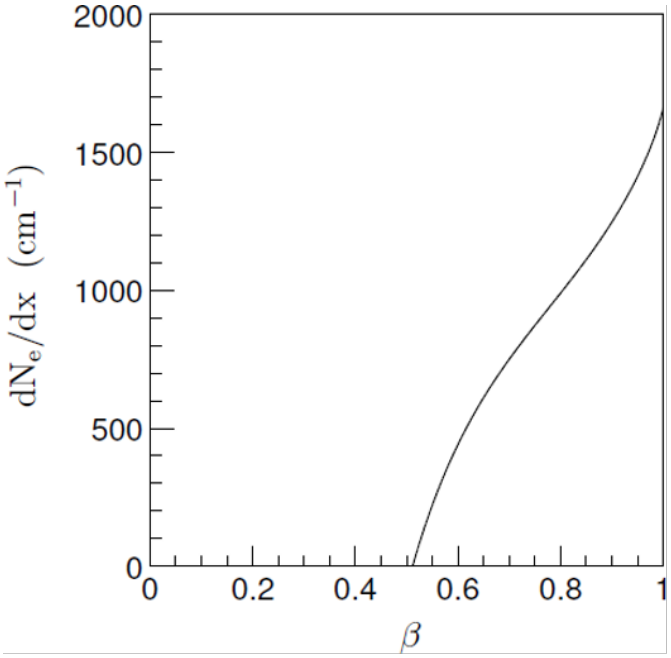

FIGURE 3.6: The overall number of δ-rays with kinetic energy greater than 0.25 MeV generated per centimetre path length by a monopole with g_D as a function of monopole velocity, assuming sea water to be the medium.

δ-ray emission of Cherenkov light

The number of Cherenkov photons released per unit length by an electron with a wavelength within 300 and 600 nm is expressed as:

$$\frac{dN_\gamma}{dx_e} \approx 764 \left(1 - \frac{1}{\beta_e^2 n^2}\right) cm^{-1}\Big), \tag{3.9}$$

where $\beta_e c$ denotes the δ-ray's velocity. It is essential to determine the losses of energies due to ionization of a electron in water before calculating the total number of Cherenkov photons N_γ released by a δ-electron having a starting kinetic energy T_e. The Seltzer and Berger formula [71], which is valid for kinetic energies less than 10 MeV, may be used to compute them:

$$\frac{dE_e}{dx_e} = \frac{2\pi N e^4}{m_e c^2 \beta_e^2}\left(B(T) - 2\ln\frac{I}{m_e c^2} - \delta\right), \tag{3.10}$$

with T denoting the kinetic energy of the δ-ray as it crosses water, δ is the density effect adjustment, and the factor $B(T)$ is only reliant on the kinetic energy and written as:

$$B(T) = \ln\frac{\tau^2\left(\tau^2+2\right)}{2} + \frac{1+\tau^2/8-(2\tau+1)\ln 2}{(\tau+1)^2}, \tag{3.11}$$

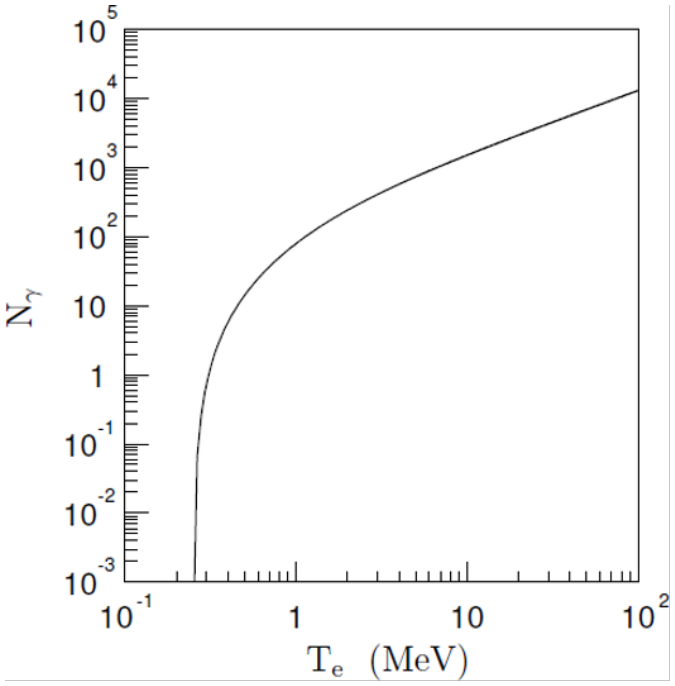

FIGURE 3.7: The total number of Cherenkov photons with wavelengths between 300 and 600 nm released by a δ-ray with initial kinetic energy T_e. Sea water is considered to be the medium.

where $\tau = T/m_e c^2$. The total number of Cherenkov photons released by a δ-ray with kinetic energy T_e is shown in Fig.3.7 and may be calculated as follows:

$$N_\gamma = \int_{T_0}^{T_e} \frac{dN_\gamma}{dx_e} \left(\frac{dE_e}{dx_e}\right)^{-1} dE_e \tag{3.12}$$

As a result, the total number of Cherenkov photons released by all the -δ-rays created per unit length by a mMM passing through may be calculated as:

$$\frac{dn_\gamma}{dx_e} = \int_{T_0}^{T_{\max}} \frac{d^2N_e}{dT_e dx} \int_{T_0}^{T_e} \frac{dN_\gamma}{dx_e} \left(\frac{dE_e}{dx_e}\right)^{-1} dE_e dT_e, \tag{3.13}$$

Fig.3.8 depicts this. Given the high amount of light released by the δ-electrons, a MM with a speed below the Cherenkov threshold might be detected by ANTARES up to speeds on the order of 0.55, in comparison with the light emitted by a muon.

Indirect Cherenkov light angular distribution

It is vital to recognize the angular distribution of photons released by δ-rays created in the passage of a MM in order to simulate them. The Cherenkov photons are released at the standard Cherenkov angle θ_c with regard to the δ-ray direction. The Cherenkov

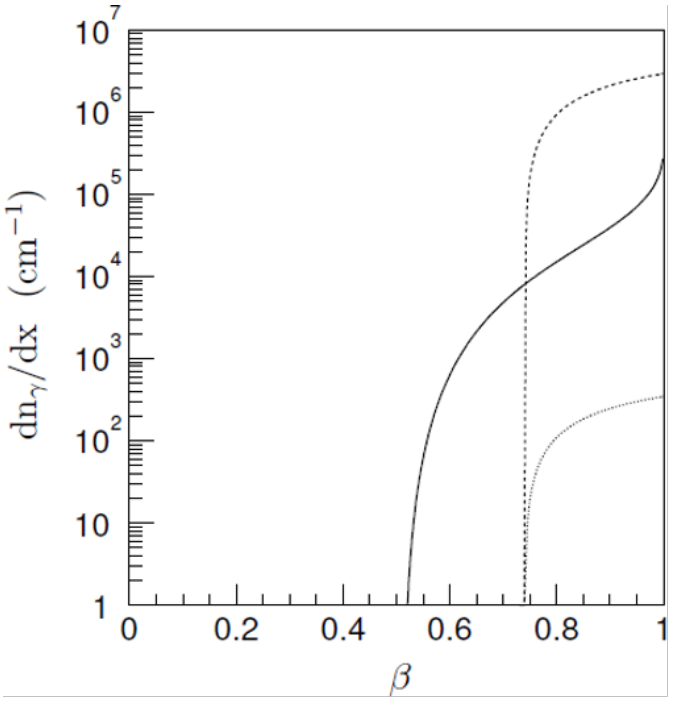

FIGURE 3.8: As a function of the monopole velocity, the total number of Cherenkov photons with wavelengths between 300 and 600 nm released by δ-rays generated per centimetre path length by a monopole with g_D (solid line), the number of Cherenkov photons released directly by a monopole (dashed line) and a minimal ionizing muon (dotted line).

angle is defined as:

$$\cos\theta_c = \frac{1}{n\sqrt{1 - m_e^2c^4/\left(m_ec^2 + T\right)^2}}, \tag{3.14}$$

T denotes the kinetic energy of the δ-ray as it travels through water. Around the path of the δ-ray, photons are scattered equally in the azimuthal angle ϕ_c. To estimate the emission angle θ_γ of δ-ray photons with regard to the direction of the MM, the δ-ray production angle θ_e and the Cherenkov angle θ_c can be combined.

$$\cos\theta_\gamma = \sin\theta_e \sin\theta_c \cos\phi_c + \cos\theta_e \cos\theta_c. \tag{3.15}$$

The integral in Eq.3.13 may be utilized to derive the angular distribution of the photons in θ_γ since both θ_e and θ_c are correlated to the kinetic energy of the δ-rays, Fig.3.9 depicts the outcome. The angle between the δ-ray and the MM is assumed to remain constant along the passage of the δ-ray, ignoring the directional variations of the δ-ray owing to multiple scattering. In the azimuthal angle, the photons have a uniform distribution.

With increased velocity, the angular dispersion of photon emission rises in θ_γ, although all photons are emitted in forward directions with respect to the MM, that is, in directions with $\cos\theta_\gamma \geq 0$.

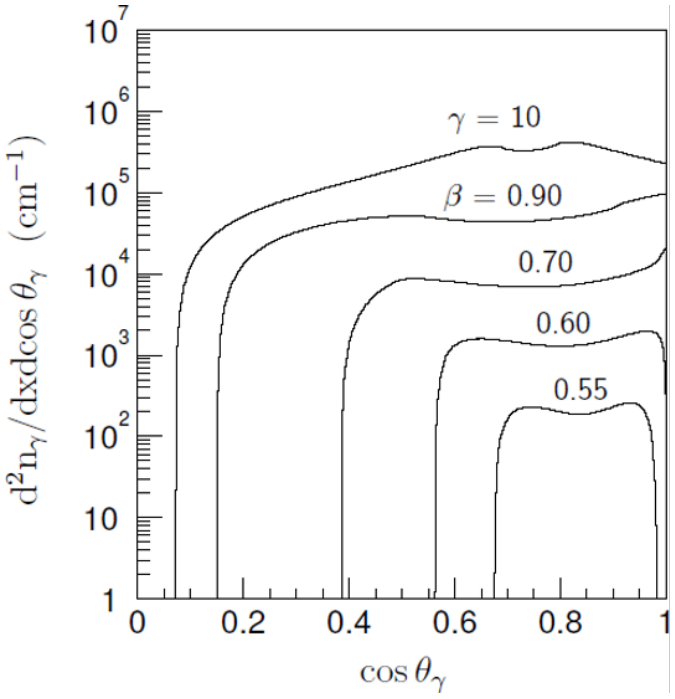

FIGURE 3.9: As a function of the emission angle θ_γ between the photons and the monopole, the angular distributions of the Cherenkov photons released by the δ-rays that are created per centimetre path length by a monopole with g_D in the sea water. It is supposed that the angle between the δ-rays and the monopole is constant. The distributions for β= 0.55, 0.60, 0.70, 0.90, and γ= 10 are illustrated.

A continuous detection of a δ-ray crossing water is due to multiple dispersion of atomic electrons and nuclei. A Gaussian distribution with standard deviation [72] can be used to estimate the distribution of the related scattering angle.

$$\theta_0 = \frac{13.6\text{MeV}}{E_e\beta_e^2}\sqrt{\frac{x_e}{X_0}}\left(1 + 0.038\ln\frac{x_e}{X_0}\right), \tag{3.16}$$

E_e being the total energy of the δ-ray, x_e its travel distance, and $X_0 = 36.1$ cm is the water radiation length [73]. As a result of this correlation, the δ-ray scatters more at lower energies. Because of the δ-ray's energy loss, the dispersion rises along its course. The angle between the δ-rays and the MM varies constantly when multiple scattering of the δ-rays is included, leading to greater angular dispersion of the Cherenkov photon emission. The angular distributions depicted in Fig.3.10 reflect this. Photons can even be released backwards at MM velocities greater than 0.60 c.

The peak of the angular distribution for $\gamma = 10$ is at $cos\,\theta_\gamma = 0.74$. This is attributable to the impact of the most energetic δ-rays produced in directions quite near to the MM direction at this velocity. These δ-rays travel longer distances and are less affected by multiple scattering than less energetic δ-rays due to their comparatively high energy. At the standard Cherenkov angle $cos\,\theta_c \approx 0.74$, they produce a large number of Cherenkov

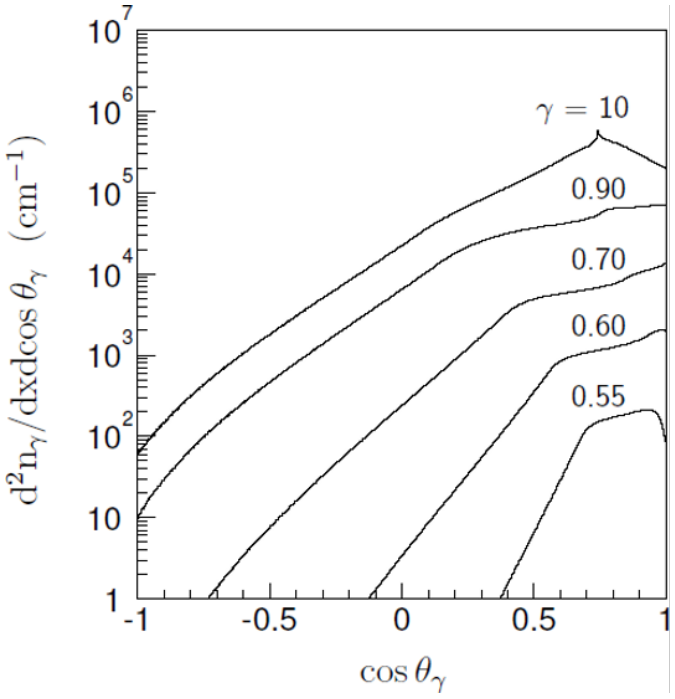

FIGURE 3.10: The Cherenkov photons' angular distributions with multiple scattering of the δ-rays taken into consideration.

photons, most of which are released with the same angle with regard to the MM direction. Since the angular distribution is more dispersed, the monopole signature might alter. As a result, for velocities over the Cherenkov threshold, indirect Cherenkov light is incorporated alongside direct Cherenkov light in the simulation.

3.4 Conclusion

Cherenkov radiation is generated by electrically charged particles crossing the detector in neutrino telescopes. The electromagnetic energy losses of MMs in matter would be comparable to those of an electrically charged heavy nucleus. MMs moving fast enough might emit Cherenkov light in water, something that the ANTARES telescope may observe.

Chapter 4

Data processing and Monte Carlo simulation in ANTARES

4.1 Introduction

This section aims to detail the tasks achieved, software wise, to treat data collected by the ANTARES telescope, simulate the events of the MMs signal and the background (atmospheric muons and neutrinos), as well as the detector's response while taking into consideration the surrounding conditions such as water resolution and PMTs quantum efficiency (QE), bio luminescence, etc. In order to accomplish these tasks, a number of algorithms is used to prepare MC productions to simulate and reconstruct all events of the particles crossing the detector and their interaction with the medium.

4.2 Data processing

The ANTARES telescope registers data under the form of runs, specified by a run number and a duration (12 hours of data taking time per run usually). These runs are stored in specific disks (HPSS: High Performance Storage System) at CC-Lyon (Centre de Calcul de Lyon), and once registered they are made available to be studied for different analyses.

The data collected by the ANTARES detector is then compared to simulated particles of the standard model (muons and neutrinos), as well as the MMs signal which is the aim of our study.

4.3 Monte Carlo simulation and reconstruction

The events simulation was carried out by firstly generating the fundamental parameters of the particles in question (muons, neutrinos and MMs), these parameters consist of the position, time of arrival, direction, velocity, energy among others. Next, the estimations regarding the propagation of these particles while crossing the Earth and water were set, all while being cognizant of the propagation of resulting particles from interaction proprieties and decay mechanisms. Afterwards, Cherenkov light is generated while the simulated particles are near the detector. Then the response of the PMTs is estimated while considering their QE, along with other Optical Module (OM) electronics. Finally, the last step consists of the triggering, by keeping only events passing the trigger conditions, thus minimizing noise influence.

The codes and algorithms used to put in motion the simulation are described in the up-coming sections.

Once the simulation of events is attained, each production of the simulated particles undergoes a reconstruction procedure, during which tracks are generated using the simulation parameters of the particle. Real data stored by the ANTARES telescope undergoes the same procedure.

In this work, the reconstruction utilizes the arrival time of Cherenkov light on the PMT, along with its position and amplitude. The BBfit algorithm described in the upcoming section was used for the reconstruction.

4.3.1 Magnetic Monopole simulation

MMs were simulated as up-going events with a charge equal to one unit of Dirac charge: $g = g_D$. The simulation of MMs was carried out across 10 equal intervals of velocity $\beta \in [0.5500, 0.995]$ described in table 4.1.

The simulation of MMs was performed, independently form the MMs mass, using a MC code developed by Bam van Rens [74] which was based on GEANT3 [75]. MMs were generated with an isotropically scattered direction. The emitted photons (propagation and detection) were treated inside of a simulated cylinder around the detector (CAN), having a larger radius than the detector to consider the large amount of light emitted by MMs. Fig.4.1 represents the CAN where MMs events are generated.

β range number	β range simulated
1	[0.5500, 0.5945[
2	[0.5945, 0.6390[
3	[0.6390, 0.6835[
4	[0.6835, 0.7280[
5	[0.7280, 0.7725[
6	[0.7725, 0.8170[
7	[0.8170, 0.8615[
8	[0.8615, 0.9060[
9	[0.9060, 0.9505[
10	[0.9505, 0.9950[

TABLE 4.1: Velocity ranges considered for MMs simulation.

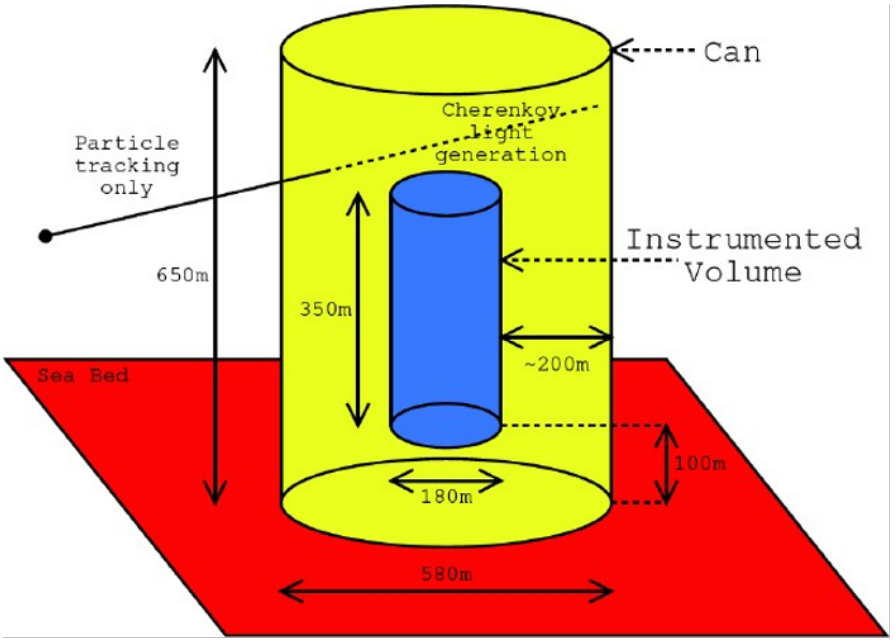

FIGURE 4.1: The virtual volume in yellow represents the CAN where MM events are generated, it encircles the detector (instrumented volume) shown in blue, the sea bed is represented in red. The radius of the CAN takes into account the amount of light to be generated by MMs.

Magnetic Monopole generation

The generation of MM tracks in the CAN surface relies on a package named Genmon, derived from genneuV5r1 [75]. The code generates MM tracks in a given velocity range, permitting the use of different CAN sizes for each velocity range, which is advantageous since there is a high dependence between the light yield and the velocity of a particle. The energy values of the cut parameter establish the velocity range. the MM is defined as a particle with a mass of $10GeV$ and a particle ID of 666 in Geamon (detailed in

4.3.1). The following equation describes the energy as a function of the velocity:

$$E = \frac{10[GeV]}{\sqrt{(1-\beta^2)}}. \tag{4.1}$$

The code uses velocity intervals ranging from 0.55 to 0.995, with logarithmic interpolation applied to compute the Cherenkov emission for unavailable intervals.

Magnetic Monopole tracking

GEASIM [76] is the basis for the geamon code used for MM tracking. It takes the genmon files as input and outputs event files that include the detector's reaction to the MM signal. The light intensity I as a function of the length traversed L by the photons and the length of attenuation λ_{tt} has been factored in the simulation for direct Cherenkov radiation.

$$I(L) \propto \frac{e^{-L/\lambda_{att}}}{L} \tag{4.2}$$

This light intensity for indirect Cherenkov radiation is:

$$I(L) \propto \frac{1}{L^2} e^{-L/\lambda_{att}} \tag{4.3}$$

because of photons' quasi-isotropic nature (see Fig.3.10).

Magnetic Monopole Triggers

The data collected by the ANTARES telescope is subjected to a set of triggers, as previously stated. As a result, evaluating the trigger efficiency in ANTARES for MM is critical. Only hits exceeding a threshold of 3 photo-electrons (pe) are evaluated in general. Before going over the many triggers available, here are some frequent notations:

- L1 denotes a hit with a large amplitude (3 pe) or the occurrence of at least two hits on the same storey in a 20-ns interval.
- T3 is a 100 ns or 200 ns interval coincidence of two L1 on two storeys between three adjacents.

Other ANTARES triggers are provided for different applications (or other analyses). Given the massive quantity of light that MMs would release in a neutrino telescope, it is vital to examine the various triggers and select one that is optimal for MMs (trigger efficiency). T3 is the most effective of all the triggers shown in Fig.4.2. As a result,

only T3 triggers are taken into account in this study. The other triggers 3S and 3N are defined below as given in [77]:

- 3N: This trigger is optimized for the passage of muons in the detector, if at least 5 L1 are registered in a time window of between 2.2μm before the first hit, and 2.2μm after the last hit, the event is kept.
- 3S is based on the same algorithm as the 3N trigger, if at least 7 L1 are remaining, the event is kept, and all hits present in a window of $\sim$ 4μm before and after, respectively the first and the last hit, are then recorded.

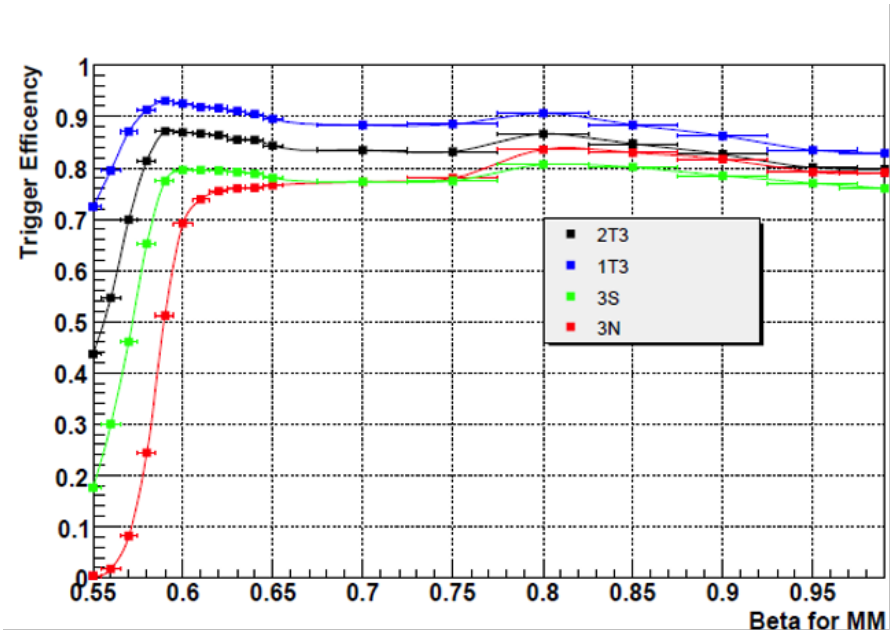

FIGURE 4.2: Up-going magnetic monopoles' trigger efficiency as a function of velocity (β).

4.3.2 Background simulation

The interactions of atmospheric muons and neutrinos are simulated before reaching the CAN, including their possible secondary particles (differently from MMs). The thorough modeling of Cherenkov photon propagation in the detector, as well as the response of the PMTs, is then done after these particles are in the CAN. Finally, the telescope's acquisition electronics and triggering devices, as well as the surrounding background noise, are all covered in the simulation. The generator MUPAGE [78], which is based on the direction and energy distributions of muons in the medium as a function of their bundle multiplicity [79], is used to simulate atmospheric muons. MUPAGE generates muon events on the virtual cylinder's surface.

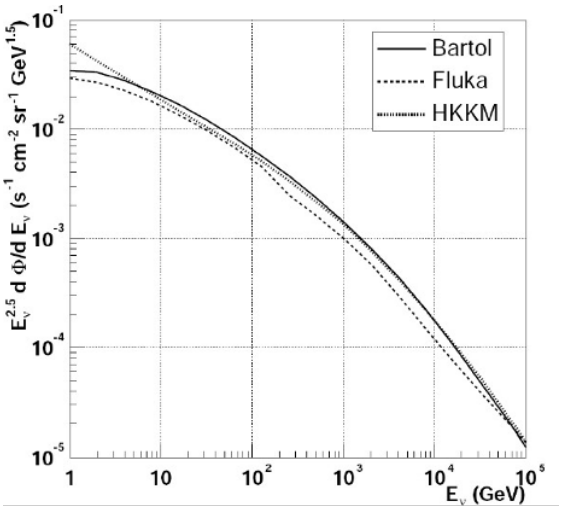

FIGURE 4.3: Atmospheric neutrino spectrum estimated with the models Bartol [80], Fluka [81], and HKKM [82] with energies $\leq 10^5$ GeV.

The software GENHEN [83, 84] is used to simulate up-going atmospheric neutrinos from the decay of pions and kaons, adopting the Bartol group's model [80, 85], which does not involve the decay of charmed particles. The Bartol model [80] was merged with the RPQM model [86] since they both predict a greater neutrino flux and are most conservative.

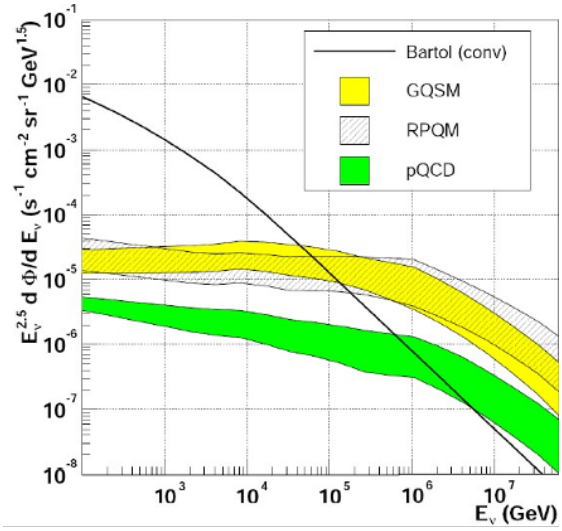

FIGURE 4.4: The flux of atmospheric neutrinos from the decay of charmed mesons, estimated with the models GQSM, RPQM, and pQCD [86] and compared to the flux predicted by the Bartol model.

GENHEN employs MUSIC [87] package to simulate muon energy loss and multiple scattering in order to propagate muons into the CAN. Only events having a chance of reaching the CAN are saved and used in the following step. The software KM3 [88] mimics Cherenkov photons generated, as well as their dispersion, absorption, and scattering in water, by propagating muons in the CAN. The photons generated by neutrinos

interacting within the CAN are also simulated using the GEASIM tool [76]. The efficiency and optical characteristics of PMTs are taken into account while simulating their response.

4.3.3 Reconstruction

The BBfit [89] reconstruction algorithm has been created as a dependable reconstruction approach that does not require accurate location calibration. Its tight hit selection ensures a solid up-down separation while maintaining efficiency. The BBfit idea is driven by the fact that a detector line and a muon track would both be linear in space. Besides the exceptional scenario where these two lines are perfectly parallel (as in the case of a precisely vertical track), a point of closest approach to the detector line can be defined on the muon track, around which The majority of the Cherenkov light must be visible. This is factored in both the hit selection and fitting algorithms. The fit is limited to hits resulting from direct Cherenkov photons, it is then simplified by excluding tails caused by scattering and electromagnetic activity. A χ^2 like function is defined and minimized.

BBfit ignores the geometry of the three optical modules on a storey, which is defined as a point in space that is centered on the detector line. The operation always begins with the snapshot hits list, that are only evaluated if triggered hits are not present (in LED beacon events for instance). BBfit starts by calibrating the time and charge, however the automated selection of a calibration set, based on the approach described in [90], is the default method for real data. The hit amplitudes a_i are reported in photo-electrons and the calibrated hit timings t_i are given in ns with regard to the commencement of the run. The hit times are reset to time differences with respect to the first triggered hit in order to avoid excessive numbers during the fitting operation.

In the fitting operation, just one hit per story is permitted. As a result, the calibrated snapshot hits of a physics event are treated as follows:

- Regardless of which optical module they originate from, all hits from the same storey are time sorted.
- Hits with a timing difference of less than 20 ns are merged by combining their amplitudes while maintaining the timing of the earlier hit.
- When hits from multiple optical modules are merged, the merged hit receives a 1.5 photo-electron extra charge (once only).

When compared to a single high charge pulse, the extra charge lends a larger weight to occurrences between two hits on distinct optical modules. All future processes are dependent on the hit list that has been pre-treated.

The list of selected hits is assessed before any fit is performed. If there is less than 5 hits in the list, no fit attempt is conducted. If all of the selected hits are on a single detector line, a single line fit operation is initiated. A multi-line fit approach is used only if the hits are spread across many detector lines.

Track of a particle

A track is defined as a line in space depicting the passage of the particle, as seen in Fig.4.5 describing the form of a track in a neutrino telescope. Repeated scattering and other phenomena that may cause the particle to stray from its straight path are not taken into account. In vacuum, the particle is expected to travel at the speed of light (the code uses the value $0.3m/ns$). Each of the track's space-time points can be specified as follows:

$$\vec{p}(t) = \vec{q}(t_0) + c\,(t - t_0)\,\vec{v} \tag{4.4}$$

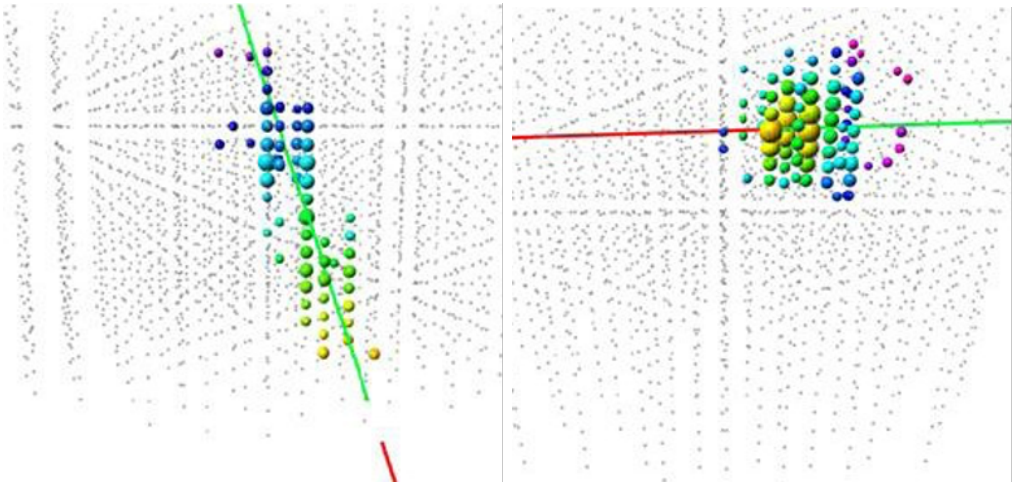

FIGURE 4.5: Left: depiction of the track of a particle crossing a neutrino telescope. Right: an event representing a bright point in a neutrino telescope. The gray points represent the floors of the telescope.

At time t_0, the particle crosses point $(\vec{q})$ and proceeds in the direction $\vec{v}$. Redefining t_0 allows $(\vec{q})$ to be moved down the track, as a result, there are five factors that define the track Fig.4.6: three values to fix $(\vec{q})$ for a specific time and two angles to define $\vec{v}$. Now assume a detector line that is perfectly vertical along the z-axis, i.e. (0; 0; z). The closest point between the detector line and the particle track may be determined solely

geometrically, along the z-axis, this point is:

$$z_c = \frac{q_z - v_z(\vec{q} \cdot \vec{v})}{1 - v_z^2} \tag{4.5}$$

which the particle crosses through in time:

$$t_c = t_0 + \frac{q_z v_z - (\vec{q} \cdot \vec{v})}{c\,(1 - v_z^2} \tag{4.6}$$

at a distance:

$$d_c = \sqrt{p_x^2\,(t_c) + p_y^2\,(t_c) + (p_z\,(t_c) - z_c)^2}. \tag{4.7}$$

In the case where the track is perfectly vertical, hence parallel to the detector line, then $t_c = t_0$, and $z_c = q_c$ is selected. Rotations around the z-axis have no impact on the layout

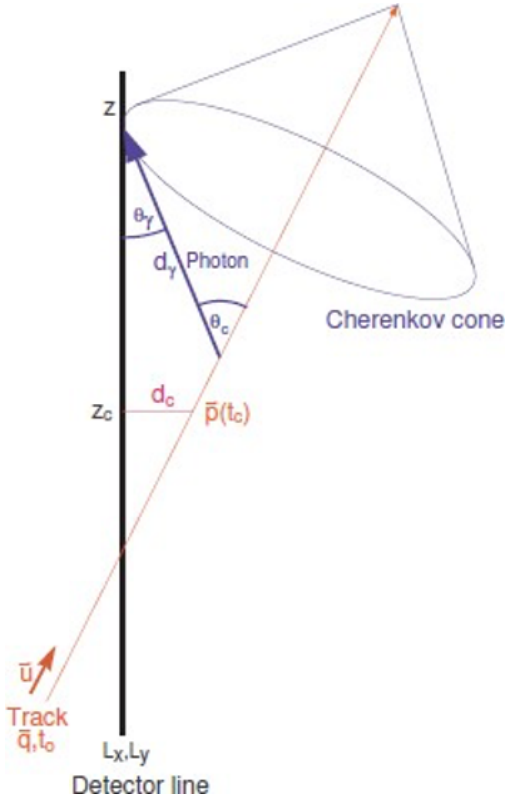

FIGURE 4.6: The track, as well as the variables used to characterize it.

of a track and a single detector line. The track may be easily re-characterized in terms of z_c, t_c, d_c, and v_z, with the latter being the cosine of its zenith angle. This indicates that just four parameters are left to define the track. To construct a fitting function, Cherenkov photon's arrival time t_γ at the detector line point (0; 0; z), its associated travel path d_γ, and its inclination with respect to the detector line $cos(\theta_\gamma)$ are needed to be known. These three values can be calculated from the four track parameters defined above.

$$d_\gamma(z) = \frac{n}{\sqrt{n^2-1}}\sqrt{d_c^2 + (z-z_c)^2\,(1-v_z^2)} \tag{4.8}$$

$$t_\gamma(z) = (t_c - t_0) + \frac{1}{c}\left((z-z_c)\,v_z + \frac{n^2-1}{n} d_\gamma(z)\right) \tag{4.9}$$

$$\cos\theta_\gamma(z) = \left(1-v_z^2\right)\frac{z-z_c}{d_\gamma(z)} + \frac{v_z}{n}. \tag{4.10}$$

For Cherenkov photons of a particular wavelength, these equations are precise. The effects of dispersion and group velocity, as well as delays caused by light scattering in a medium, are not factored. The code employs a refractive index of $n = 1.38$.

Bright point

A bright point, unlike a particle track, is a point-like light source that releases a single light flash at a specific time, (see Fig.4.5). It is assumed that the light emission is isotropic. The bright point model applies not just to artificial light sources like LED and laser beacons, but also to sparks (as seen in certain optical modules) and light from hadronic and electromagnetic showers, where the shower's real extent is much smaller than the detector's relevant scales. The position $\vec{q}$ and the time t_0 of a bright point are the factors that characterize it. It is straightforward to notice that for a bright point z_c = q_z and $t_c = t_0$ in the same way as the point of closest approach is defined for particle tracks.

$$d_c = \sqrt{q_x^2 + q_y^2} \tag{4.11}$$

The three parameters z_c, t_c and d_c permit the complete specification of the bright point with regard to a singular detector line at (0; 0; z), reducing the number of parameters by one in this instance. In the same way as proceeded for a particle track, the photon arrival time t_γ, path length d_γ, and angle with respect to a specific arrival point z along the detector line can be determined.

$$d_\gamma(z) = \sqrt{d_c^2 + (z-q_z)^2} \tag{4.12}$$

$$t_\gamma(z) = t_0 + \frac{n}{c} d_\gamma \tag{4.13}$$

$$\cos\theta_\gamma(z) = \frac{z-q_z}{d_\gamma}. \tag{4.14}$$

In the case of particle tracks, it is supposed that all photons have the same wavelength, resulting in a refractive index of 1.38.

Fit function

As in a typical χ^2 fit, the fitting function employs the time difference between the hit times t_i and the expected arrival time of photons from the track or bright point t_γ. The predicted amplitude versus distance relation of the measured hit amplitudes a_i is also used.

$$Q = \sum_{i=1}^{N_{\text{hit}}} \left[\frac{(t_\gamma - t_i)^2}{\sigma_i^2} + \frac{a\,(a_i)\,d\,(d_\gamma)}{< a > d_0} \right]. \tag{4.15}$$

For $a_i > 2.5pe$, the timing error σ_i is set to $10ns$, otherwise, it is set to $20ns$. This may appear high in comparison to the ANTARES PMTs' transit time spread of $1.3ns$, but it has been verified by examining the time residuals of usual track fits.

To prevent consequences from high theoretical amplitudes, the second term is not arranged as a difference between theoretical and observed amplitude. The selected form, on the other hand, penalizes the combination of high amplitude and large distance. To account for the fact that higher energy tracks or showers would emit more light at the same distance, the result is normalized by the average amplitude $< a >$. The weight between the two terms is balanced by the normalization $d_0 = 50m$. The photon travel lengths d_γ and hit amplitudes a_i are not calculated directly from the calibrated detector readings. The amplitudes are first adjusted for the floor's angular acceptance. From the arrangement of optical modules in a floor and the related angular acceptance function of a single optical module, a very basic form (moon phases) may be numerically generated. As a result, the adjusted hit amplitude a_i' is:

$$a_i' = \frac{2a_i}{\cos\theta_\gamma + 1} \tag{4.16}$$

These adjusted hit amplitudes are used to derive the average amplitude $< a >$:

$$< a >= \frac{1}{N_{hit}} \sum_{1}^{N_{hit}} a_i' \tag{4.17}$$

The amplitudes are further modified before being utilized in the fit function:

$$a\,(a_i) = \frac{a_0 a_i'}{\sqrt{a_0^2 + a_i^2}}. \tag{4.18}$$

The function $a(a_i)$ produces an artificial saturation so that $a_i \ll a_0$ returns $a \approx a_i'$, whereas $a_i \gg a_0$ returns $a \approx a_0$: the saturation value is $a_0 = 10pe$. This reduces the impact of the significant dispersion in the dynamic ranges of the various modules, which

is not currently simulated. The photon travel distance is treated in a similar fashion:

$$d\,(d_\gamma) = \sqrt{d_1^2 + d_\gamma^2}. \tag{4.19}$$

For long distances, $d_\gamma \gg d_1$, we find back $d \approx d_\gamma$, but for short distances, $d_\gamma \ll d_1$, we get $d \approx d_1$ with $d_1 = 5m$. This prevents the fit object from being dragged too far towards the detection line.

Minimization

The minimization is performed using the MIGRAD function from the MINUIT package [91]. The fit object is specified by its point of closest approach, i.e. z_c, t_c and d_c, and v_z for the track fit, to conduct a single line fit. For a given particle track or bright point, the equations 4.8 through 4.12 are employed to calculate t_γ, d_γ, and angle $cos(\theta_\gamma)$. The formulae for multiline fits are the same. A loop is run across all detector lines with chosen hits, and a coordinate transformation is applied to each line to place it at the nominal point $(x, y) = (0, 0)$. Because the multi-line arrangement disrupts rotational symmetry, all parameters must be determined to calculate the track or bright point, as shown in Table 4.2.

	Single line	Multi line
Track	4	5
Bright point	3	4

TABLE 4.2: The number of fit parameters.

As a result, two parameters are proposed to define the quality of these reconstructions: $t\chi^2$ for the track fit and $b\chi^2$ for the bright-point fit. The reconstruction assigns a $t\chi^2$ and a $b\chi^2$ value to each event, such that if $t\chi^2 < b\chi^2$, the event should be classified as a track, and if $t\chi^2 > b\chi^2$, it should be classified as a bright point.

4.3.4 Run-by-run Monte Carlo

The circumstances in a maritime environment are not always steady and consistent. In an undersea neutrino telescope like ANTARES, variations impact data acquisition. Biological [10] and physical [92] events exhibit changing trends on seasonal time frames, resulting in a periodic shift in the background optical rates recorded at the detector. Because the optical rates are affected by the sea current velocity, there are also changes on the short-term scale. Aside from external factors, the detector components may

not collect data continually due to temporary or permanent malfunctions of the optical modules or a lack of connection to a section of the apparatus; also, the detector lines are constantly moving due to the sea current. Finally, the trigger algorithms that are applied to the data during the detector's lifetime can be changed. All of these effects should be reproduced by a credible Monte Carlo simulation of the detector.

Extracting relevant information straight from the data is an efficient technique to adjust for fluctuations in the optical background. This data is extracted from raw data files by the TriggerEfficiency tool. It takes into account the counting rate in brief data stream segments (approximately 100 ms) and simulates the matching optical background based on the detected charge distribution of hits. The DAQ conditions for each run (status of each detector component, active triggers, data filtering settings) are saved in the ANTARES database, accessible by the TriggerEfficiency code, and utilized during the simulation.

The output is in the same format as the original data and is processed using the available reconstruction method to obtain physics information from the data. The run-by-run approach [126] considerably enhanced data/MC agreement and allowed for better monitoring of the data acquisition's time evolution.

4.3.5 Blinding approach

The study presented in this work is based on ten years of ANTARES data gathered between January 2008 and December 2017, yielding 2480 active days in total. The analysis is based on an unblinding approach, which consists of executing the research using MC production and utilizing a test data sample equivalent to 10% of the whole data set (run numbers ending with 0) to create a comparison data/MC.

4.4 Conclusion

The blind approach enables the use of a sample of 10% of the totality of the telescope data, to be compared with the simulation of MMs and atmospheric background, after the reconstruction of events. This sample is mainly used to compare data and MC distributions, which is detailed in the up coming chapter. In order to achieve the best predicted sensitivity, the event selection and optimization of the cuts will be detailed in the next chapter as well.

Chapter 5

Search for Magnetic Monopoles with ten years of ANTARES data

5.1 Introduction

The aim of this section is to calculate the Flux Upper Limit on MMs for the ANTARES telescope. To do so a blinded strategy has been followed, and a data/MC comparison has been carried out using a 10% data sample collected by the ANTARES telescope throughout a 10 year period between 2008 and 2017. For a refined isolation of the MM signal from the background, the optimization of the Model Rejection Factor was performed on the totality on data and MC considered in this analysis.

The results discussed in this section have been published in [68].

5.2 Analysis strategy

To calculate the upper limit on the flux of MM for the ANTARES telescope, the isolation of the MM signal from the background consisting of atmospheric muons and neutrinos is necessary. This was carried out by firstly applying preliminary cuts to reduce the atmospheric background, the following step is the verification of Data/MC agreement for different distributions relevant to the analysis. Afterwards, the determination of the discriminant variables essential to produce the cuts leading to the isolation of the signal from the background, these cuts are then optimized using the Model Rejection Factor method [93], which allows for the calculation of the sensitivity and consequently the upper limit on the flux using the Fieldman-Cousins [94] formula.

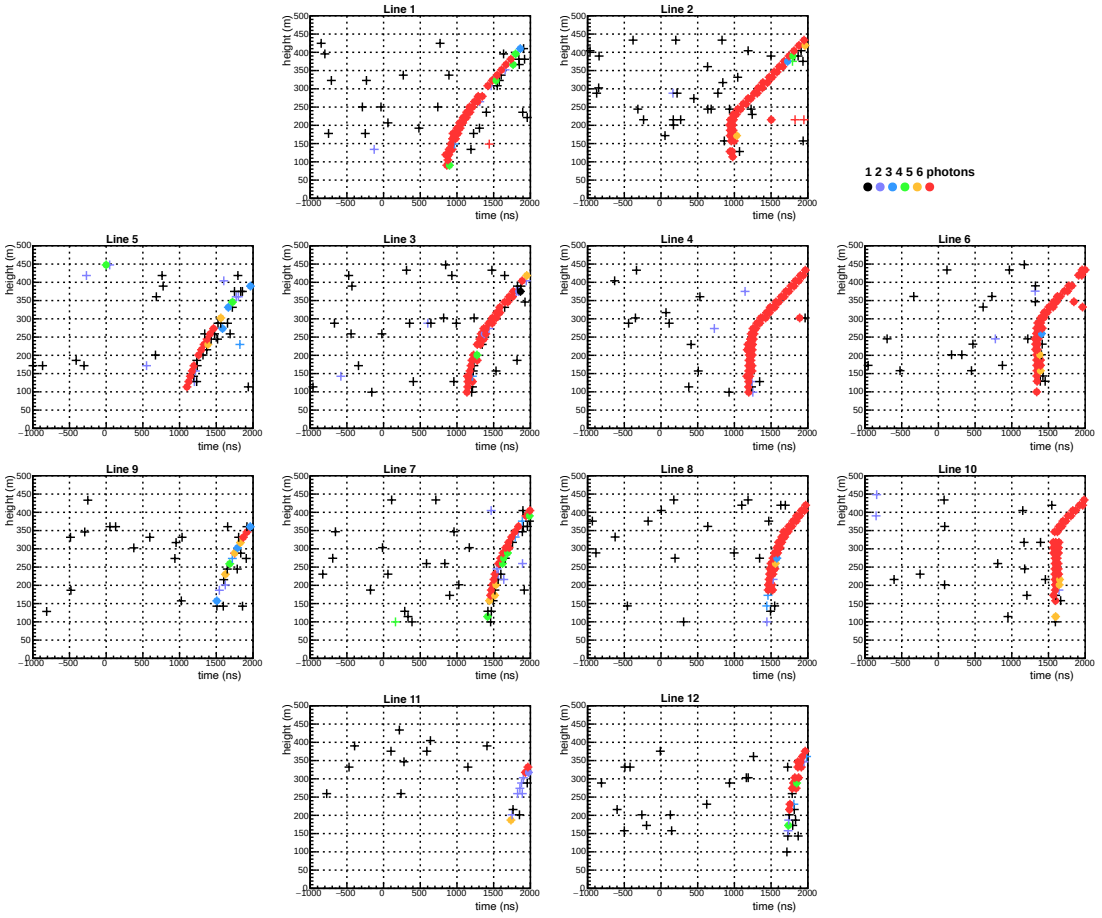

FIGURE 5.1: Event display of a simulated magnetic monopole travelling through the ANTARES telescope after crossing the Earth in the range $\beta \in [0.9505, 0.9950]$ (upgoing event). Each graph represents a single detector line, the octagonal arrangement approximates their placement on the sea floor, and the detected photons are shown as a function of their arrival time (x-axis) and elevation above the sea floor (y-axis), with their amplitude color-coded. Background photons (black crosses) are clearly distinguished from monopole signals (red hyperbolae).

5.2.1 Event selection

For this analysis, a derivative version of the fast tracking method BBfit is utilized. The method looks for a straight line (i.e. a track-like event) that is compatible with the Cherenkov photon emission hypothesis' large amplitude hit placements and duration while allowing for a variable effective particle speed $v_{reco} = \beta_{reco} \cdot c$. Fig.5.1 depicts an example of a simulated MM event for $\beta \in [0.9505, 0.9950]$.

Depending on the velocity of the simulated MMs, two separate approaches are followed in this study:

- Fast MMs are simulated using $\beta \in [0.8170, 0.9950]$, divided into four equal intervals, and reconstructed with $\beta_{reco} = 1$. Relativistic MMs are expected to release

substantially more Cherenkov radiation in the detector than muons in this velocity range, which is essential to separate the signal from the background. As seen in Fig.3.4, the light emission of a single muon is less than two orders of magnitude lower than that of an MM. During the ten years of data analysis, however, muon bundle events with multiplicities up to ~ 100 are foreseen. The number of storeys with fired PMTs (N_{sh}) is employed in the reconstruction algorithm [89] to distinguish signal from background in this velocity range. Each point in Fig.5.1 represents a "storey hit," in which the position coordinates are represented by the center of the storey, the time considered is that of the first hit, and the charge is equal to the total hit charges. The amount of light released by the particle is approximately proportional to N_{sh}. Candidate MMs with a high value of N_{sh} generate significantly more light than other background particles (muons and neutrinos) reaching the detector's deep position.

- Slower MMs are simulated in the interval of $\beta \in [0.5500, 0.8170[$ where the events are divided into six evenly spaced interval. The variable β_{reco} is utilized as a free parameter in the reconstruction algorithm to seek MMs simulated with velocities between $[0.5500, 0.8170]$. Because atmospheric muons and neutrinos are mainly reconstructed as relativistic ($\beta_{reco} \sim 1$) particles, the appropriate output value in the range $\beta_{reco} \in [0.5500, 0.8170[$ is applied as primary cut to isolate the signal from the background.

5.2.1.1 Preliminary cuts

In order to further optimize data taking conditions, some basic preliminary cuts are imposed to the productions considered [95]. Since the interest of this work revolves around up-going MMs, a selection cut on the zenith angle θ_{reco} is elected, the condition $\theta_{reco} > 90°$ selects up-going events, using the Earth as a filter resulting in a significant rejection of background stemming from down-going atmospheric muons and neutrinos.

Another condition is required to improve the quality of events reconstruction, which is the selection of events that were reconstructed on at least 2 lines of the detector.

However, occasionally the reconstruction of some tracks is not perfect, validating the usage of the quality of the track reconstruction parameter $t\chi^2$ (Fig.5.2). Hence another cut on this parameter is designated: $t\chi^2 \leq b\chi^2$, favoring track events rather than bright point ones.

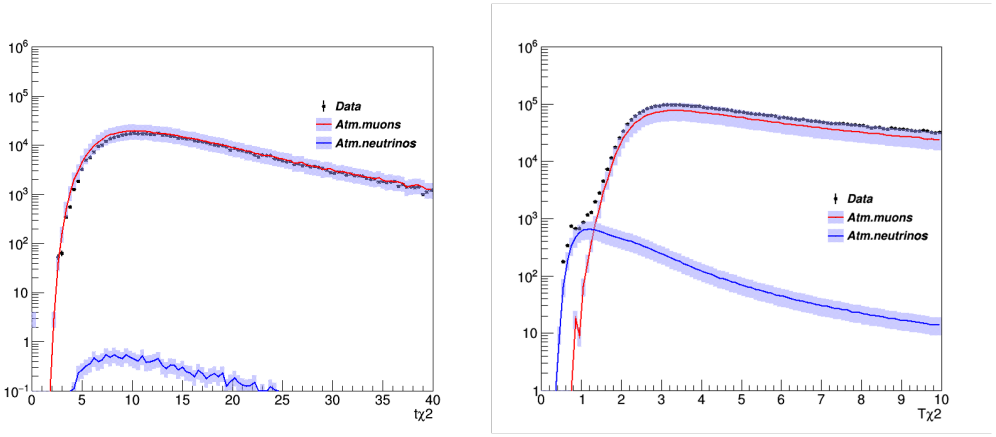

FIGURE 5.2: The distribution of $t\chi^2$ for atmospheric muons (red histogram) and atmospheric neutrinos (blue histogram) with a 35 percent uncertainty range (gray band) and the data (10% sample) is depicted in black dots. The plot on the left corresponds to the interval [0.5500, 0.5945[of β and has an extra cut on β_{reco} in the same interval, whereas the plot on the right relates to the range [0.8615, 0.9060[of β. Both graphs represent ten years of studied data.

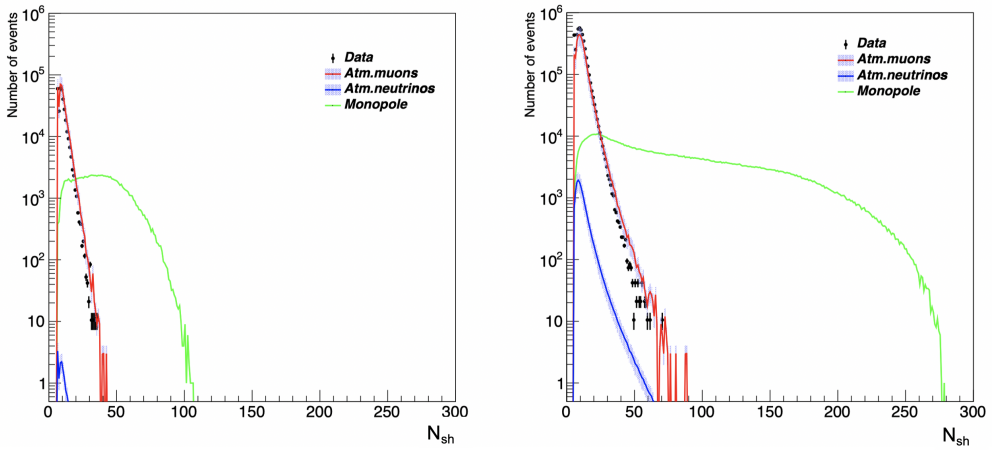

FIGURE 5.3: The distribution of N_{sh} for atmospheric muons (red histogram) and atmospheric neutrinos (blue histogram) with a 35 percent uncertainty range (gray band). The data (10% sample) is depicted in black dots, while the MMs signal is shown in green. The plot on the left corresponds to the interval [0.5945, 0.6390[of β and has an extra cut on β_{reco} in the same interval, whereas the plot on the right relates to the range [0.8615, 0.9060[of β. Both graphs represent ten years of studied data.

5.2.1.2 Discriminant variables

In this study, the N_{sh} parameter which was presented before and illustrated in Fig.5.3, is used as an event energy proxy and considered as the first discriminant variable. The quality parameter of the track reconstruction $t\chi^2$, is combined with the brightness of the event N_{sh}, reduced by the number of free parameters, N_{df}, and has been used by the reconstruction algorithm to separate the MM signal from the background. This variable denoted α, represented in Fig.5.4, is chosen as the second discriminant variable and is

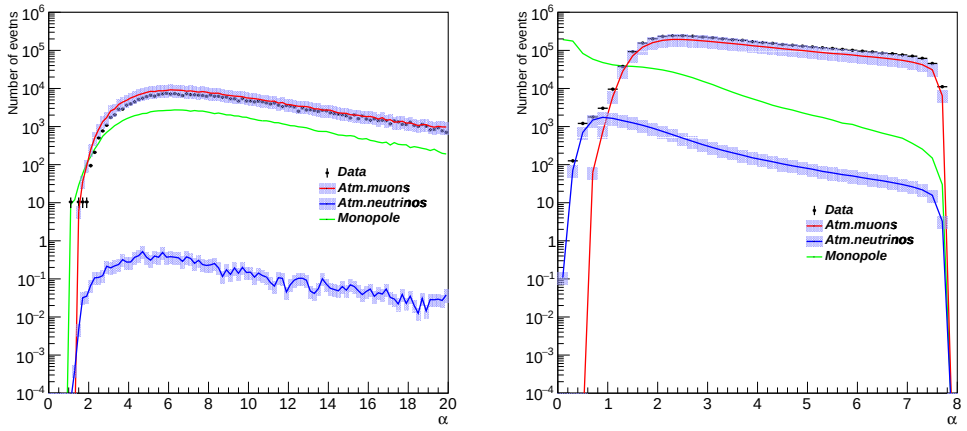

FIGURE 5.4: Distribution of α showing atmospheric muons in the red histogram, atmospheric neutrinos in the blue histogram with an uncertainty band of 35% filled in gray, data (10% sample) represented in black points, and MMs signal in the green histogram. The plot in the left corresponds to the interval [0.5945, 0.6390[of β and has an additional cut (beside the initial cuts described in section 6) on β_{reco} ($\beta_{reco} \in$ [0.5945, 0.6390[), while the plot on the right corresponds to the range [0.8615, 0.9060[. Both plots correspond to ten years of analyzed data.

empirically written as follows:

$$\alpha = \frac{t\chi^2}{1.3 + (0.04 \times (N_{sh} - N_{df}))^2}, \tag{5.1}$$

When β_{reco} is included in the reconstruction, as it is for slow MMs ($\beta_{reco} \in$ [0.5500, 0.8170[), N_{df} is equal to 6, and when β_{reco} is fixed to 1, it is equal to 5, corresponding to nearly relativistic MMs.

Fig.5.5 depicts the N_{sh} vs α event distribution for MMs simulated in the ranges [0.5945, 0.6390[and [0.8615, 0.9060[. By applying cuts on N_{sh} and α, the MMs signal, in the upper left corner, can be distinguished from the background, which is superimposed on the signal in the figure.

To compensate for the deficiency of statistics in the N_{sh} distribution for the sample of atmospheric muons, an extrapolation in the signal region is performed by fitting the histogram with a Landau distribution, as shown in Fig.5.6. The contribution of this extrapolation is included in the total number of background events used to compute the sensitivity.

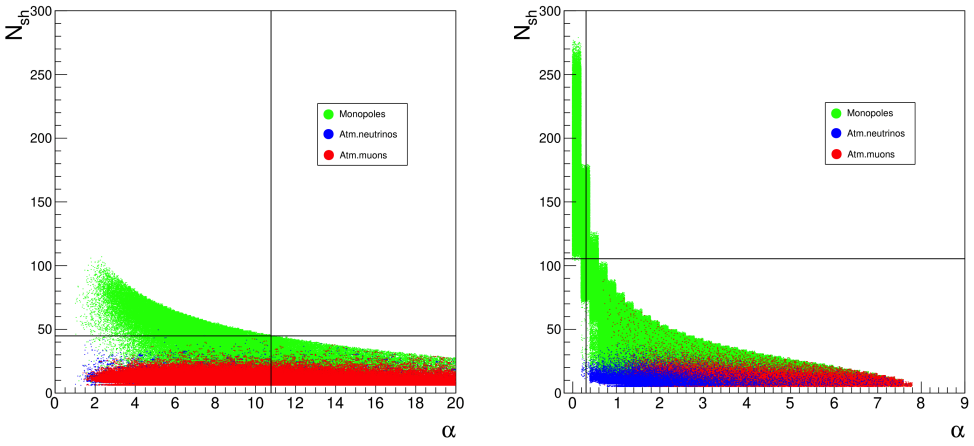

FIGURE 5.5: Scatter-plot of the two variables α and N_{sh} for the MMs signal simulated within the range $\beta \in$[0.5945, 0.6390[(left plot) with an extra cut (in addition to the initial cuts stated in section 6) $\beta_{reco} \in$ [0.5945, 0.6390[, and $\beta \in$ [0.8615, 0.9060[(right plot). The background zones comprised of atmospheric muons in red and atmospheric neutrinos in blue are distinguishable from the MM's signal zone in green. The optimal cuts are indicated by the black lines. Both graphs represent ten years of analyzed data.

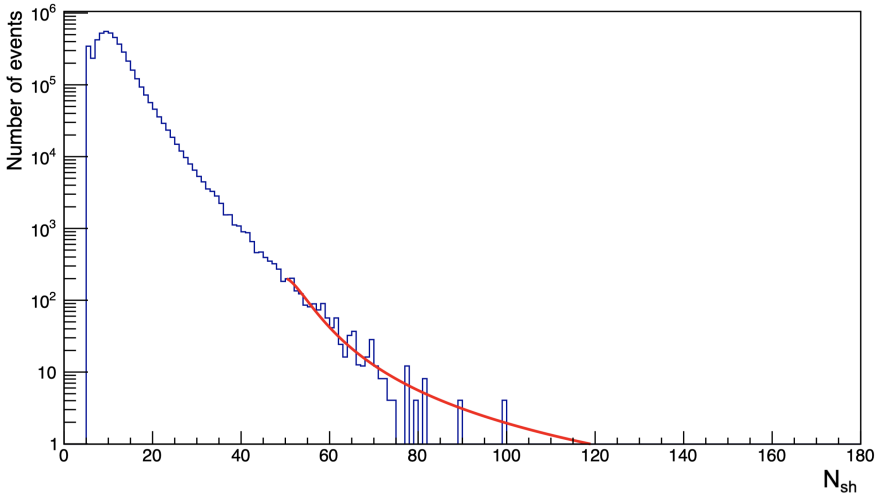

FIGURE 5.6: The N_{sh} distribution for simulated atmospheric muons. The extrapolation in the signal region using a Landau function is represented by the red line. When calculating the sensitivity, the extrapolation is taken into consideration. The graph represents ten years of data analysis.

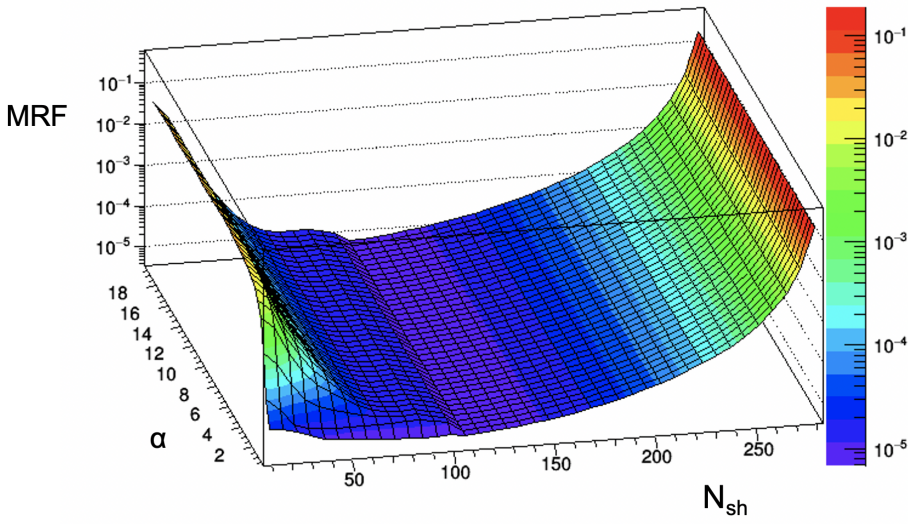

FIGURE 5.7: The model rejection factor MRF as a function of α and N_{sh} cuts for the case of $\beta_{reco} \in [0.7725, 0.8170[$.

5.2.2 MRF optimization

The Model Rejection Factor is optimized for each velocity interval using α and N_{sh} cuts to provide the optimum sensitivity. After applying the cuts on α, N_{sh}, and β_{reco} (with the latter applied in the six bins with lower velocities), the selection efficiency for signal events in the 10 intervals varies from 16% to 51%. The Feldman-Cousins [94] formula is used to compute the 90% C.L. sensitivity $S_{90\%}$ for events that follow a Poisonnian distribution:

$$S_{90\%}[\mathrm{cm}^{-2}\,\mathrm{s}^{-1}\,\mathrm{sr}^{-1}] = \frac{\bar{\mu}_{90}\,(n_b)}{A_{eff}\,[\mathrm{cm}^2\,\mathrm{sr}] \times T[\mathrm{s}]}\,, \tag{5.2}$$

where T is the duration spent collecting data, n_b is the number of expected background events in the 90% C.L. interval μ_{90}, $\bar{\mu}_{90}$ and A_{eff} are defined as:

$$\bar{\mu}_{90}\,(n_b) = \sum_{n_{obs}=0}^{\infty} \mu_{90} \frac{n_b^{n_{obs}}}{n_{obs}!} e^{-n_b}, \tag{5.3}$$

$$A_{eff} = \frac{n_{MM}}{\Phi_{MM}}, \tag{5.4}$$

with n_{MM} denoting the number of MMs remaining after applying the optimal cuts, $\Phi_{MM}[\mathrm{cm}^{-2}\,\mathrm{sr}^{-1}]$ representing the flux of generated MMs and n_{obs} is the total number of observed events. The Model Rejection Factor approach entails adjusting the cuts until the lowest Rejection Factor (RF) flow is determined, corresponding to the best sensitivity (see Fig.5.7). The Feldman-Cousins approach is used to derive the sensitivity at 90% C.L. after optimizing the rejection factor RF.

5.3 Results

The table 5.1 below summarizes the upper limits derived from 10 years of the analyzed data, as well as the cuts and the number of events remaining in each beta region.

β Interval	β_{reco}	β cut	α cut	N_{sh} cut	Expected background	Observed events	Flux upper limit [cm^{-2} s^{-1} sr^{-1}]
[0.5500, 0.5945[	Fitted	[0.5500, 0.5945[	< 12.4	≥ 41	5×10^{-5}	0	8.4×10^{-18}
[0.5945, 0.6390[	Fitted	[0.5945, 0.6390[	< 10.8	≥ 45	2×10^{-5}	0	1.0×10^{-17}
[0.6390, 0.6835[	Fitted	[0.6390, 0.6835[	< 8.8	≥ 51	3×10^{-4}	0	6.5×10^{-18}
[0.6835, 0.7280[	Fitted	[0.6835, 0.7280[	< 5.2	≥ 68	2×10^{-4}	0	6.7×10^{-18}
[0.7280, 0.7725[	Fitted	[0.7280, 0.7725[	< 3.6	≥ 85	5×10^{-4}	0	7.0×10^{-18}
[0.7725, 0.8170[	Fitted	[0.7725, 0.8170[	< 2.6	≥ 86	8×10^{-4}	0	3.7×10^{-18}
[0.8170, 0.8615[	1	-	< 0.6	≥ 102	0.29	0	2.8×10^{-18}
[0.8615, 0.9060[	1	-	< 0.3	≥ 105	0.18	0	1.2×10^{-18}
[0.9060, 0.9505[	1	-	< 0.3	≥ 105	0.18	0	8.8×10^{-19}
[0.9505, 0.9950]	1	-	< 0.3	≥ 105	0.18	0	7.3×10^{-19}

TABLE 5.1: The optimized cuts, the number of background events remaining after cuts, the number of observed events remaining after the cuts and the upper limit on the flux obtained in each β range, for the full analyzed data sample corresponding to 10 years live time.

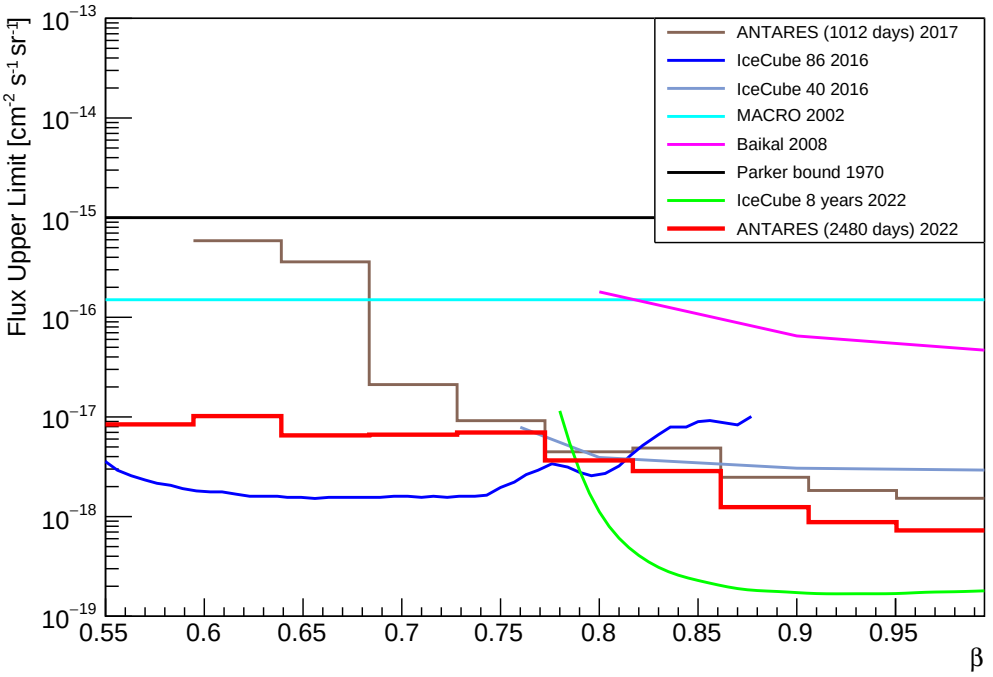

FIGURE 5.8: The 90% C.L upper limit on the flux for MMs set with the ANTARES detector and corresponding to 10 years of analyzed data (2480 days, red line) in comparison with other experiments and results including: ANTARES previous upper limit on the flux (brown line [96]), IceCube (blue [9] and green lines [97]), MACRO (cyan line [48]) and Baikal (magenta line [98]), as well as the theoretical Parker bound (black line [45]).

No event survived the selection after applying the cuts to the entire data set. Fig.5.8 shows the ANTARES upper limit on the flux for Magnetic monopoles, based over the whole 2480 days of data collection, compared to other experiments upper limits on the flux, and including upper limits from the earlier MM analysis (1012 days) performed with the ANTARES telescope as well.

In the region of high velocities, the improvement in the upper limit on the flux for MMs compared to the results obtained in the previous MMs search (ANTARES limit [96] 1012 days) is mainly due to the increase in statistics, that is data taking time. Above the Cherenkov threshold (β >0.76), where the emission of Cherenkov light is direct, the impact of the cross-section models is mitigated.

A significant improvement in sensitivity (thus the upper limit on flux) is observed, however, below the Cherenkov threshold, which is a result of the choice of the KYG model, which, as shown in Fig.3.4, can be considered more promising for lower velocities due to the improved description of the MM cross-section and the increased light yield in these regions. The added cut on β_{reco} in this region eliminated the majority of the background, therefore justifying the large decline in the number of surviving background events seen in Table 5.1 for β <0.8170. Atmospheric muons dominate the background in the $\beta \geq$0.8170 velocity range, whereas atmospheric neutrinos dominate the background in the lower velocity range.

5.4 Conclusion

The results of a new study that used an optimized simulation strategy of magnetic monopoles based on the KYG model and a wider exposure, to search for MMs with velocities ranging in $\beta \in$ [0.5500,0.9950] and crossing the ANTARES neutrino telescope, are explored in this report. To optimize the sensitivity for each of the 10 assessed intervals of β, a Model Rejection Factor technique was used, which relied on cuts on observable parameters such as the number of hits in the detector and the quality of the reconstructed events. After analyzing the whole data sample (2480 days), no event survived the selection, and upper flux limits are set for each of the 10 intervals. The choice of the KYG model for the MM cross-section with matter resulted in an improved upper limit on the flux for low velocities compared to the ANTARES' previous result, as well as the additional cut in this region that allowed for greater background rejection. The upper limits on the flux obtained in this analysis is between 7.3×10^{-19} and 1.0×10^{-17} cm^{-2} s^{-1} sr^{-1}, holding for MMs with mass M $\gtrsim 10^{11}$ GeV/c^2, in compliance with the requirement of crossing the Earth diameter [99]. This result can be considered

competitive, in particular in view of the modest size of ANTARES with respect to IceCube.

Chapter 6

Construction of the KM3NeT telescope

6.1 The KM3NeT collaboration

The KM3NeT Collaboration comprises 55 institutes and groups in 16 countries, as of October 2021 (see Fig.6.1).

Three Moroccan institutions are involved in this collaboration: Mohammed I University in **Oujda**, Mohammed V University in **Rabat**, and Cadi Ayyad University in **Marrakech**.

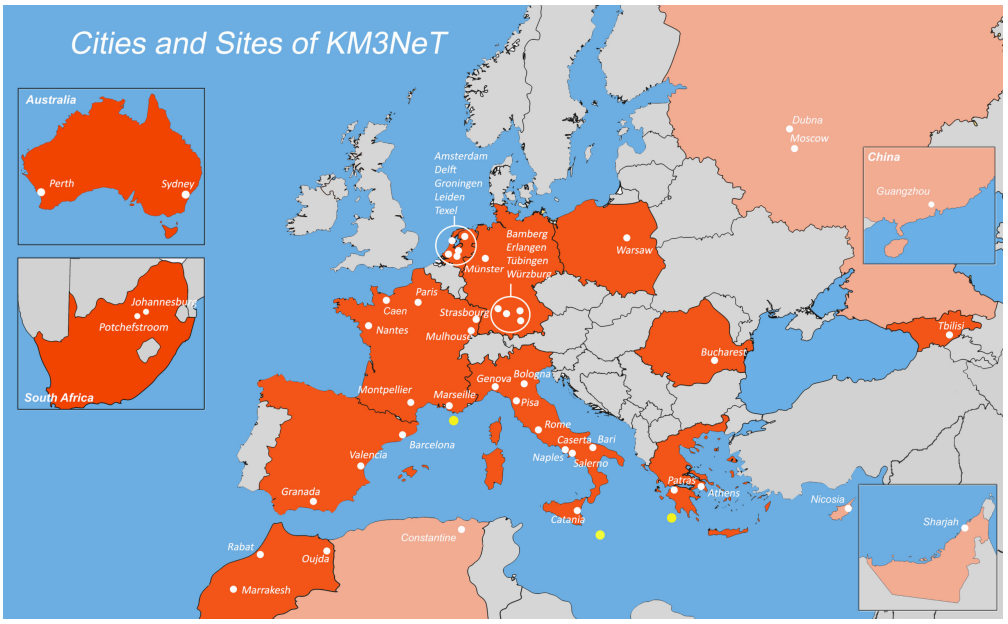

FIGURE 6.1: The map of the KM3NeT collaboration's member cities and sites.

Currently, two Moroccan institutes (Mohammed V University in **Rabat** starting in 2021 and Mohammed I University in **Oujda** starting in 2022) are actively taking part in the construction of the KM3NeT telescope (via DOM integration and BM integration respectively).

The DOM integration and BM integration processes carried out in the Rabat and Oujda sites will be detailed in the up-coming sections.

6.2 General overview of the KM3NeT telescope

The KM3NeT (Kilometre Cube Neutrino Telescope) is a network of light-sensitive detectors in the Mediterranean Sea that is currently under construction. The aim of the detectors is to identify neutrino interactions at energies ranging from MeV to multi-PeV, covering a wide range of scientific applications. Further information can be found in [100] in which detailed description of the KM3NeT design and physics goals are covered.

Two detector blocks make up KM3NeT:

ORCA, a dense network of digital optical modules (DOMs) installed 40 kilometers off the coast of Toulon (France). Its main purpose is the establishment of neutrino mass hierarchy by measuring atmospheric neutrino oscillations, targeted at the GeV scale.

ARCA, situated 80 kilometers from Portopalo di Capo Passero (Italy), aims to detect cosmic neutrino sources in the TeV to PeV range.

Fig.6.2 below shows the actual map of both blocks.

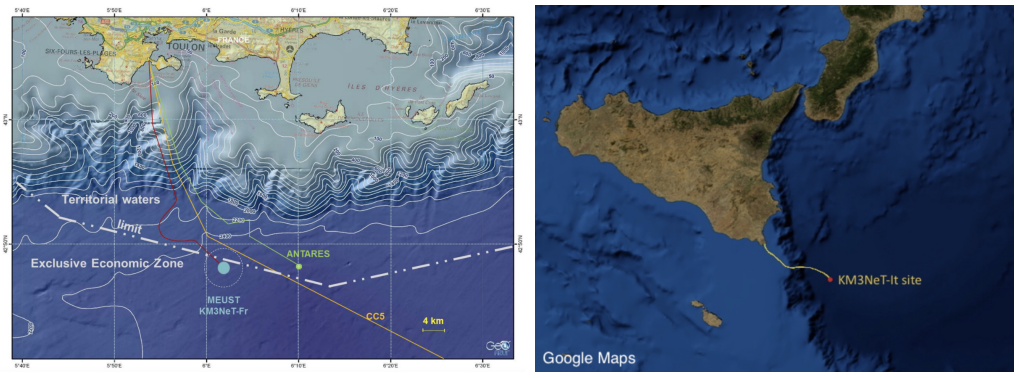

FIGURE 6.2: Map of the Mediterranean Sea south of Toulon, France. The location of the KM3NeT-France (ORCA) and ANTARES installations are indicated on the left. On right, close to Sicily, Italy is the location of the KM3NeT-Italy installation (ARCA).

KM3NeT covers a diverse range of possibilities in addition to its primary physics aims. The hunt for exotic particles and dark matter candidates, sterile neutrinos, CP-violation among others, even extending to oceanographic, geophysical and biological researches,

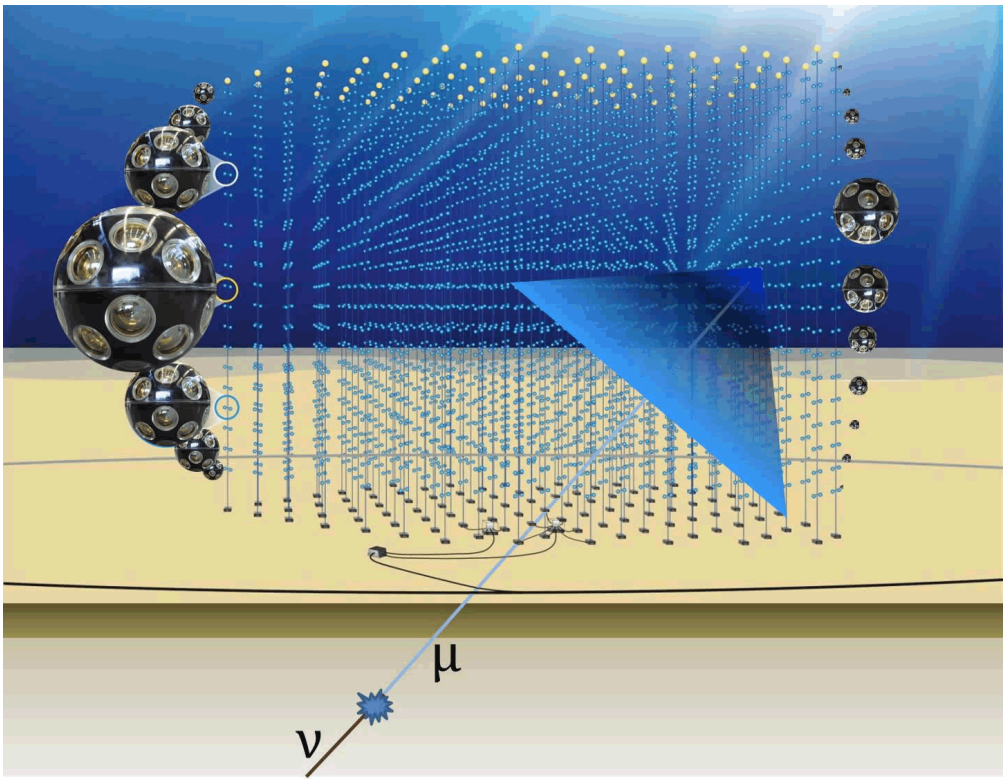

FIGURE 6.3: Illustration of the detection principle of the KM3NeT telescope showing the trajectory of a muon in blue after the interaction of the neutrino in black with matter below the sea bed. The image shows The cone of Cherenkov light emitted along the path of the muon as well.

are all complementary topics of research for the telescope. Having a low energy threshold makes it sensitive to low-energy astrophysical neutrinos (on the GeV scale) (e.g. solar flares). ARCA can detect neutrino traces of dark matter particle annihilation or decay in the Sun and Galactic structures at high energies.

Other research can focus on signals of exotic physics such as magnetic monopoles, allowing for a continuity and a possibility of improved results in comparison to those discussed in the previous chapter using the ANTARES telescope.

The KM3NeT detectors will use up to 200000 photo-multipliers tubes (PMTs) integrated in around 6000 DOMs in total, resulting in an instrumented volume at the kilometer cube scale. The orientation and timing information provided by Cherenkov photons will be employed by recording the hit timings with nanosecond precision, owing to the large absorption length and low scattering probability of light in water.

A detection unit (DU) is made up of eighteen DOMs that are vertically organized and moored to the sea bottom. The DU's vertical position is maintained by a buoy attached at the top. A special cable called the *vertical electro-optical cable* (VEOC) runs down the DU and is linked to each DOM through a pressure-resistant penetrator illustrated

in Fig.6.20. The VEOC is an oil-filled plastic tube that incorporates an optical fibre for data transmission and two copper wires for power distribution for each DOM. A building block consists of 115 detection units placed in a quasi-cylindrical array. The DOM architecture of ARCA and ORCA are similar, but the instrumentation density and total size of the detector array varies. The mean horizontal distance between the placements of the DUs and the average vertical distance between the DOMs in a detection unit are optimized for the distinct energy scales of relevance in the two detectors. Table 6.1 summarizes the ARCA and ORCA detector geometries.

	ARCA	ORCA
Building blocks	2	1
DUs	230	115
DOMs	4140	2070
PMTs	128340	64170
Vertical distance between DOMs	36 m	9m
Horizontal distance between DUs	90 m	20 m

TABLE 6.1: The geometrical parameters and composition of the KM3NeT ARCA and ORCA detectors.

Both of the KM3NeT detector are connected to shore via one or more *main electro-optical cables* (MEOC), which consist of a power conductor and optical fibres. The MEOC ends at a cable termination frame (CTF), which is linked to the secondary junction boxes. The KM3NeT-It (ARCA) sea floor arrangement is shown in Fig.6.4. The ARCA MEOC transmits power at 10 kV DC, which is converted at the CTF to 375 V DC. Fig.6.5 depicts the KM3NeT-Fr (ORCA) seabed architecture. It makes use of two MEOCs, one of which will be reused from ANTARES. Each MEOC is linked directly to a junction box, from which it is branched out to the next MEOC in the chain. The ORCA MEOC provides a single 3.5 kV AC conductor to the detector.

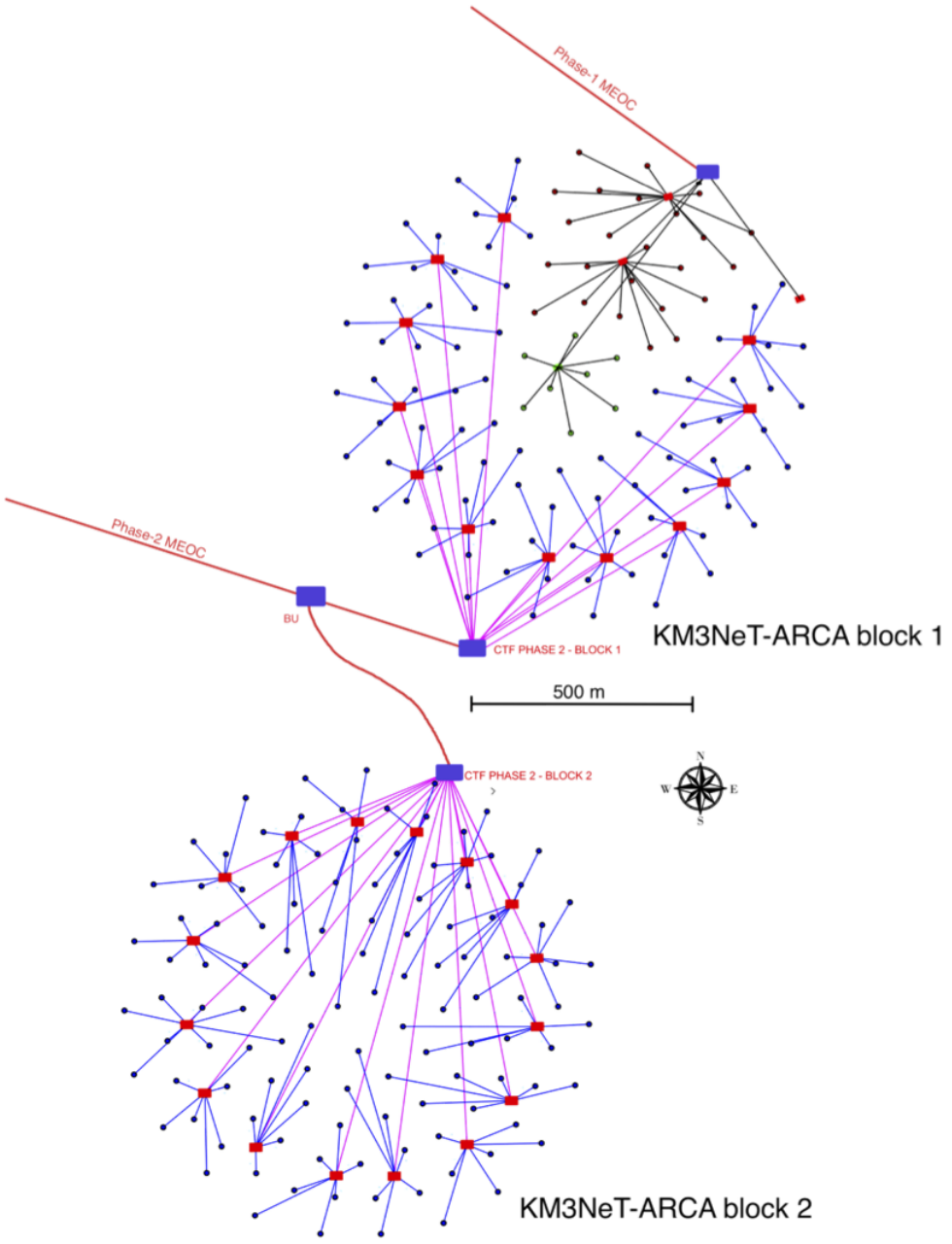

FIGURE 6.4: Layout of the two blocks of the KM3NeT ARCA detector on the sea bed, taken from: [100].

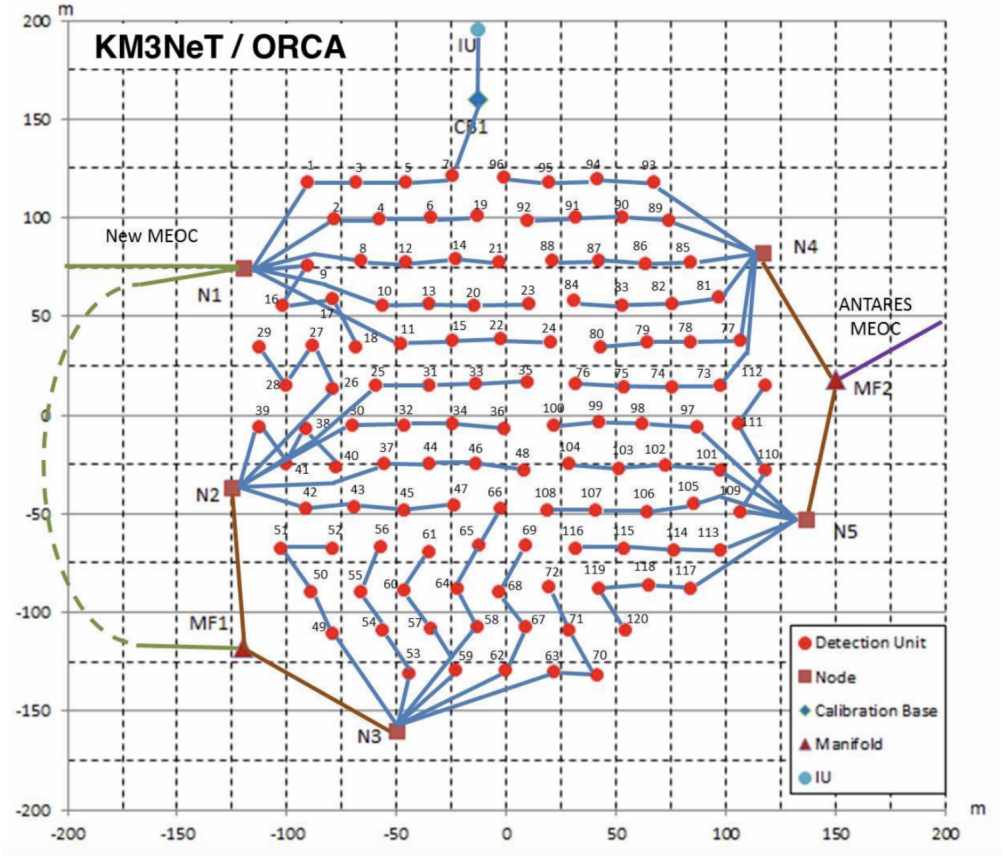

FIGURE 6.5: Layout of the KM3NeT ORCA detector on the sea bed, taken from: [100].

6.3 DOM integration in the Rabat site

The Digital Optical Module (DOM), a pressure-resistant glass sphere containing thirty-one 80 mm PMTs with three-dimensional coverage, is the basis for the KM3NeT design. Fig.6.6 below shows an image of the first DOM integrated in the Rabat DOM integration site. The paper [101] describes in details the KM3NeT DOM.

6.3.1 Production distribution

In order to reach the goal of producing more than 6200 DOMs, a distributed production approach has been set in place. To meet the KM3NeT's baseline production rate, the integration procedure has been standardised for all the integration sites. The requirements of the KM3NeT collaboration to carry out the production of DOMs include providing a moderately sized laboratory area, a dark box (and/or dark room), reasonably priced equipment, and a small number of human resources. There are now eight optical module production sites (see Fig.6.7) with a combined capacity to assemble around 100 optical modules per month.

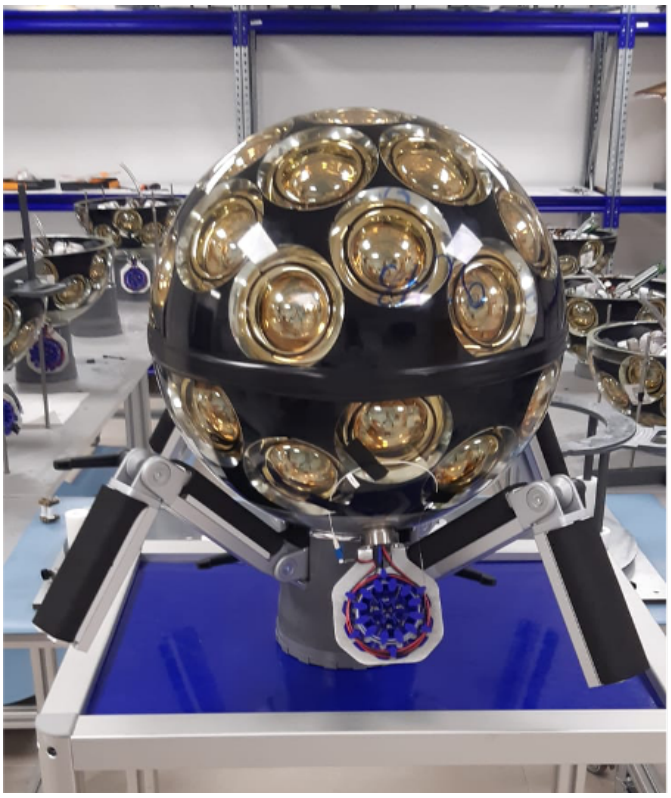

FIGURE 6.6: The first DOM integrated in the Rabat DOM integration site.

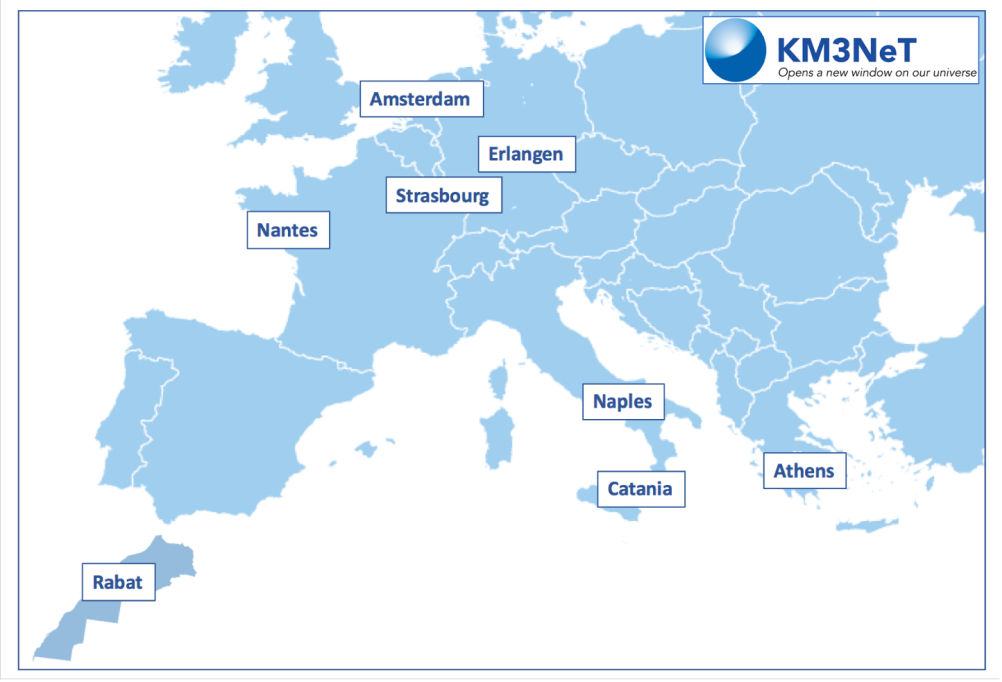

FIGURE 6.7: The eight DOM integration sites of KM3NeT.

FIGURE 6.8: The first set of 7 DOMs integrated in the Rabat DOM integration site, inserted in the transportation crate and ready to be sent to a DU integration site.

The Rabat DOM integration site, being the latest structure to join the DOM integration group, has successfully integrated the first set of 7 DOMs (see Fig.6.8). A second set of 18 DOMs is programmed to be assembled starting later on the year 2022.

6.3.2 Site requirements and preparation

In order to carry out DOM integration activities, the KM3NeT collaboration established a set of rules and requirements applied to all concerned sites. A laboratory in the faculty of Science of Rabat has been made available to host the DOM integration activities, and had been renovated to meet the KM3NeT collaboration's requirements (see Fig.6.9).

6.3.2.1 Space requirements

There are three different placements that are required:

FIGURE 6.9: The Rabat DOM integration site before and after the renovation according the KM3NeT collaboration's requirements.

- a storage area for the components, enough for at least 18 DOMs, corresponding to one DU.
- a storage area for the integrated hemispheres and the closed DOMs, the storage period of closed DOMs is independent of the DOM integration group, and several criteria must be taken into account.
- an area for various integration activity (the site itself):

  - A core assembly workbench,
  - A DOM test (dark box) workbench,
  - A gel pouring workbench,
  - A helium leak test workbench,
  - A DOM closure workbench,
  - 5 DOMs workbenches with 2 positions each,
  - Shelves for 36 halves with enough space between adjacent halves.

6.3.2.2 Environmental conditions

Light

The dark current of the PMTs increases when they are exposed to UV light, as does the time it takes to restore an acceptable noise level. As a result, direct daylight or fluorescent tubes are to be avoided. As seen in Fig.6.9, the windows allowing for day light the reach the laboratory have been covered in the renovation. LED tubes should be used to illuminate the laboratory. The color temperature of the LED has no bearing on the PMT noise. The PMTs should be kept in the dark as much as possible, especially during storage.

Other radiations: magnetic field, mobile phones, ionizing radiations

The functional testing of the top and bottom spheres, as well as the DOM calibration and acceptance tests, should all be conducted in a magnetic-free environment. Mobile phones should also be avoided near a test bench during any tests. Ionization radiations should be avoided at all costs: PMTs should not be subjected to charged particles.

Cleanliness

- Dust exposure must be prevented to avoid an electrical short circuit.

- The surfaces of the PMTs and glass hemispheres are to be cleaned during the integration process, immediately before the components are assembled.

- Open DOMs should be coated with anti-electrostatic material, such as pink bubble wrap, to avoid Electrostatic Discharge (ESD). This also provides protection from dust.

As a result, the standard degree of laboratory cleanliness is sufficient.

- It is critical to place a metallic mesh on the floor around the gel pouring workstation as seen in Fig.6.9.

Any alternative method of maintaining cleanliness, such as an adhesive mat at the laboratory's entrance, is encouraged.

Temperature, humidity and water source

The temperature should be between 15 and 25 degrees Celsius. Furthermore, the humidity level should be between 40% and 60% to prevent ESD. As a result, monitoring equipment are required.

The laboratory has been equipped with 2 air conditioners, 1 dehumidifier and a monitoring tool of temperature an humidity. (See Appendix A).

Any water faucet in the integration site must be away from the electronics storage area.

6.3.2.3 Man power and safety

The human resources needed to carry out DOM integration activities are:

- One integration site responsible,

- Two technicians (one primary and one for back up to assist in operations that require two people),

- One local quality supervisor.

Local safety precautions are usually in accordance with EU safety criteria and are thus deemed adequate.

6.3.3 DOM Components

The multi-PMT digital optical module was designed as a standard 0.44 m diameter pressure-resistant glass sphere with a dense packing of photo-detection sensors, position and timing calibration devices, and associated electronics for electrical power, read-out and data acquisition, monitoring, and long-range communication with the onshore control station. The DOM's components were chosen for their ability to operate in low-power environments. As a consequence, DOM's electrical power consumption could be kept to 7 W [100].

This section is dedicated to describe the DOM's components, an overview can be seen in Fig.6.10 and Fig.6.11.

The numbers showing in Fig.6.11 refer to:

1. Bottom support structure
2. Top support structure
3. Glass hemisphere (bottom)
4. Bottom support structure with PMTs and light collection rings installed
5. Tray for routing of optical fibres
6. Cooling and support mechanics (cooling mushroom)
7. Power board
8. Central Logic Board
9. PMTs with base attached and light collection rings
10. Pressure gauge
11. Signal collection boards (Octopus board small and large)
12. Nano beacon (led flasher)
13. Penetrator
14. Piezo accostic sensor
15. Laser transceiver (SFP).

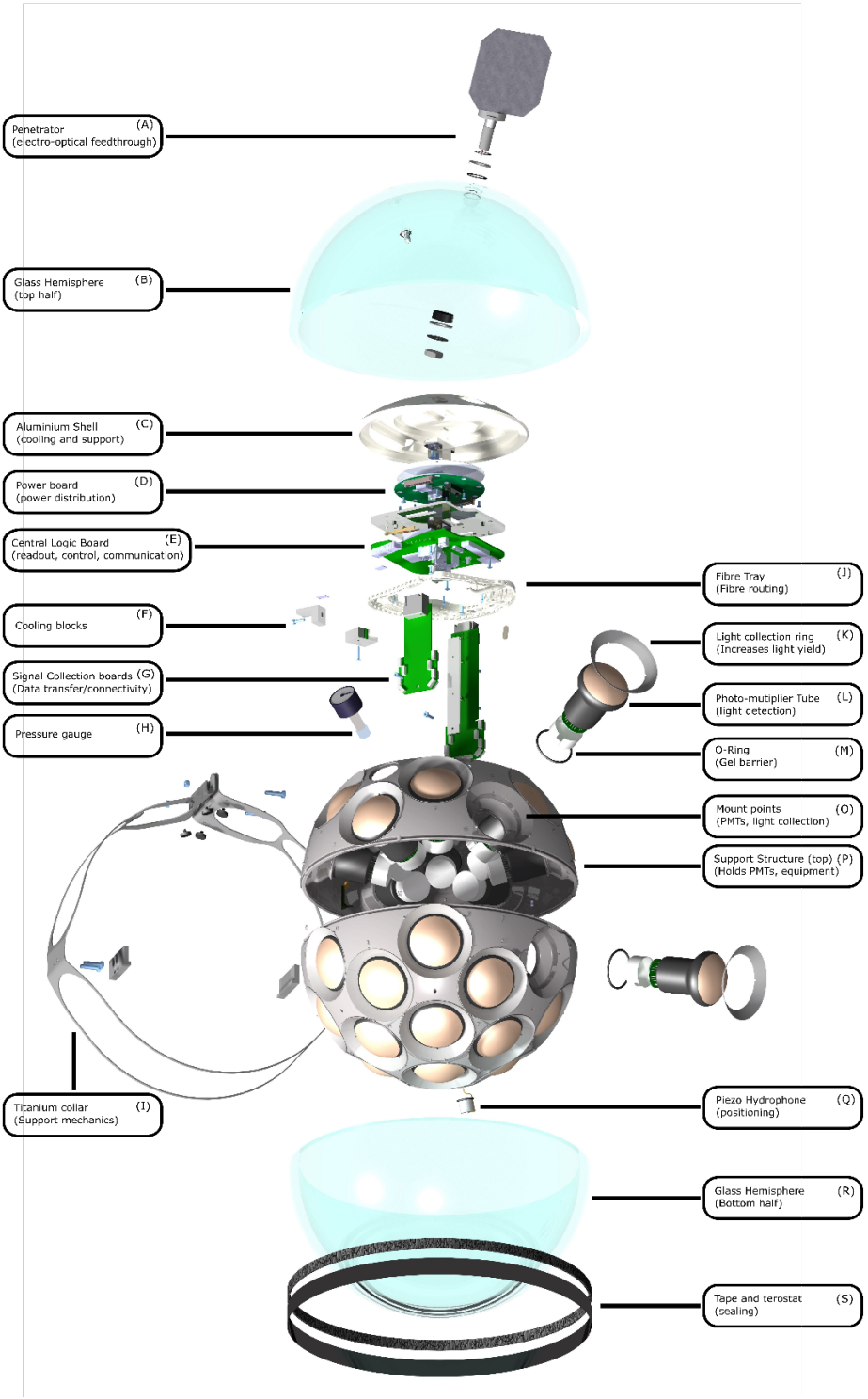

FIGURE 6.10: The KM3NeT DOM in exploded view, with the a label of each component, taken from [100].

FIGURE 6.11: The KM3NeT DOM's components numbered: taken from [101].

6.3.3.1 The photomultiplier tube (PMT) and its base

Hamamatsu provided the R12199-02 3 inch for the first batches, which is illustrated in Fig.6.12 with the base. For the succeeding batches, the Hamamatsu R14374 was used, which has somewhat enhanced performance, particularly in terms of transit time spread. A convex bialkali photo-cathode with an 80 mm diameter and a 10-stage dynode structure are used in the PMTs. For the case of the 7 DOMs integrated in Rabat, 2 DOMs had the R12199-02 while the remaining 5 had the R14374 one, 7 boxes of 30 PMTs each and 1 box of 7 PMTs were received as seen in Fig.6.13. The comparison between the two model alongside other PMT related information are found in [102]. Polished metal rings (component L in Fig.6.10) are positioned at a 45-degree angle around the top of PMTs during optical module integration, producing a 92 percent reflectance for photons in the wavelength range 375-500 nm. The recessed location of the rings takes use of the convex form of the PMT's sensitive region. The photon acceptance is boosted by 20-40% as a result of this, with the majority of the gain occurring in the forward direction [102]. The photo-cathode of the PMTs is powered with a negative high voltage (HV), which allows for easier control and signal digitization. To avoid ESD between the PMT and its surroundings, an insulating coating is placed to the exterior of the photomultiplier tubes and on the PMT bases [103]. Given the high-counting rate characteristic of the deep-sea condition, a relatively low nominal gain of $3 \cdot 10^6$ is selected to minimize the effect of the degradation and hence maximize the lifespan of the PMTs. The operational gain is acquired by fine-tuning the HV of each PMT in the lab and while the DOM is in operation. The tuning is done by considering the distribution of pulse-widths of each PMT and setting the average to a value corresponding to the required gain, as the information on the PMT pulse is reduced to the time of crossing a threshold together with the pulse duration (the time-over-threshold technique).

The PMTs have custom-designed low-power HV bases with integrated amplification and tunable discrimination. Small form-factor connectors (SAMTEC 0.80 mm Tiger Eye Micro Terminal Strip) and flat kapton cables are integrated into the printed circuit board (PCB) and carry the 3.3 V power voltage to the base, as well as an Inter-Integrated Circuit (I2C) communication bus and a 100Ω LVDS (Low-Voltage-Differential-Signal) output. A Cockroft-Walton (CW) circuit generates high voltage directly on the base, which is controlled by CoCo [104], a custom-designed Application-Specific Integrated Circuit (ASIC). Using feedback from the HV circuit, the ASIC adjusts the frequency at which electricity from the 3.3 V supply is pulsed inductively in the CW circuit. The analog PMT pulse is amplified by a charge amplifier before being digitized by PROMiS (PMT Read Out Mixed Signal), a custom-designed mixed signal ASIC [105].

FIGURE 6.12: A Hamamatsu R12199-02 photomultiplier tube with base attached in the left. A photomultiplier base on the right, taken from [100].

FIGURE 6.13: One of the boxes of PMTs received in the Rabat site, it is advisable to wear anti-ESD gloves while handling the PMTs.

A comparator distinguishes the amplified PMT signal against an adjustable threshold during the digitization process.

6.3.3.2 Electronics

The DOM contains the following electronic boards:

the Central Logic Board (see Fig.6.14),

Two PMT-signal collection boards ('long/short octopus', components 11 in Fig.6.11),

The power board (component 7 in Fig.6.11).

The SFP transceiver (component 15 in ig.6.11).

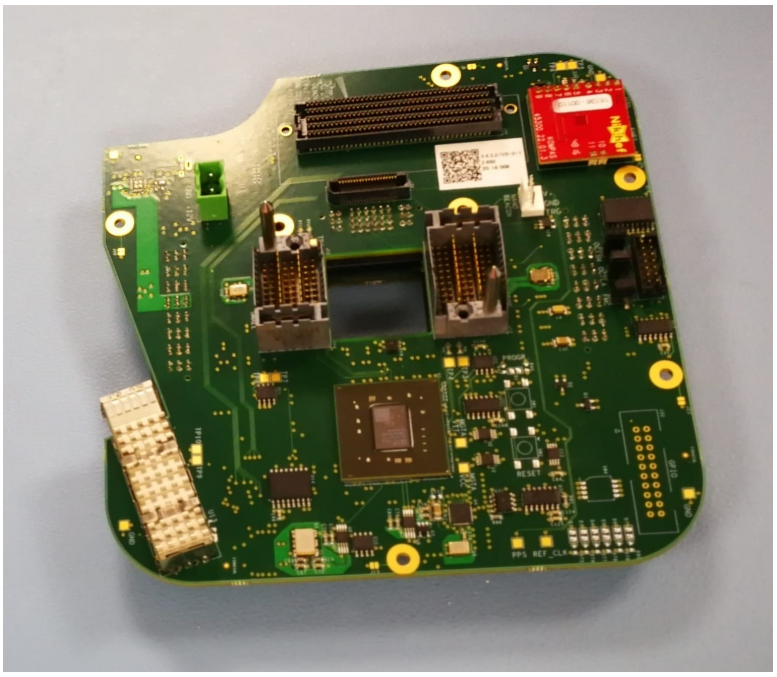

FIGURE 6.14: One of the 7 central logic boards received in the Rabat site.

The central logical board: CLB

The Central Logic Board (CLB) (shown in Fig.6.14), which controls all electronic equipment inside the DOM, interprets data from PMTs and the acoustic piezo sensor, and maintains connection with the onshore control station, is at the core of the DOM electronics. In addition, the CLB monitors the DOM's working state by reading a humidity sensor, various distributed temperature sensors, and the compass/tilt-meter. The CLB's Field Programmable Gate Array (FPGA) Xilinx Kintex 7 is configured from an image saved on the CLB's re-programmable Serial Peripheral Interface (SPI) memory, which stores several pictures, when the optical module is powered on. Two images are saved in the typical configuration, the first of which is 'called "golden" image, which is loaded during power-up. The image runs through a series of tests, including communication checks, and gives a time window for intervention before prompting the FPGA to be reconfigured with a run-time' image that enables complete system functioning. In situ, both images can be re-flashed or changed. Safeguards have been included to enable for data corruption recovery during the golden or run-time upload of a fresh image.

The octopus boards

Two 'octopus' boards serve as the interface between the CLB and the PMT bases, each servicing the PMTs in a one of the DOM's hemispheres. The 'octopus' boards provide an I2C multiplexer and deliver 3.3 V to the PMT bases, allowing each PMT base to

FIGURE 6.15: DOM's lower hemisphere with PMTs connected to the large octopus board.

be addressed separately from the CLB while sending one LVDS transmission line from each PMT to the CLB. The long octopus board, which serves the DOM's bottom half, is also connected to the piezo sensor's cable 6.15, which carries the requisite 5 V and digital communication between the sensor and the CLB.

The power board

The power board (see Fig.6.16), installed within the DOM's top hemisphere, supplies fixed voltage rails of 1, 1.8, 2.5, 3.3, and 5 V, as well as a rail that is configurable up to 30 V via a Digital-to-Analog converter, to fulfill the demands of the various subsystems. The voltage and current of all rails are monitored by Analog-to-Digital converters (ADCs), with output signals being sent to the CLB.

The SFP transceiver

The Small Form-factor Pluggable (SFP) transceiver (see Fig.6.17) is needed for optical communication and time synchronisation. It contains a high-power duplex single mode laser transceiver (>80 km range) for communications with the onshore control station

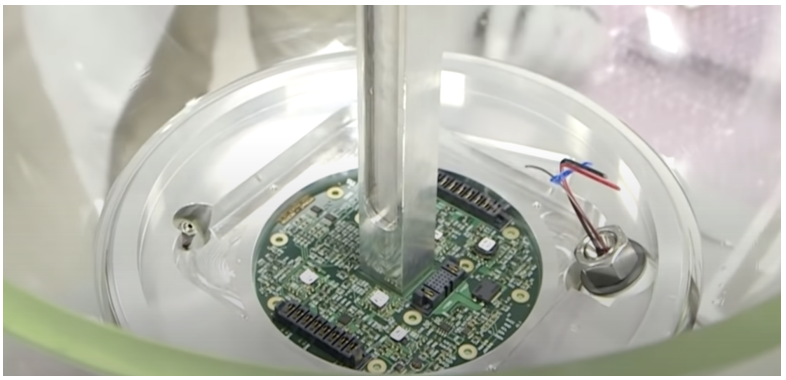

FIGURE 6.16: Power board ready to be installed in a DOM's top hemisphere.

through the fiber network. Communication to the optical modules is currently accomplished via a broadcast from the control station on a shared wavelength. Each optical module has an emitting wavelength selected from the ITU^3 grid with 50 GHz spacing to allow multiplexing of the data stream from the transceiver onto a smaller number of optical fibres. The underwater network is designed to offer a maximum of 72 different wavelengths, allowing four detecting units with 18 optical modules each to be connected to a single cable. The DOM includes an optical add-and-drop filter, shown in the picture 6.18, that combines the two communication channels to and from the SFP transceiver into a single fibre.

FIGURE 6.17: One of the seven SFP transceivers received in the Rabat site.

FIGURE 6.18: Add-and-Drop filter, combines the signal coming from 2 optical fibers into one.

6.3.3.3 Support and cooling components

Glass hemispheres

The DOM components are enclosed in a Vitrovex® low-activity boro-silicate glass sphere with a diameter of 0.44 m (see Fig.6.19). The spheres have a 14 mm thickness and can sustain pressures of up to 6.7×10^7 Pa. The sphere's glass satisfies a light transmission criterion of more than 95 percent above 350 nm, matching the PMTs' maximum sensitivity optical wavelength range.

FIGURE 6.19: Some of the glass hemispheres received in the Rabat site.

The application of the clear two-component silicone gel (Wacker SilGel® A/B) ensures optical contact between the PMTs and the glass. The two hemispheres forming the glass sphere are in a glass-on-glass contact at the equator, relying on atmospheric pressure to maintain the sealing airtight. In the sealed DOM, an under-pressure of 2×10^4 Pa is applied inside the DOM, allowing for an air-tight sealing. This number strikes a compromise between shipping, storage, and deployment limitations, during which the DOM must remain closed, and the appropriate functioning of all internal components and the gel. A layer of Terostat 81 coated in Scotch encircles the mid section of the DOM (see Fig.6.6) to reinforce the sealing.

The top glass hemisphere has 2 holes, one contains a valve from which air will be extracted to apply the under-pressure to close the DOM. The other hole is used to install the penetrator (Fig.6.20) that will allow for the communication with the DOM via one optical fiber, as well as the power supply to the DOM via two copper wires. The

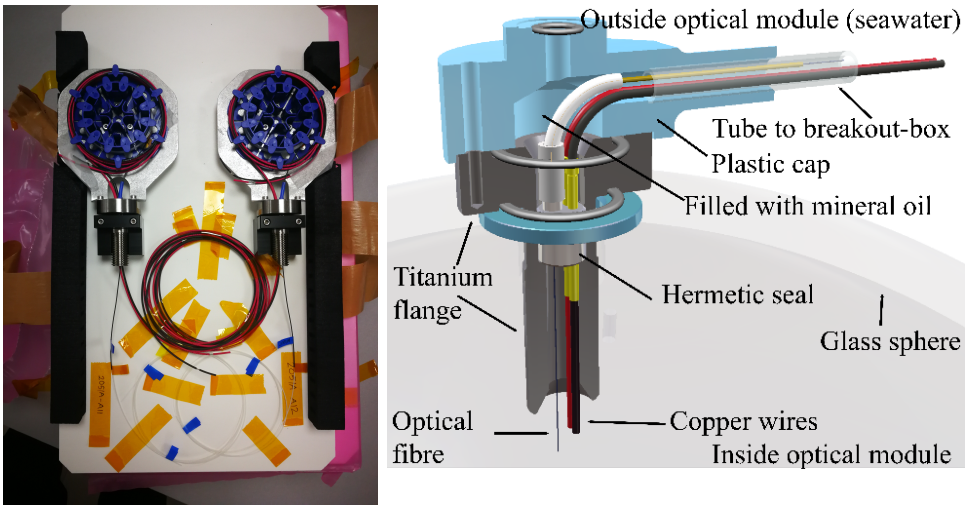

FIGURE 6.20: Left: 2 of the 7 penetrators received in the Rabat site. Right: Open schematic of a KM3NeT penetrator, taken from: [101].

penetrator must be waterproof, and has to be tested by a helium leak testing machine which will described later.

PMT support structure

Two different plastic support structures is purposed to install the PMTs, one for each hemisphere. The top support structure holds 12 PMTs, 1 nano beacon (components 12 in Fig.6.11), and a pressure gauge to monitor the under-pressure inside the DOM (components 10 in Fig.6.11), while the bottom one hold 19 PMTs and has a spacing for the piezo acoustic sensor to pass through (components 14 in Fig.6.11).

The structures used to be created utilizing 3D printing, the printed support structures' form include optimizations for printing numerous pieces at once in the printers' restricted volume. For the top structure, 3D printing was substituted with an injection moulded design made of acrylonitrile butadiene styrene (ABS) for a speedier and much lower cost of manufacture. The support structures are either made in or painted black to mitigate light reflection.

A PMTs bottom support structure is shown in the picture of Fig.6.21 while being inserted with PMTs and reflector rings.

Cooling parts

The top hemisphere of the DOM contains, alongside the electronics, a number of aluminum cooling blocks, that act as an internal cooling system for the electronics that tend

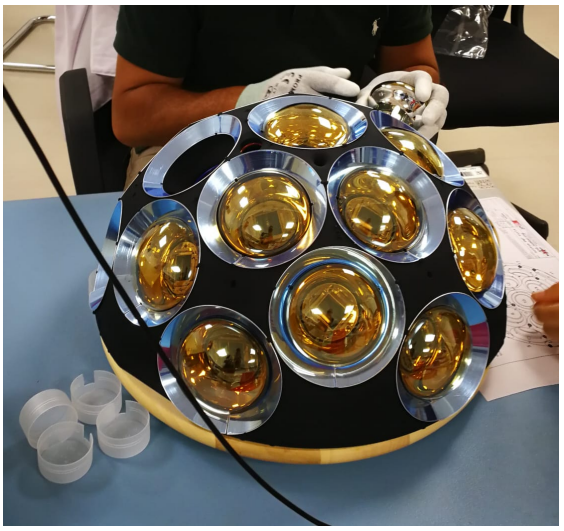

FIGURE 6.21: Bottom PMT support structure being integrated with PMTs and reflector rings.

to have and increase in temperature while powered. The cooling mushroom (component 6 in Fig.6.11 is glued to the glass hemisphere using a special primer and gel, and all other aluminum block are in contact with it, it serves to dissipate the heat from inside the DOM outward.

6.3.4 DOM integration procedures

The DOM integration procedures are divided among four branches, that are merged 2 by 2, to result in a fully functional instrumented sphere, the assembly of these four branches is detailed in what follows.

6.3.4.1 Reception of components

Once the components are received in the Rabat DOM integration site, a mandatory visual inspection is performed, then all the UPIs (Unique Product Identifier) of the components are cross checked with the one in the KM3NeT data base. If everything checks out, the local quality supervisor (LQS) then proceeds to close the open SRS (Shipping Record Sheet), and the DOM integration procedures can start. Otherwise, if there are any damaged component or any discrepancy in the UPIs, a NCR (NON Conformity Report), is to be opened by the LQS, and wait for a suggestions on behalf of the DOM integration group experts for a corrective action.

6.3.4.2 The DOM Integration Assistant (DIA)

This DIA is a powerful tool used to insure the traceability of the DOM integration activities for all the involved sites. Once the SRS is closed, all the components' UPIs become avaible in the integration site's DIA. It is mandatory to fill in the UPI of each component (if applicable) in the DIA once integrated in a DOM. The results of all the tests performed on the DOMS are filled in the DIA as well. The interface of the DIA can be seen in the Fig.6.22.

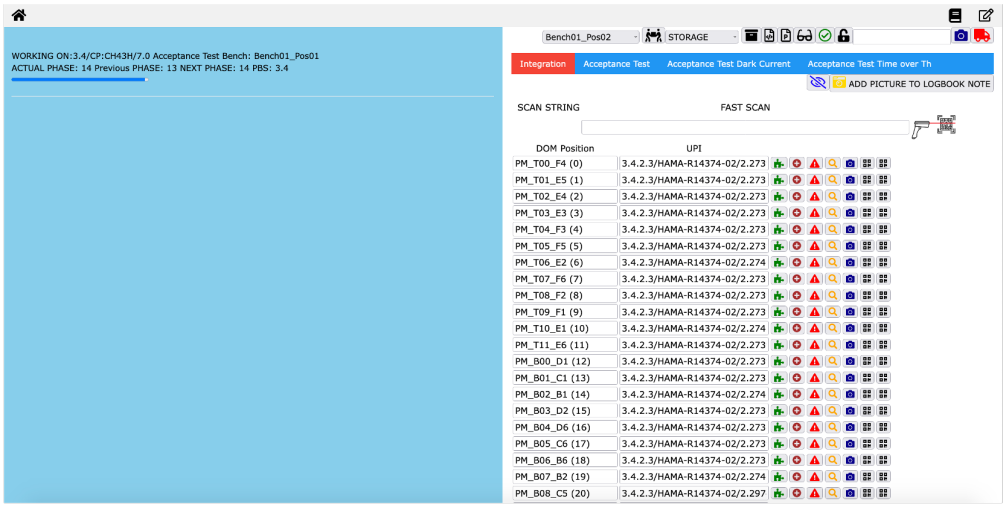

FIGURE 6.22: The interface of the DOM Integration Assistant.

6.3.4.3 Integration procedures of the top glass hemisphere

Gluing of the cooling mushroom on the top glass hemisphere

A special primer is applied on the cooling mushroom and the inside of the glass hemisphere (top), an alignment tool is used to properly position the mushroom (see Fig.6.23), and the glass hemisphere is placed on a cylindrical support to determine where to apply the primer on the inside of the hemisphere. After applying the primer, it is left to rest and the process for the preparation of 200g of optical gel is started. 120g of Gel type A and 80g of type B (a ratio of 60% to 40%), are mixed for 5 to 10 minutes, and degassed using the desiccator and the under pressure pump (0.6 bar). The bubbles are seen elevating and disappearing. Once degassed, the gel is injected in the gap between the mushroom and the glass hemisphere via a syringe.

In the case of the 7 DOMs integrated in Rabat, the hemispheres were received with mushrooms already glued, however the next set of 18 DOMs expected to arrive soon, this operation with be done in the Rabat DOM integration site.

FIGURE 6.23: Cooling mushroom alignment tool, picture taken during the training in Athens DOM integration site.

Installation of the electronics

On the top hemisphere where the cooling mushroom is glued, the installation of the electronic components is carried out:

- The cooling bar is mounted using 2 countersunk M5 x 12 screws, with a torque of 3 Nm.
- The cooling pad that was prepared before is sticked to the cooling mushroom.
- The power board is installed next, J4 connector facing the penetrator hole, and using 11 M3x8 screws with a torque of 0.6 Nm.
- The Faraday plate is mounted next, above it 5 aluminum spacers and 2 nylon spacers are set.
- The compass on the CLB is checked for calibration in the Data-Base.
- The spring holder is mounted on the CLB after cutting some excess off of it.
- The CLB is installed next, using 3 M3x16 screws and 4 M3x12 screws, all with a torque of 0.6 Nm.
- The cooling pad for the FPGA is sticked on it, and the aluminum block was mounted on top of it.

- The SFP is mounted next, after checking that its channel matches that of the CLB's, a spacer pad is put over it, and another aluminum block is mounted over it.

In the case of the first set of DOMs sent to Rabat, 2 hemispheres were received with electronics already installed (see Fig.6.25, while the remaining 5 had their electronics integrated in the Rabat site. The cooling components integrated alongside the electronics (Faraday plate, cooling bar and 2 cooling blocks) are shown in the picture in Fig.6.24.

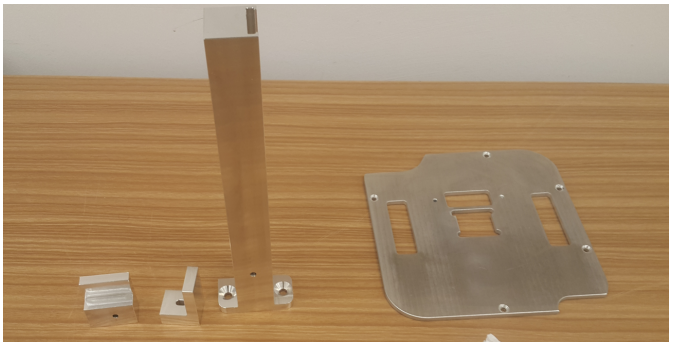

FIGURE 6.24: Cooling parts integrated alongside the electronics, from right to left: Faraday plate, horizontal bar, 2 cooling blocks. These aluminum parts are all in contact with the cooling mushroom. The picture was taken during the training in the Athens DOM integration site.

FIGURE 6.25: Top Glass hemisphere after the integration of the cooling mushroom and the electronics.

Installation of the penetrator and helium leak test

The parts used to mount the penetrator (Fig.6.20) are arranged in advance, while minding the ones that go inside the glass hemisphere and the ones that go on the outside, the order is described in a document provided by the KM3Net collaboration. The picture

below (Fig.6.27) shows the tools used for the installation of the penetrator as well as the needed parts to insure the air tightness (bolts, and o-rings). The penetrator is tightened with a torque of 10 Nm.

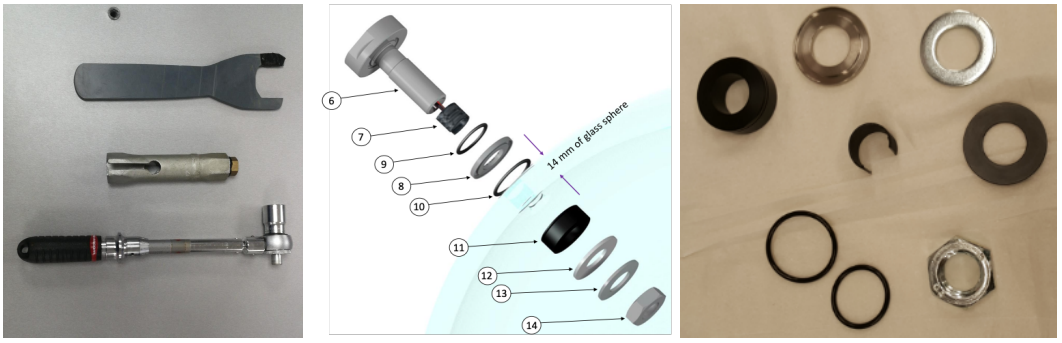

FIGURE 6.26: The tools used to mount the penetrator in the left, and parts used to prevent any leak on the right. The middle picture shows the order of which the parts are to be installed.

Once the penetrator is mounted, it is mandatory to verify that it is leak free, to do so, a special helium leak test machine (Pfeiffer ASM 340) is used for this task.

As seen in 6.26, a tube is mounted between the vacuum cap (white cylinder) and the machine, then the cap is put over the penetrator covering it entirely, not placing the penetrator exactly on the middle, but moving further from the base of the glass hemisphere (weakest point of the glass hemisphere). A circular rubber is put between the cap and glass hemisphere for air tightness. The vacuum pump then is turned on, once the under pressure reaches the order of $10^{-10} mbarl/s$ the screen of the machine turns green instead of red. Once the acceptable value is reached, the helium is then sprayed on the inside of the hemisphere and the green screen is monitored. If the screen remains in green and the value does not increase, the test is considered OK. Otherwise, in case the penetrator is leaking, the value will increase and the screen turns back in red. The same operation is then repeated for the vacuum valve.

For all the penetrators and vacuum valves tested in the Rabat site, the helium leak test was OK.

Optical fiber splicing and connection of the CLB to the penetrator

This procedure is crucial to establish communication with the DOM from the outside, as well connecting it to the power source. the steps of this operation are as follows:

- The optical fiber tray with the add-and-drop filter routed in it previously is mounted on the CLB, by removing 3 temporary screws from the CLB and re-mounting them over the tray.

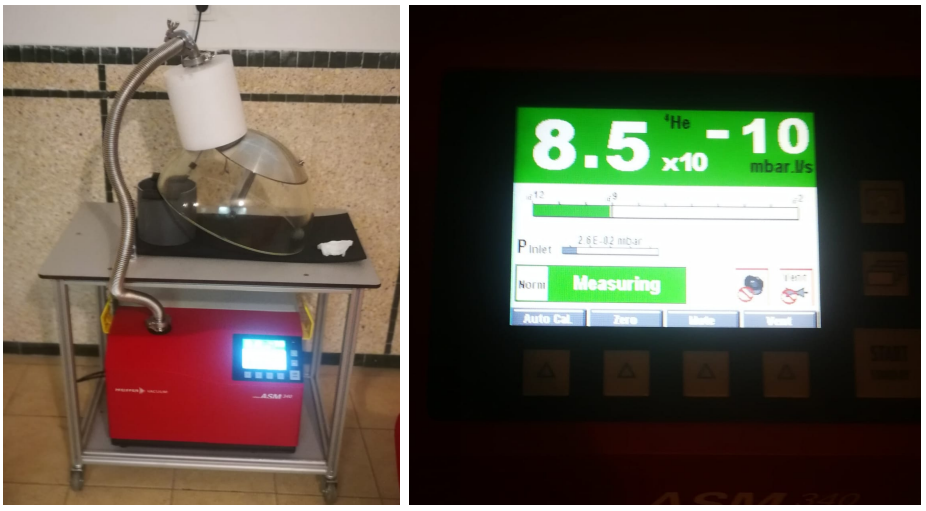

FIGURE 6.27: The setup of the helium leak test in the left, and screen of the helium leak test machine once the acceptable value of under pressure is reached on the right.

- The Reflect and the Pass ports of the add-and-drop filter are plugged to the SFP after cleaning, (the Pass close to the glass, the Reflect close to the tray (see Fig.6.18).
- The Com is connected to the power meter machine to check if the signal is active, as long as it gives a positive value it is OK, meaning the CLB is emitting signal thus functioning well (see left picture in Fig.6.28) .
- The orange and black wires coming from the penetrator to the inside of the hemisphere were cut at 8cm then plugged in the CLB.
- The CLB is then powered on with a source of 12 V DC.
- The protective tube is removed from the penetrator's optical fiber, this task requires two persons.
- The Com fiber is cut on a mark placed on the tray, to be spliced with the fiber coming from the penetrator (see right picture in Fig.6.28).
- The LC connector that was cut from the Com fiber in spliced again on the outside of the Dom with the penetrator's out side optical fiber.
- The LC connector coming from the newly spliced optical fiber is connected to the power meter machine, to measure the loss after the splice. The test is OK when the difference does not exceed 0.2dBm.

All the 14 splices performed in the Rabat site for all the 7 DOM were OK.

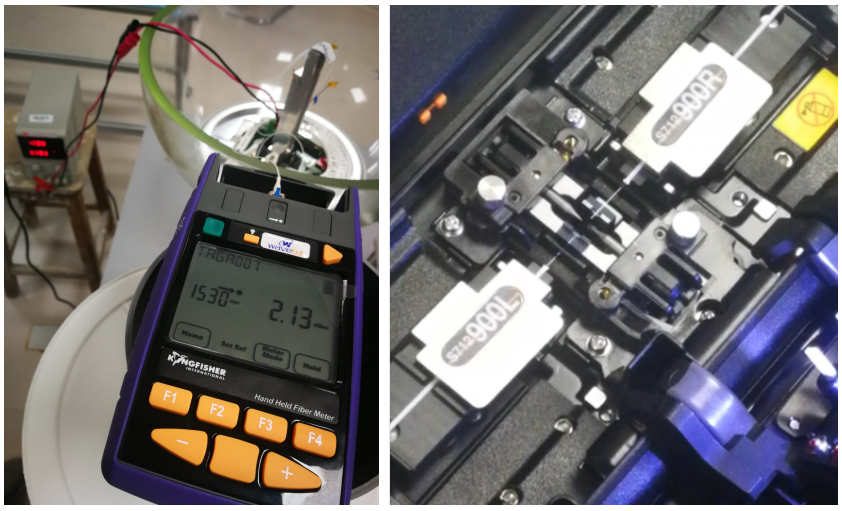

FIGURE 6.28: Left: Measurement of the optical signal originating from the CLB. Right: Optical fiber splice

6.3.4.4 Integration procedures of the top support structure

Three different components are integrated to top support structure. The first one is the led nano beacon (Fig.6.29 on the left) which is glued to the structure from the inside using mastic. The second component is the pressure gauge, glued on the outside using mastic as well. It is advisable to use a generous amount of mastic here to avoid any leaks during the gel pouring procedures. The installation of the PMTs on the top structure is next, and is performed as follows:

- The procedure starts by cleaning and mounting 12 o-rings on the support structure where PMTs are to be installed.
- The next step is the scanning of 12 PMTs and filling in the DIA with their position's number in the structure.
- Afterwards, the pigtails (connective wires) of the PMTs are labeled according to their number in the structure, this step prevents a lot of confusion when the PMTs are to be plugged in the octopus board during the instrumentation procedure.
- A protective cap is mounted on each one of the PMTs' electronic base.
- PMTs are then installed in the structure, paying attention that each new PMT installed doesn't cause the pigtail of the previous ones to bend.
- Next step is the installation of the reflector rings already prepared.

Once every component is installed, the full support structure can be placed on the glass hemisphere, the picture in Fig.6.29 (right) shows the top structure ready for the next step (instrumentation).

FIGURE 6.29: Left: The led nano-beacon being inserted in its sliding place on the top support structure. Right: The top support structure after the installetion of PMTs, pressure gauge and the nano-beacon from the inside.

6.3.4.5 Integration procedure of the bottom glass hemisphere

Unlike the integration of the top glass hemisphere which contains the electronics and the cooling components, the integration procedure of the bottom glass hemisphere is straightforward, only one component is integrated to this hemisphere, which is the piezo acoustic sensor.

Gluing the piezo acoustic sensor to the bottom glass sphere

After cleaning the area where the piezo is to to be glued, 0.5 g of a special glue is prepared by mixing two fluids with a ratio 1:1. A few drops are then applied on the piezo's contact surface and placed on the hemisphere on a marked position. In order to avoid bubbles of air between the flat surface of the piezo sensor and the curved surface of the glass, the piezo sensor is slightly rotated when in contact with the glass, this way the glue will fill up any empty space. The hemisphere is then put in the storing space while the glue hardens, which takes 24 hours.

6.3.4.6 Integration procedure of the bottom support structure

The integration procedure of the bottom support structure is similar to the top support structure with the exception of the integration of 19 PMTs instead of 12, and the absence of the nano-beacon and the piezo acoustic sensor. A bottom support structure during its integration can be seen in Fig.6.21.

After the finalization of the integration of the four branches of the DOM, the top glass hemisphere and the top support structure are merged, and in the same way the bottom glass hemisphere and the bottom support structure are merged as well. The merged halves will be referred to from here on as top and bottom hemispheres.

6.3.4.7 Instrumentation of the top and bottom hemispheres

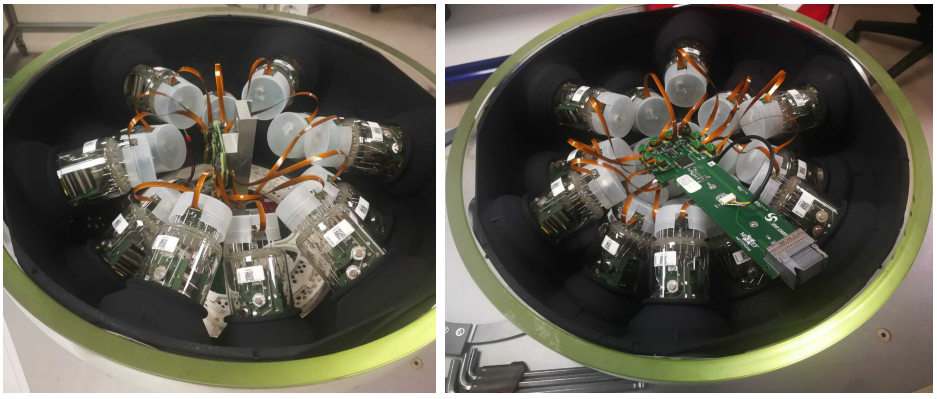

FIGURE 6.30: The DOM's top hemisphere on the left and the bottom hemisphere on the right after being instrumented.

Instrumentation of the top hemispheres

This procedure consists of connecting the top hemisphere's components to the CLB. To do so, the 12 PMTs are plugged into the octopus board in their specific order, the octopus board is then plugged into the CLB alongside the cooling bar that was mounted during the installation of the electronics. In the other hand the nano beacon is plugged directly to the CLB as can be seen in the left picture of Fig.6.30.

Instrumentation of the bottom hemispheres

Since there is no CLB in the bottom hemisphere, all the component in the bottom hemisphere are connected to the large octopus board, which will be connected to CLB at the step of the closing of the DOM. The components plugged to the large octopus

board are the 19 PMTs (in order) and the piezo sensor. An instrumented bottom hemisphere is seen in the right picture of Fig.6.30.

6.3.4.8 Functional test

Once both hemispheres are correctly instrumented, they are ready for the functional test. The objective of this test is to verify the response (functionality) of all the integrated components. In order to carry out the test while the DOM is not yet closed, a clever solution has been established to simulate a closed DOM. The large octopus board of the bottom hemisphere is plugged into a special extension cable (called internally the Leiden cable) in one end while the hand is plugged in the CLB in the top hemisphere. This way both hemispheres are connected to the CLB and communication with the DOM can be established as if it is closed, the picture in Fig.6.31 shows the setup for this test.

FIGURE 6.31: The setup of the functional, both hemispheres are connected using the Leiden cable.

To secure the connection through the optical fibers between the white Rabbit Switch, DOM, and the splitter, a specific environment program is loaded on the computer. The setup for the functional test (the acceptance test as well) is a meticulous process that will not be covered in this work.

The functional test permits to check the temperature and humidity of electronic components, whether all the PMTs are plugged correctly and if their Id correspond to those

in the data base, the functionality of the piezo, nano-beacon and the compass among others. During this test the PMTs are not put under HV (high voltage), thus darkness is not mandatory.

The chronological positioning of the functional test among the DOM integration procedures is wisely chosen, permitting the intervention in case of a non-conformity or faulty component. Since so far, all the procedures carried out allow for the correction of any mistake, the up coming procedures however are irreversible.

6.3.4.9 Gluing of the top support structure to the top glass hemisphere

After the success of the functional test of all the 7 DOMs, we proceed to the first of the irreversible operations, which is the permanent merger of the top glass hemisphere with top support structure both fully integrated.

As seen in Fig.6.32, a special brand of silicone mastic (Bison transparent) is applied on the top edge of the support structure, to be placed in the top glass hemisphere, where the mastic will be in contact with the edge of the cooling mushroom. Once positioned correctly, the structure is rotated slightly left and right so that mastic fills in any gaps. Again it is advisable to apply the mastic generously to avoid leaks during the gel pouring procedures.

FIGURE 6.32: Silicone mastic being applied to the edge of the top support structure in order to be glued to the cooling mushroom.

Once this operation is completed, the top hemisphere is placed in storage for 72 hours, so that the mastic dries completely, then it is ready for the next procedure which is the gel pouring.

6.3.4.10 Gel pouring in the top and bottom hemispheres

A picture of this procedure is in Fig.6.33, the steps are as follows:

- A funnel is mounted over the top hemisphere, connected via a transparent plastic tube to a hole in the support structure, allowing for the gel to fill is the gap between the support structure and the glass hemisphere, this will make the pouring procedure smoother.
- All the containers that will be used during this procedure are cleaned with isopropanol and wipes.
- 1450 of gel is prepared: 870g of A and 580 of B. (ratio of 60% gel A and 40% gel B).
- The gel is then mixed for around 10 minutes with 120 rounds per minute.
- The mixture is then degassed is the desiccator for around 10 minutes at an under pressure of 0.6 bar negative. Once all the bubbles are on the surface, the under pressure is released, and applied once more for a few seconds to be sure all the bubbles have popped.
- After making sure that the hemisphere is correctly leveled, the gel is poured in the funnel that's connected to the hemisphere via the clear tube, all that remains now is waiting for the hemisphere to get filled.
- In case there is a leak, the gel will not fill the hemisphere completely. In this case it is advisable to wait until the next day, giving time to the gel to harden, and an appropriate amount of gel prepared in order to complete the procedure. The additional amount is filled in via a syringe.

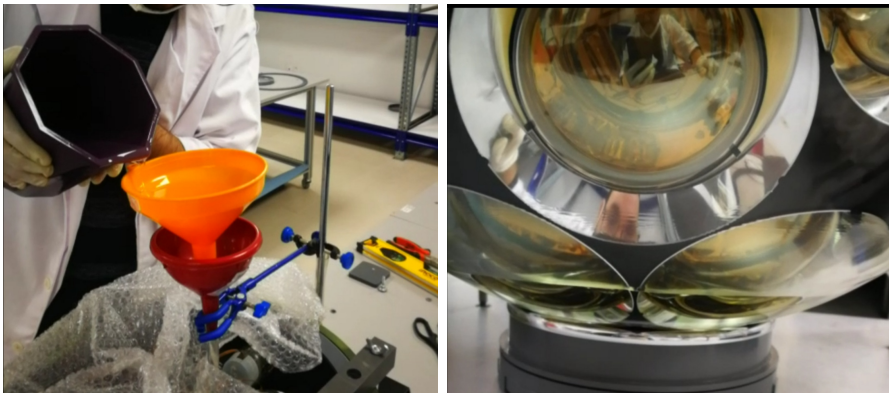

FIGURE 6.33: The left picture shows the gel being poured into the hemisphere, and the right picture shows the level of the gel rising inside the hemisphere.

For the bottom hemisphere, exactly the same procedure is followed, except for the quantity of gel used: 1260g of A and 840g of B, yielding a mixture of 2100g. The resting time for this operation is 24 hours.

6.3.4.11 DOM closure

This procedure can be tackled once the gel has hardened inside the hemispheres, i.e. 24 hours after the gel pouring. It is recommended to proceed with the closure as soon as possible after the gel has hardened. The DOM closure procedure is shown in Fig.6.34, and the steps are as follows :

- The bottom hemisphere is turned up side down and then lifted using a suction pump and a crane.
- After ensuring the correct horizontal level, the top hemisphere is placed underneath it and, using the crane, the bottom hemisphere is gently lowered.
- The sliding block mounted to the large octopus board is inserted in the cooling bar, to be plugged into the CLB once the bottom hemisphere is sufficiently lowered.
- lowering is kept until closing, while making sure the holes and springs in both support structures are aligned.

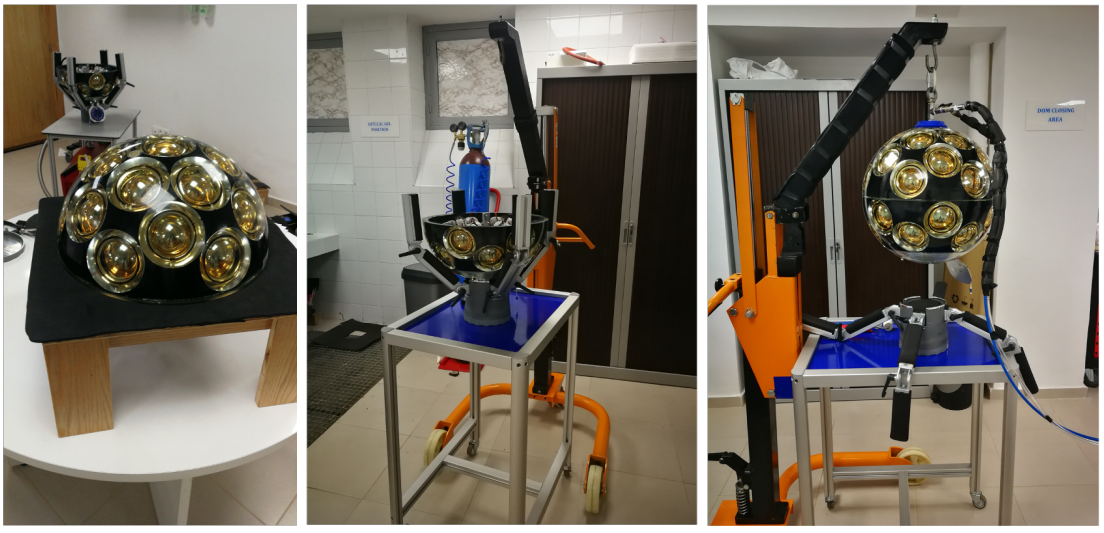

FIGURE 6.34: The procedure of DOM closure

Once the edges of the glass hemispheres are in contact, we make sure they are correctly positioned (using fingers) and we adjust when necessary. Now we proceed to secure the closing by slowly extracting the air from inside the DOM through the valve, using the pump, until an under pressure value of 0.2 bar negative is reached. Terostat is the

applied around the equator for 1 turn, followed by the scotch tape for 3 turns to seal the DOM. The picture in Fig.6.6 shows the first DOM assembled in Rabat closed and sealed, and ready for the acceptance test.

6.3.4.12 Acceptance test

The DOM integration procedures are finalized with the acceptance, it is similar to the previously discussed functional test with further verification.

This process performs a series of checks on each component of the DOM using a set of predetermined criteria, with the goal of determining all necessary parameters and assessing whether the DOM is suitable for DU integration.

During this test, a period of 24 hours of darkening for the PMTs is mandatory. Afterward, the test will be carried out in darkness inside the a light tight dark box, as seen in the picture in Fig.6.35.

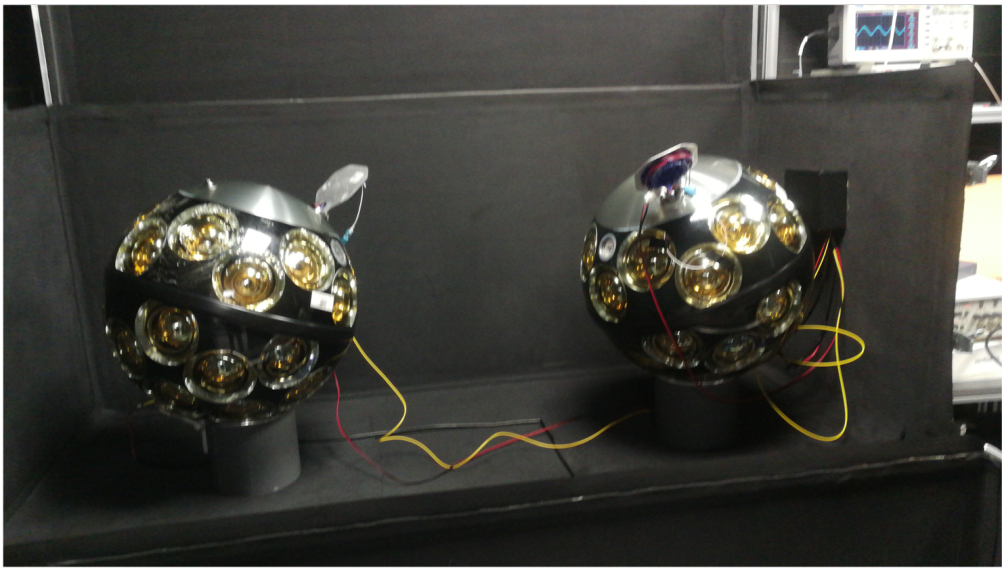

FIGURE 6.35: Dark box used to perform the functional and the acceptance tests, 2 of them are available in the Rabat site. The dark boxes are found in a dark room to further ensure light tightness during the tests.

The acceptance test includes almost all the checks performed in the functional, with the addition of the dark rate count and time over threshold (tot) of all the PMTs. Also the measurement of the compass during which the DOM is rotated facing four directions (north, west, south and east), remaining 1 minute in each while the measurement is being taken, the bottom plots of Fig.6.36 show the result of the compass check. Another verification is added to this test, which is the checking of the piezo acoustic sensor, where a sound of a frequency of 30KHz is sent via a special exterior piezo emitter to visualize

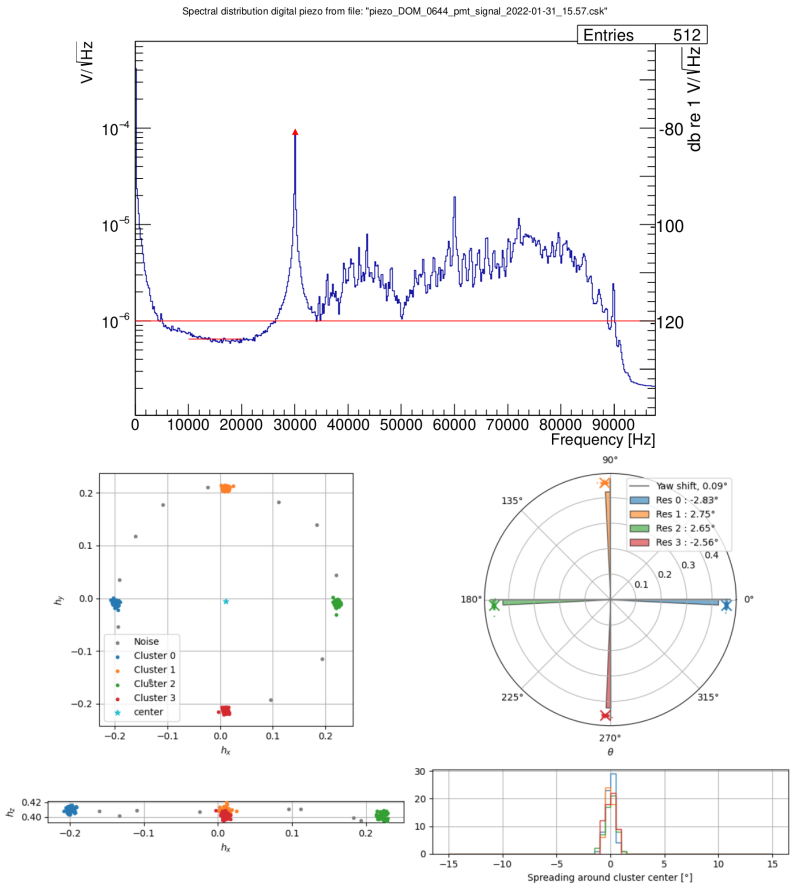

FIGURE 6.36: The result of the piezo test is shown in the top plot, a clear peak is seen around 30KHz in the X axis, meaning the piezo sensor is functioning correctly. The bottom plots correspond to the compass test, all the points are concentrated in the four cardinal directions, meaning the compass is functioning correctly.

the reaction of the piezo sensor inside the DOM. The result of the piezo test can be seen in the top plot of Fig.6.36.

FIGURE 6.37: The first set of 7 DOMs integrated in the Rabat site after successfully passing the acceptance test.

The 7 DOMs integrated in the Rabat site passed the acceptance test successfully (Fig.6.37). Three NCRs have been raised for three DOMs but they are of a minor nature.

6.3.4.13 Mounting the collar

The very last procedure of DOM integration is the mounting of the collar, in this operation the closed DOM is surrounded by a special titanium alloy collar, tightened with 2 titanium alloy bolts with a torque of 3Nm. The titanium alloy is chosen due to its resistance to the harsh conditions the DOM will deployed in.

With the mounting of the collar, the DOM is ready to be integrated in a DU. The picture of Fig.6.38 shows one of the DOMs integrated in Rabat with the collar mounted.

FIGURE 6.38: One of the DOMs assembled in the Rabat site with the collar, ready for shipment.

The table if Fig.6.39 is a summary of all the DOM integration procedures carried out in the Rabat site for the first set of 7 DOMs.

	CH53H	CH51H	CH49H	CH47H	CH45H	CH43H	CH41H
Cooling mushroom Gluing	OK	OK	OK	OK	OK	OK	OK
Electronics installation	OK	OK	OK	OK	OK	OK	OK
Penetrator mounting	OK	OK	OK	OK	OK	OK	OK
Helium test	OK	OK	OK	OK	OK	OK	OK
Optical splice	OK	OK	OK	OK	OK	OK	OK
Piezo gluing	OK	OK	OK	OK	OK	OK	OK
Pressure gauge and nano beacon gluing	OK	OK	OK	OK	OK	OK	OK
Pmt integration top (+ reflectors and o-rings)	OK	OK	OK	OK	OK	OK	OK
Pmt integration bottom	OK	OK	OK	OK	OK	OK	OK
Instrumentation of top hemisphere	OK	OK	OK	OK	OK	OK	OK
Instrumentation of bottom hemisphere	OK	OK	OK	OK	OK	OK	OK
Functional test	OK	OK	OK	OK	OK	Ok	Ok
Gluing top structure onto cooling mushroom	OK	OK	OK	OK	OK	OK	OK
Gel pouring top hemisphere	OK	OK	OK	OK	OK	OK	OK
Gel pouring bottom hemisphere	OK	OK	OK	OK	OK	OK	OK
Closing the DOM	OK	OK	OK	OK	OK	OK	OK
Mounting of the collar	OK	OK	OK	OK	OK	OK	OK
Acceptance test	OK	OK	OK (-1pmt)	OK(-2gains - compass)	OK (-6gains)	OK(-4gains - 1rate)	OK (-2gains)
				NCR	NCR	NCR	

FIGURE 6.39: A summary and results of all the DOM integration procedures carried out in the Rabat site for the first set of 7 DOMS.

6.4 BM integration in Oujda site

Morocco participates in the integration of the ORCA base module (BM) in Mohammed first university of Oujda, in addition to the DOM integration site in Rabat. In Oujda, a group of researchers has recently finished the integration of the first base module. CPPM Marseille, LUPM Montpellier, IFIC Valencia, and Oujda are the four sites that are currently integrating ORCA base module for KM3NeT. In addition, a new location in Demokritos, Athens, is being prepared. (Fig.6.40).

FIGURE 6.40: The integration sites of the KM3NeT Base Module, the blue dots represent site of ORACA-BM integration while the red dots represent ARCA-BM.

A base module is a component found at the basis of each detection unit. Its function is to provide a single connection between a row of four DUs and the junction box node, as well as four detecting units. ORCA contains four different sorts of BMs: A, B, C, and D. The last one (D type BM) is likewise separated into two types depending on whether the calibration unit (CU) is contained in the DU or not.

6.4.1 The ORCA BM

Four DUs must be connected to the node through a single connection in the ORCA detector. Each DU is linked to a different base module to suit this need. A Calibration unit might be at the end of the four-DU row. Fig.6.41 shows the ORCA arrangement, which has five different configurations based on their position in the row and whether or not a CU is connected to the rows.

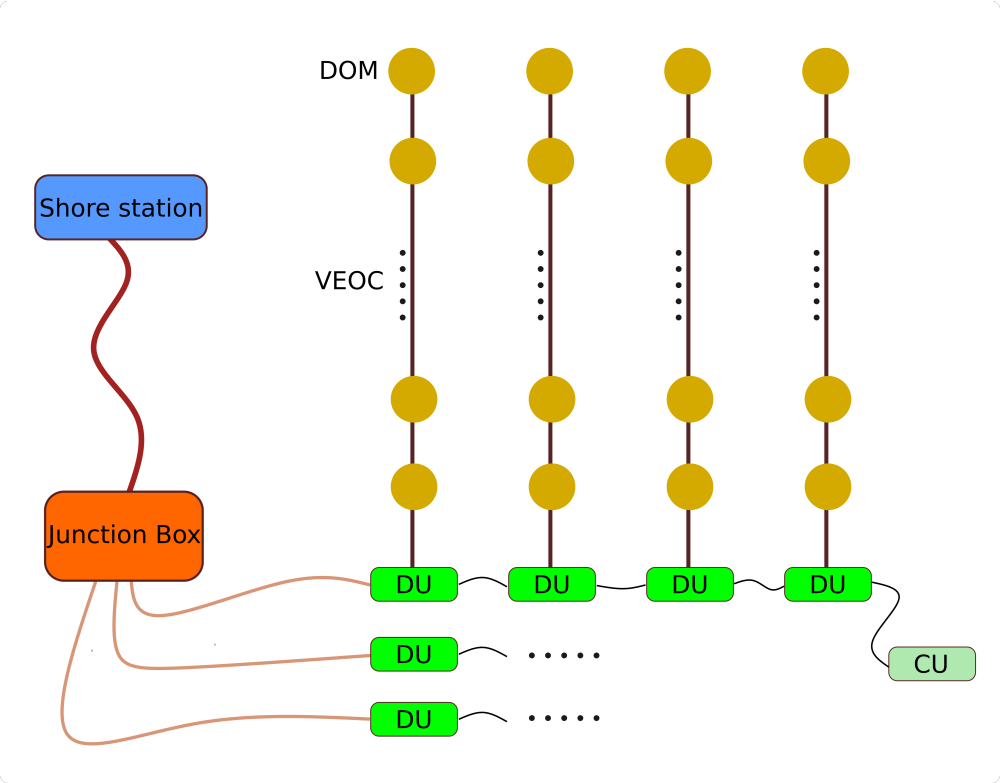

FIGURE 6.41: The ORCA layout is depicted schematically, with four DUs in a chain arrangement. A calibration unit (CU) can be used to end each chain. The DUs' base modules are of type A, B, C, and D (from left to right).

- Type A: This is the type of BM attached to the first DU in the row; it collects the slow control (SC) data from the four DUs and multiplexes it onto a single optical cable, which is then connected to the node through an optical component called an Interleaver. The optical signal arriving to the BM is divided 80/20 in this setup. The BM gets 20% of the credit, while the rest of the row gets 80%.

- Type B: In this design, the incoming signal is divided into a 70/30 ratio, with 30% of the signal going to the BM in question and 70% going to the remainder of the row.

- Type C: In this setup, the incoming signal is divided into a 60/40 split, with 40% going to the BM in question and 60% going to the remainder of the row.

- Type D with CU: In this situation, the incoming SC optical signal is divided into a 20/80 ratio, with 80 percent going to the BM in question and the remainder of the row getting the remaining 20%.

- Type D without CU: The BM receives the entire dedication of the entering SC optical signal.

6.4.2 The mechanics of ORCA BM

The BM mechanics must fulfill certain standards due to the nature of the setting in which it will be employed. To withstand the pressures that surround these components, a titanium alloy cylindrical container was used. Fig.6.42 shows a schematic drawing of the container, which is supplied by an experienced corporation. The container's requirements are:

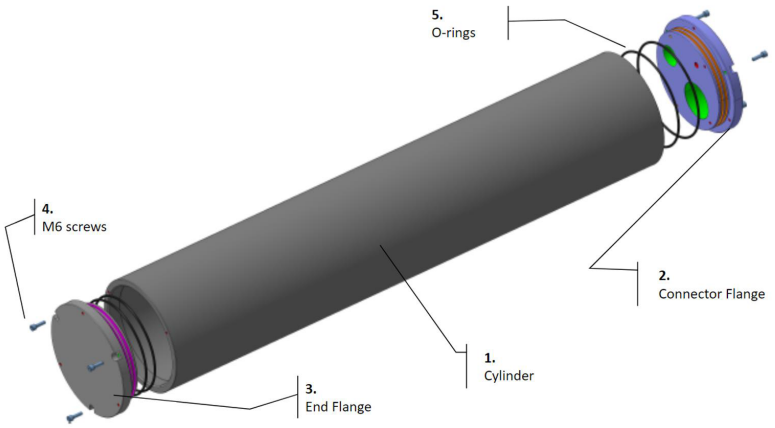

FIGURE 6.42: The container of the BM designed to withstand high pressures experienced at a depth of roughly 2500 meters in the Mediterranean Sea.

- With a safety factor of 1.5, it is resistant to the service pressure (250 bars).
- Corrosion-resistant for a 15-year lifespan.
- The product has already been pressure tested and certified.
- Permits the communication with the DU, seafloor infrastructure and external equipment (hydrophone,)

Connector flanges and blind flanges are used to seal the BM cylindrical container. Each flange is linked to the container with two O-rings and three M6 screws to ensure water tightness. The interlink penetrator, the *Vertical Electro Optical Cable* (VEOC) penetrator, and the hydrophone connection are all housed in three holes on the standard flange (Fig6.43 shows the BM container flanges). From a pressure standpoint, this product was initially certified. Nonetheless, when the holes were machined, several pressure tests were performed to validate the flange.

The optical part of ORCA BMs holds the optical components, while the electronics part includes the electronics needed to distribute the electrical signals among the DU DOMs. The third portion of the BM is the power section, and its job is to supply electric power to the base module (Fig.6.44 shows the schematics of the ORCA BM's three parts).

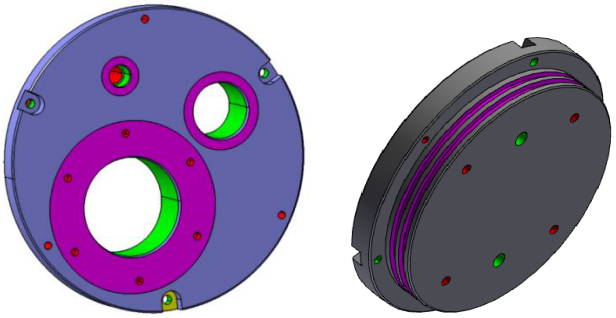

FIGURE 6.43: The flanges of the ORCA BM's container are shown schematically. The connection flange is on the left, while the end flange is on the right.

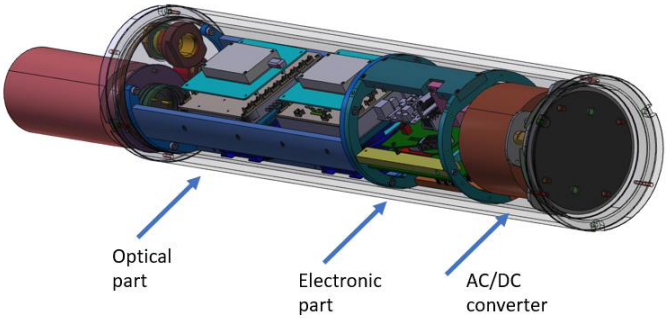

FIGURE 6.44: The three sections of the ORCA base module are shown schematically.

The team of Oujda BM integration site have recently integrated their first OCRA-BM, the pictures in Fig.6.45 showcases the two sides of the first BM integrated in the Oujda site.

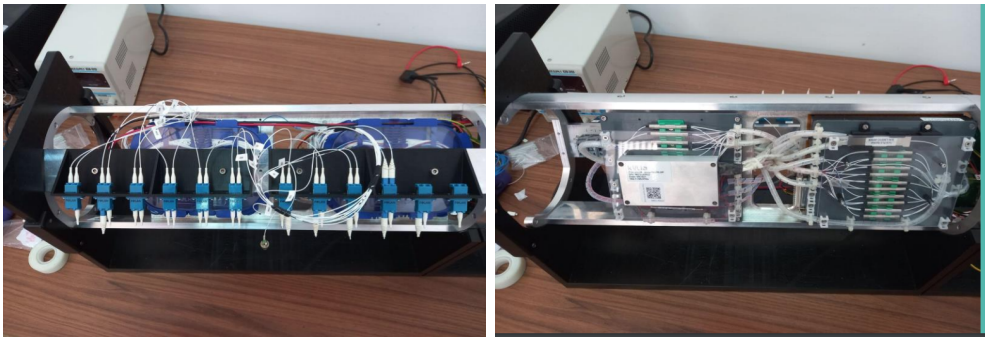

FIGURE 6.45: The first BM integrated in the Oujda site showcased from two sides.

6.5 KM3NeT Construction and deployment history and perspectives

The KM3NeT's pre-production Digital Optical Module (PPM-DOM) variant was installed at the sea in 2013, connected with the ANTARES detector [106]. Between May

2014 and July 2015, the KM3NeT-It facility used a pre-production detection unit (PPM-DU) with three DOMs [107]. The PPM-DU gave the first data on reconstructed atmospheric muons and allowed the DOM calibration methods to be tested.

ARCA's first DU was deployed in December 2015 followed by two more DUs were installed in 2016. Data collection began immediately after installation. Between April 2017 until January 2019, activities at the KM3NeT-It facility were halted due to electrical issues with the sea floor equipment, following which data collection restarted. In 2019, operations at the ARCA site were again halted due to shore station renovations. The detector was successfully upgraded in April 2021, additionally ARCA has five additional detection units that have been connected and are functional. In September 2021, 2 more DUs were added to the ARCA block, corresponding to the current status being 8 active lines (Fig.6.46 top picture). A sea campaign in programmed in June 2022 to add more DUs to the ARCA detector.

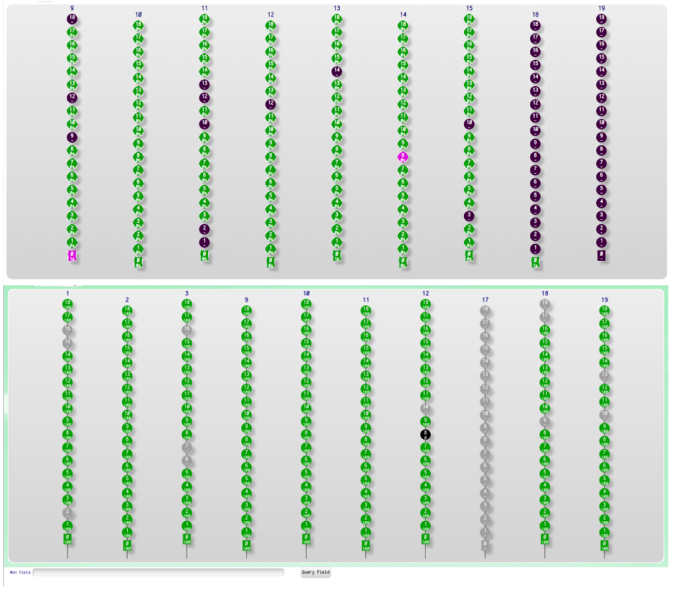

FIGURE 6.46: ARCA's 8 functional DUs on the top and ORCA's 10 functional DUs on the bottom, corresponding to the current status of the KM3NeT telescope (June 2022).

The first ORCA DU was deployed in September 2017 and functioned until the primary electro-optical cable failed in mid-December 2017. Following the repair of a portion in the main cable [108], data collection was restarted in February 2019. Between May and July 2019, four further ORCA DUs were deployed, but the first DU had to be recovered owing to inadvertent damage. Two more ORCA DUs were deployed in January 2020, increasing the total number of operational strings to six. On November 2021 a new sea campaign was launched to bring the number of ARCA DUs to 10 (Fig.6.46 bottom picture), which have been functioning correctly as of the time of the writing of this report.

6.6 Conclusion

The KM3NeT telescope is in the early stages of the construction. Having recently completed the phase I of the project, which consisted of the deployment of few lines as prototype.

The current step of the project, phase II, will focus on a mass production of DOMs, DUs and BMs, the completion of the KM3NeT telescope construction is foreseen at around 2028 for ORCA and 2030 for the 2 blocks of ARCA.

The Moroccan institutes are contributing to this task, and are expected to reach mass production level as well, which consist a valuable opportunity of learning for the Moroccan scientists.

Appendix A

Landau distribution

The Bethe-Bloch formula [55, 109] describes the average energy loss of charged particles as they move through matter. Landau [110] theoretically explained the variations in energy loss caused by ionization of a charged particle in a thin layer of matter. This section concludes with a universal asymmetric probability density function for positive values, which has a small peak and a lengthy tail. The low number of individual collisions, each with a modest possibility of transmitting proportionally significant quantities of energy, causes this tail to gravitate towards positive values as shown in Fig.A.1. The Landau probability density function's integral representation is written as follows:

$$\phi(c) = \frac{1}{\pi} \int_0^\infty x^{-x} \sin(\pi x) \exp(-cx) dx \tag{A.1}$$

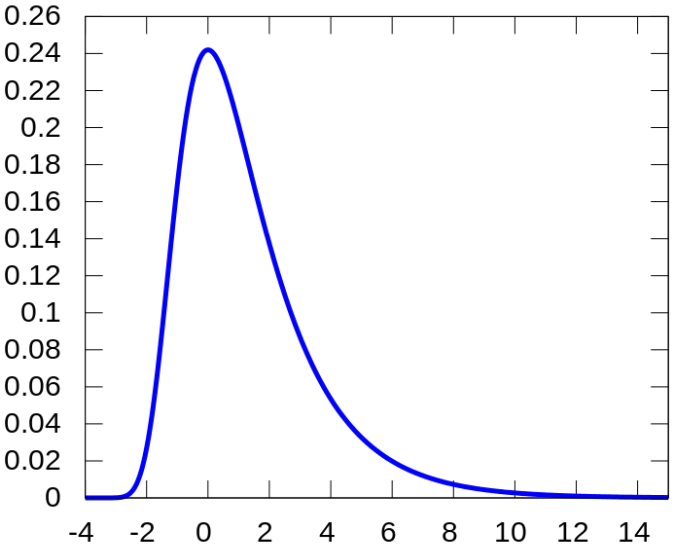

FIGURE A.1: The probability Density Function of the Landau distribution.

The N_{sh} distribution utilized in this research refers to the overall amount of light released by each event, as well as the number of storeys that detected light from it. The energy loss in the medium is proportional to the number of photons released by a muon track. The Landau distribution in Fig.5.6 fits the distribution of N_{sh} for muons perfectly under this assumption.

Bibliography

[1] Alan H. Guth and Erick J. Weinberg. Could the Universe Have Recovered from a Slow First Order Phase Transition? *Nucl. Phys. B*, 212:321–364, 1983.

[2] J. H. Christenson, J. W. Cronin, V. L. Fitch, and R. Turlay. Evidence for the 2π Decay of the K_2^0 Meson. *Phys. Rev. Lett.*, 13:138–140, 1964.

[3] N. D. Mermin. The topological theory of defects in ordered media. *Rev. Mod. Phys.*, 51:591–648, 1979.

[4] Gerard 't Hooft. Magnetic Monopoles in Unified Gauge Theories. *Nucl. Phys. B*, 79:276–284, 1974.

[5] Alexander M. Polyakov. Particle Spectrum in Quantum Field Theory. *JETP Lett.*, 20:194–195, 1974.

[6] Abbasi et al. Search for relativistic magnetic monopoles with the amanda-ii neutrino telescope: The icecube collaboration. *European Physical Journal C*, 69:361–378, 10 2010.

[7] Georges Aad et al. Search for magnetic monopoles and stable particles with high electric charges in 8 TeV *pp* collisions with the ATLAS detector. *Phys. Rev. D*, 93(5):052009, 2016.

[8] S. Adrian-Martinez et al. Search for Relativistic Magnetic Monopoles with the ANTARES Neutrino Telescope. *Astropart. Phys.*, 35:634–640, 2012.

[9] M. G. Aartsen et al. Searches for Relativistic Magnetic Monopoles in IceCube. *Eur. Phys. J. C*, 76(3):133, 2016.

[10] Marco Circella. The construction of ANTARES, the first undersea neutrino telescope. *Nucl. Instrum. Meth. A*, 602:1–6, 2009.

[11] Enrico Fermi. Versuch einer theorie der β-strahlen. i. *Zeitschrift für Physik*, 88(3):161–177, 1934.

[12] A. Yu. Smirnov. The MSW effect and matter effects in neutrino oscillations. *Phys. Scripta T*, 121:57–64, 2005.

[13] Yusuke Koshio. *Study of Solar Neutrinos at Super-Kamiokande*. PhD thesis, Tokyo U., 1998.

[14] Giorgio Giacomelli and Miriam Giorgini. Atmospheric neutrino oscillations in MACRO. In *NO-VE International Workshop on Neutrino Oscillations in Venice*, pages 207–220, 10 2001.

[15] Kate Scholberg. Supernova neutrino detection. *Nuclear Physics B - Proceedings Supplements*, 91(1):331–337, 2001. Neutrino 2000.

[16] P. A. Cherenkov. Visible luminescence of pure liquids under the influence of γ-radiation. *Dokl. Akad. Nauk SSSR*, 2(8):451–454, 1934.

[17] P Amram et al. The antares optical module. *Nuclear Instruments and Methods in Physics Research Section A: Accelerators, Spectrometers, Detectors and Associated Equipment*, 484(1):369–383, 2002.

[18] J. A. Aguilar et al. Performance of the front-end electronics of the ANTARES neutrino telescope. *Nucl. Instrum. Meth. A*, 622:59–73, 2010.

[19] F. Druillole, D. Lachartre, F. Feinstein, E. Delagnes, H. Lafoux, C. Hadamache, and J. Fopma. The analog ring sampler: An ASIC for the front-end electronics of the ANTARES neutrino telescope. *IEEE Trans. Nucl. Sci.*, 49:1122–1129, 2002.

[20] J.A. Aguilar et al. The data acquisition system for the antares neutrino telescope. *Nuclear Instruments and Methods in Physics Research Section A: Accelerators, Spectrometers, Detectors and Associated Equipment*, 570(1):107–116, 2007.

[21] A. G. Dickson and C. Goyet. Handbook of methods for the analysis of the various parameters of the carbon dioxide system in sea water, 1994.

[22] G. Audi, O. Bersillon, J. Blachot, and A. H. Wapstra. The Nubase evaluation of nuclear and decay properties. *Nucl. Phys. A*, 729:3–128, 2003.

[23] J. Brunner. Simulation of 40K Signals internal note Site/1999-002. *ANTARES Collaboration*, 1999.

[24] Jun S Song. Theory of magnetic monopoles and electric-magnetic duality: A prelude to s-duality. *J. Undergrad. Sci*, 3:47–55, 1996.

[25] Paul Adrien Maurice Dirac. Quantised singularities in the electromagnetic field,. *Proc. Roy. Soc. Lond. A*, 133(821):60–72, 1931.

[26] Steven Weinberg. *The quantum theory of fields. Vol. 2: Modern applications.* Cambridge University Press, 8 2013.

[27] T. W. B. Kibble. Topology of Cosmic Domains and Strings. *J. Phys. A*, 9:1387–1398, 1976.

[28] John P Preskill. Cosmological production of superheavy magnetic monopoles. *Physical Review Letters*, 43(19):1365, 1979.

[29] Michael S. Turner, E. N. Parker, and T. J. Bogdan. Magnetic monopoles and the survival of galactic magnetic fields. *Phys. Rev. D*, 26:1296–1305, Sep 1982.

[30] G. Giacomelli. Magnetic monopoles. *a Rivista del Nuovo Cimento 7(12), 1*, 7, 1984.

[31] Steven Weinberg. *The Quantum Theory of Fields*, volume 2. Cambridge University Press, 1996.

[32] H. Georgi, H. R. Quinn, and S. Weinberg. Hierarchy of interactions in unified gauge theories. *Phys. Rev. Lett.*, 33:451–454, Aug 1974.

[33] M. Daniel, George Lazarides, and Q. Shafi. SU(5) Monopoles, Magnetic Symmetry and Confinement. *Nucl. Phys. B*, 170:156–164, 1980.

[34] Thomas W. Kephart and Thomas J. Weiler. Magnetic monopoles as the highest energy cosmic ray primaries. *Astroparticle Physics*, 4(3):271–279, 1996.

[35] Paul H. Frampton and Bum-Hoon Lee. Su(15) grand unification. *Phys. Rev. Lett.*, 64:619–621, Feb 1990.

[36] Paul H. Frampton and Thomas W. Kephart. Higgs sector and proton decay in su(15) grand unification. *Phys. Rev. D*, 42:3892–3894, Dec 1990.

[37] S.F King and Q Shafi. Minimal supersymmetric su(4)×su(2)l×su(2)r. *Physics Letters B*, 422(1):135–140, 1998.

[38] Thomas W. Kephart, Chin-Aik Lee, and Qaisar Shafi. Family unification, exotic states and light magnetic monopoles. *JHEP*, 01:088, 2007.

[39] Keith R. Dienes, Emilian Dudas, and Tony Gherghetta. Grand unification at intermediate mass scales through extra dimensions. *Nuclear Physics B*, 537(1):47–108, 1999.

[40] Ignatios Antoniadis, Nima Arkani-Hamed, Savas Dimopoulos, and Gia Dvali. New dimensions at a millimeter to a fermi and superstrings at a tev. *Physics Letters B*, 436(3):257–263, 1998.

[41] Anna Pollmann. Searches for magnetic monopoles with icecube. *EPJ Web of Conferences*, 168:04010, 01 2018.

[42] Stuart D Wick, Thomas W Kephart, Thomas J Weiler, and Peter L Biermann. Signatures for a cosmic flux of magnetic monopoles. *Astroparticle Physics*, 18(6):663–687, 2003.

[43] Eric Huguet and Patrick Peter. Bound states in monopoles: sources for uhecr? *Astroparticle Physics*, 12(4):277–289, 2000.

[44] Stuart D. Wick, Thomas W. Kephart, Thomas J. Weiler, and Peter L. Biermann. Signatures for a cosmic flux of magnetic monopoles. *Astroparticle Physics*, 18(6):663–687, 2003.

[45] Eugene N. Parker. The Origin of Magnetic Fields. *Astrophys. J.*, 160:383, 1970.

[46] C. Patrignani et al. Chin. Phys. C, 40, 100001 (2016) and 2017 update.

[47] L. Patrizii and M. Spurio. Status of Searches for Magnetic Monopoles. *Ann. Rev. Nucl. Part. Sci.*, 65:279–302, 2015.

[48] M. Ambrosio et al. Final results of magnetic monopole searches with the MACRO experiment. *Eur. Phys. J. C*, 25:511–522, 2002.

[49] E. Bauer. The energy loss of free magnetic poles in passing through matter. *Math. Proc. Cambridge Phil. Soc.*, 47(04):777, 1951.

[50] H. J. D. Cole. The theoretical behaviour of a magnetic monopole in a wilson cloud chamber. *Mathematical Proceedings of the Cambridge Philosophical Society*, 47(1):196–206, 1951.

[51] S. P. Ahlen. Monopole Track Characteristics in Plastic Detectors. *Phys. Rev. D*, 14:2935–2940, 1976.

[52] S. P. Ahlen. Stopping Power Formula for Magnetic Monopoles. *Phys. Rev. D*, 17:229–233, 1978.

[53] Yoichi Kazama, Chen Ning Yang, and Alfred S. Goldhaber. Scattering of a Dirac Particle with Charge Ze by a Fixed Magnetic Monopole. *Phys. Rev. D*, 15:2287–2299, 1977.

[54] RM Sternheimer and RF Peierls. General expression for the density effect for the ionization loss of charged particles. *Physical Review B*, 3(11), 1971.

[55] F. Bloch. Leipzig,. *Annals of Physics*, 16(285), 1933.

[56] J. Posselt. Search for Relativistic Magnetic Monopoles with the IceCube 40-String Detector, Ph.D. thesis, University of Wuppertal. 2013.

[57] S.R. Kel'ner. *Sov. J. Nucl. Phys.*, 5(778), 1967.

[58] S.R. Kel'ner, Yu.D. Kotov. *Sov. J. Nucl. Phys.*, 7(237), 1968.

[59] S. Iyer Dutta, M. H. Reno, I. Sarcevic, and D. Seckel. Propagation of muons and taus at high energies. *Phys. Rev. D*, 63:094020, Apr 2001.

[60] J. Derkaoui, G. Giacomelli, T. Lari, A. Margiotta, M. Ouchrif, L. Patrizii, V. Popa, and V. Togo. Energy losses of magnetic monopoles and of dyons in the earth. *Astropart. Phys.*, 9:173–183, 1998.

[61] V. A. Rubakov. Superheavy Magnetic Monopoles and Proton Decay. *JETP Lett.*, 33:644–646, 1981.

[62] V. A. Rubakov. Adler-Bell-Jackiw Anomaly and Fermion Number Breaking in the Presence of a Magnetic Monopole. *Nucl. Phys. B*, 203:311–348, 1982.

[63] Curtis G. Callan, Jr. Disappearing Dyons. *Phys. Rev. D*, 25:2141, 1982.

[64] Curtis Gove Callan. Dyon-fermion dynamics. *Physical review D: Particles and fields*, 26(8):2058–2068, 1982. Copyright: Copyright 2015 Elsevier B.V., All rights reserved.

[65] Donald R. Tompkins. Total energy loss and Čerenkov emission from monopoles. *Phys. Rev.*, 138:B248–B250, Apr 1965.

[66] Steven P. Ahlen. Theoretical and experimental aspects of the energy loss of relativistic heavily ionizing particles. *Rev. Mod. Phys.*, 52:121–173, Jan 1980.

[67] D.E. Groom, S.R. Klein. *Particle Data Group, Passage of Particles through Matter.* European Physical Journal C 3 144, 1998.

[68] A. Albert et al. Search for magnetic monopoles with ten years of the ANTARES neutrino telescope. *Journal of High Energy Astrophysics*, 34:1–8, 2022.

[69] Bruno Benedetto Rossi. *High-energy particles.* Prentice-Hall physics series. Prentice-Hall, New York, NY, 1952.

[70] R. M. Sternheimer. Density effect for the ionization loss in various materials. *Phys. Rev.*, 103:511–515, Aug 1956.

[71] Stephen M. Seltzer and Martin J. Berger. Improved procedure for calculating the collision stopping power of elements and compounds for electrons and positrons. *The International Journal of Applied Radiation and Isotopes*, 35(7):665–676, 1984.

[72] Gerald R. Lynch and Orin I. Dahl. Approximations to multiple coulomb scattering. *Nuclear Instruments and Methods in Physics Research Section B: Beam Interactions with Materials and Atoms*, 58(1):6–10, 1991.

[73] P. A. Zyla et al. Review of Particle Physics. *PTEP*, 2020(8):083C01, 2020.

[74] B. A. P. van Rens. Detection of Magnetic Monopoles below the Cherenkov Limit, Ph.D Thesis, NIKHEF, Amsterdam, The Netherlands.

[75] Application Software Group, GEANT, CERN Program Library Long Writeup W5013. 1993.

[76] J. Brunner. GEASIM. March 2000.

[77] N.P. Clemente. Ph.D. Thesis, Université de la Méditérranée - AixMarseille II, France. 2010.

[78] G. Carminati, M. Bazzotti, A. Margiotta, and M. Spurio. Atmospheric MUons from PArametric formulas: a fast GEnerator for neutrino telescopes (MUPAGE). *Computer Physics Communications*, 179(12):915–923, 2008.

[79] Y. Becherini, A. Margiotta, M. Sioli, and M. Spurio. A Parameterisation of single and multiple muons in the deep water or ice. *Astropart. Phys.*, 25:1–13, 2006.

[80] Vivek Agrawal, T. K. Gaisser, Paolo Lipari, and Todor Stanev. Atmospheric neutrino flux above 1-GeV. *Phys. Rev. D*, 53:1314–1323, 1996.

[81] G. Battistoni, A. Ferrari, T. Montaruli, and P. R. Sala. The atmospheric neutrino flux below 100-MeV: The FLUKA results. *Astropart. Phys.*, 23:526–534, 2005.

[82] Morihiro Honda, T Kajita, K Kasahara, and S Midorikawa. Calculation of the flux of atmospheric neutrinos. *Physical Review D*, 52(9):4985, 1995.

[83] J. Brunner. ANTARES simulation tools, Proceedings of the VLVnT 2003, Amsterdam. 2003.

[84] A. Margiotta. Common simulation tools for large volume neutrino detectors. *Nucl. Instrum. Meth. A*, 725:98–101, 2013.

[85] G. D. Barr, T. K. Gaisser, S. Robbins, and Todor Stanev. Uncertainties in Atmospheric Neutrino Fluxes. *Phys. Rev. D*, 74:094009, 2006.

[86] C. G. S. Costa. The Prompt lepton cookbook. *Astropart. Phys.*, 16:193–204, 2001.

[87] P. Antonioli, C. Ghetti, E.V. Korolkova, V.A. Kudryavtsev, and G. Sartorelli. A three-dimensional code for muon propagation through the rock: Music. *Astroparticle Physics*, 7(4):357–368, 1997.

[88] S. Navas and L. Thompson. KM3 User Guide and Reference Manual, ANTARES internal note Soft/1999-011. November 1999.

[89] J.A. Aguilar, et al. A fast algorithm for muon track reconstruction and its application to the antares neutrino telescope. *Astroparticle Physics*, 34(9):652–662, 2011.

[90] C. Reed. CalReal Update, Antares collaboration Meeting, Paris, 17th June 2008.

[91] F. James and M. Roos. Minuit - a system for function minimization and analysis of the parameter errors and correlations. *Computer Physics Communications*, 10(6):343–367, 1975.

[92] H. van Haren and et al. Acoustic and optical variations during rapid downward motion episodes in the deep north-western mediterranean sea. *Deep Sea Research Part I: Oceanographic Research Papers*, 58(8):875–884, 2011.

[93] Gary C. Hill and Katherine Rawlins. Unbiased cut selection for optimal upper limits in neutrino detectors: the model rejection potential technique. *Astroparticle Physics*, 19(3):393–402, 2003.

[94] Gary J. Feldman and Robert D. Cousins. A Unified approach to the classical statistical analysis of small signals. *Phys. Rev. D*, 57:3873–3889, 1998.

[95] S. Adrián-Martínez et al. Searches for Point-like and extended neutrino sources close to the Galactic Centre using the ANTARES neutrino Telescope. *The Astrophysical Journal*, 786(1):L5, apr 2014.

[96] A. Albert et al. Search for relativistic magnetic monopoles with five years of the ANTARES detector data. *JHEP*, 07:054, 2017.

[97] R. Abbasi et al. Search for Relativistic Magnetic Monopoles with Eight Years of IceCube Data. *Phys. Rev. Lett.*, 128:051101, 2022.

[98] K. Antipin et al. Search for relativistic magnetic monopoles with the Baikal Neutrino Telescope. *Astropart. Phys.*, 29:366–372, 2008.

[99] Maurizio Spurio. *Searches for Magnetic Monopoles and other Stable Massive Particles*, pages 353–400. 2020.

[100] S Adrián-Martínez et al. Letter of intent for KM3net 2.0. *Journal of Physics G: Nuclear and Particle Physics*, 43(8):084001, jun 2016.

[101] KM3NeT Collaboration. The KM3NeT multi-PMT optical module, 2022.

[102] S. Aiello et al. Characterisation of the hamamatsu photomultipliers for the KM3net neutrino telescope. *Journal of Instrumentation*, 13(05):P05035–P05035, may 2018.

[103] S. Adrián-Martínez et al. A method to stabilise the performance of negatively fed KM3net photomultipliers. *Journal of Instrumentation*, 11(12):P12014–P12014, dec 2016.

[104] P. Timmer, E. Heine, and H. Peek. Very low power, high voltage base for a photo multiplier tube for the KM3NeT deep sea neutrino telescope. *JINST*, 5:C12049, 2010.

[105] D Gajanana, V Gromov, and P Timmer. ASIC design in the KM3net detector. *Journal of Instrumentation*, 8(02):C02030–C02030, feb 2013.

[106] S. Adrián-Martínez et al. Deep sea tests of a prototype of the KM3NeT digital optical module. *Eur. Phys. J. C*, 74(9):3056, 2014.

[107] S. Adrián-Martínez et al. The prototype detection unit of the KM3NeT detector. *Eur. Phys. J. C*, 76(2):54, 2016.

[108] M. Ageron et al. Dependence of atmospheric muon flux on seawater depth measured with the first KM3NeT detection units: The KM3NeT Collaboration. *Eur. Phys. J. C*, 80(2):99, 2020.

[109] H. Bethe. Theory of the Passage of Fast Corpuscular Rays Through Matter. *Annalen Phys.*, 5:325–400, 1930.

[110] L. Landau. On the energy loss of fast particles by ionization. *J. Phys. (USSR)*, 8:201–205, 1944.

Résumé

Les monopôles magnétiques sont des particules hypothétiques qui peuvent être détectées par leur émission directe Cherenkov ou celle des secondaires relativistes dans les milieux transparents. Les télescopes à neutrinos à grande échelle conçus pour détecter l'émission Cherenkov de secondes produites dans les collisions de neutrinos à haute énergie fournissent des sondes sensibles d'un flux cosmique de monopôles. Ce signal particulier a été étudié par divers télescopes à neutrinos comme IceCube, ANTARES, Baikal et AMANDA dans le passé. Ce travail montre une nouvelle analyse avec des données ANTARES collectées sur dix ans (janvier 2008 à décembre 2017) qui améliore les limites précédentes de la collaboration. Par rapport aux précédentes recherches ANTARES, cette analyse utilise une stratégie de simulation run-by-run, avec une plus grande exposition ainsi qu'une nouvelle simulation des monopôles magnétiques prenant en compte le modèle de Kasama, Yang et Goldhaber pour leur interaction de section avec la matière. Aucun signal compatible avec le passage des monopôles magnétiques relativistes n'est observé, et des limites supérieures sur le flux des monopôles magnétiques avec $\beta = v/c \geq 0{,}55$, sont présentées. Pour les monopôles magnétiques ultra-relativistes, la limite de flux est $\sim 7 \times 10 - 18$ cm $^{-2}$ s $^{-1}$ sr $^{-1}$. Cette thèse porte également sur le projet d'intégration de modules optiques digitaux, tâche réalisée à la faculté des sciences de Rabat, et constituant une étape majeure dans la construction du télescope KM3NeT.

Mots-clefs: Monopoles magnetique, ANTARES, Cherenkov, telescope a neutrino, KM3NeT, Module Optique Digital.

Abstract

Magnetic monopoles are hypothetical particles that can be detected by their direct Cherenkov emission or that of relativistic secondaries in transparent media. Large scale neutrino observatories designed to detect Cherenkov emission of secondaries produced in high-energy neutrino collisions provide sensitive probes of a cosmic flux of monopoles. This particular signal has been studied by various neutrino observatories like IceCube, ANTARES, Baikal and AMANDA in the past. This work shows a new analysis with ANTARES data collected over ten years (January 2008 to December 2017) that improves previous limits of the collaboration. Compared to previous ANTARES searches, this analysis uses a run-by-run simulation strategy, with a larger exposure as well as a new simulation of magnetic monopoles taking into account the Kasama, Yang and Goldhaber model for their interaction cross-section with matter. No signal compatible with the passage of relativistic magnetic monopoles is observed, and upper limits on the flux of magnetic monopoles with $\beta = v/c \geq 0.55$, are presented. For ultra-relativistic magnetic monopoles, the flux limit is $\sim 7 \times 10 - 18$ cm $^{-2}$ s $^{-1}$ sr $^{-1}$. This thesis focuses also on the project of the integration of digital optical modules, a task carried out in the faculty of science in Rabat, and being a major step in the construction of the KM3NeT telescope.

Key Words: Magnetic monopoles, ANTARES, Cherenkov, Neutrino telescope, KM3NeT, Digital Optical Module.